On osseointegration in response to controlled surface nanotopography

Dimitrios Karazisis

Department of Biomaterials
Institute of Clinical Sciences
Sahlgrenska Academy, University of Gothenburg

UNIVERSITY OF GOTHENBURG

Gothenburg 2021

Cover illustration: SEM picture taken by the author illustrating a cell interacting with a nanopatterned implant surface retrieved after 12 hours of healing.

On osseointegration in response to controlled surface nanotopography

dimitrios.karazisis@biomaterials.gu.se

ISBN 978-91-8009-344-6 (PRINT)
ISBN 978-91-8009-345-3 (PDF)
http://hdl.handle.net/2077/68064

Printed in Borås, Sweden 2021
Printed by Stema Specialtryck AB, Borås

To my family

ABSTRACT

Knowledge about the biological responses provoked by the surface modification of titanium implants on the nanoscale is still in its infancy. Although *in vitro* studies claim superior effects considering higher adhesion and proliferation of osteoblasts in the short term and even differentiation towards the osteogenic cell lineage in the long term, these responses do not necessarily reflect the actual outcome in the complex *in vivo* environment. Therefore, the main aim of this thesis was to evaluate the biological responses at the bone interface to titanium implants with controlled surface nanotopography. Both very early and late healing events were considered, and the phases of acute inflammation, bone regeneration and bone remodeling were evaluated, first in the rat tibia and thereafter in human maxillary bone. This was performed by screening and quantification of genes of interest, representing the different healing phases, by quantitative polymerase chain reaction (qPCR), and correlating these molecular events to morphological (histology and histomorphometry) and biomechanical (removal torque) outcomes of osseointegration.

The first study used a specially designed implant with nanopatterns only at the cylindrical part facing the bone marrow and not the threads that were engaging the cortical bone. Analyses showed that the gene expression of the proinflammatory cytokine tumor necrosis factor alpha (TNF-α) and osteoclast marker cathepsin K (CatK) was downregulated at the nanopatterned implants at 3 and 6 days, respectively. This finding was consistent with fewer CD163-positive macrophages in the peri-implant tissue. Due to improved methodology, the nanopatterns could be applied to complex screw-shaped implants resembling clinical dental implants and used in the second, third and fourth studies. In the second study, evaluating the very early tissue-implant interactions, nanotopography downregulated the expression of monocyte chemoattractant protein-1 (MCP-1) at 12 hours and triggered the expression of osteocalcin (OC) at 3 days. This was in parallel with a relatively lower number of CD68-positive monocytes and a higher proportion of early-formed bone. In the third study, it was demonstrated that the nanotopography could downregulate the expression of the proinflammatory cytokine TNF-α even after 21 days. Osteoclastogenesis molecular activity was down-regulated at implants with combined nano- and microtopography at 6 days. A synergistic effect was disclosed, with the combination of micro- and nanotopography further attenuating the inflammatory response via TNF-α downregulation and resulting in an increased biomechanical stability, as judged by higher removal torque values. A human study showed that implants with nanotopography significantly increased the expression of all the targeted osteoblastic markers, namely, runt-related transcription factor 2 (RUNX2), alkaline phosphatase (ALP) and OC, suggesting the promotion of bone formation.

In conclusion, nanotopography *per se*, attenuates the initial inflammatory response and increases bone formation while down-regulating osteoclastogenesis and bone resorption molecular activities. Furthermore, the combined effect of micro- and nanotopography can further attenuate the inflammatory response and enhance the mechanical stability of the implants.

Keywords: *in vivo*, nanotopography, osseointegration, titanium

ISBN 978-91-8009-344-6 (PRINT)
ISBN 978-91-8009-345-3 (PDF) http://hdl.handle.net/2077/68064

SAMMANFATTNING PÅ SVENSKA

Kunskap om det biologiska svaret på installation av titanimplantat med en yttopografi på nanonivå är i sin linda. *In vitro* studier har visat på ökad adhesion och proliferation av osteoblaster och över tid även differentiering till mogna benproducerande celler, men dessa resultat påvisar inte nödvändigtvis den faktiska nyttan i den mer komplexa *in vivo* omgivningen. Huvudsyftet med denna avhandling var därför att undersöka det biologiska svaret i gränssnittet mellan ben och titanimplantat med en kontrollerad yttopografi på nanonivå. Både det tidiga vävnadssvaret på implantationen i ben och de senare reaktionerna utvärderades. Inflammationsfasen, benregeneration och remodellering studerades molekylärbiologiskt, först i tibia på råtta och sedan i överkäken på människa.

Studierna utfördes genom screening och kvantifiering av specifika gener representerande olika läkningsfaser. För detta användes kvantitativ polymeras kedjereaktion (qPCR) och dessa tester korrelerades med morfologisk utvärdering (histologi och histomorfometri) samt biomekanisk testning (urvridningsmotstånd).

Den första delstudien innefattade ett specialdesignat implantat med nanoyta enbart på den cylindriska delen av fixturen som engagerar benmärgen men inte på den övre gängade delen som har kontakt med det kortikala benskiktet. Analyser av läkningsprocessen visade att genuttryck av den pro-inflammatoriska cytokinen, tumor necrosis factor alfa (TNF-α) och osteoklastmarkören cathepsin K (CatK) nedreglerades vid nanoytan efter 3 respektive 6 dagars läkning. Resultaten stämde även väl överens med ett minskat antal CD163-positiva makrofager i den implantatnära vävnaden. Genom förbättrad metodologi, kunde nanoytan även appliceras på den gängade delen av ett implantat, liknande orala implantat, och användes i delarbetena 2, 3 och 4. I delstudie 2, som fokuserade på den tidiga läkningen mellan ben och implantat, visades att nanotopografi nedreglerade uttrycket av monocyte chemoattractant protein-1 (MCP-1) efter 12 timmar och triggade uttrycket av osteocalcin (OC) efter 3 dagar. Parallellt sågs ett relativt lågt antal CD68-positiva monocyter och en högre grad av bennybildning vid implantaten med nanoyta.

I tredje delarbetet visades att nanotopografi nedreglerade uttrycket av proinflammatoriska cytokinen TNF-α också efter 21 dagars uppföljning. Osteoklasternas proliferation och utmognad dämpades vid implantat som hade en kombinerad nano- och mikrotopografi. En synergi sågs sålunda då en kombination av mikro- och nanotopografi applicerades på implantaten, vilket förbättrade de biomekaniska egenskaperna och visades genom högre urvridningsmotstånd. Fjärde studien som var en humanstudie kunde visa att implantat med nanotopografi signifikant ökade uttrycket av alla målmarkörer för osteoblastaktivitet; runt-related transcriptor factor 2 (RUNX2), alkaline phosphatase (ALP) och osteocalcin (OC), vilka alla signalerar bennybildning.

Sammanfattningsvis ger nanotopografi i sig en attenuering av det initiala inflammationssvaret, ökar bennybildning samtidigt som osteoklastaktiviteten och därmed benresorption inhiberas. Den kombinerade effekten av nano- och mikrotopografi på en titanyta minskar det inflammatoriska svaret och ökar implantatstabiliteten.

LIST OF PAPERS

This thesis is based on the following studies, referred to in the text by their Roman numerals.

I. Karazisis D, Ballo AM, Petronis S, Agheli H, Emanuelsson L, Thomsen P, Omar O. ***The role of well-defined nanotopography of titanium implants on osseointegration: cellular and molecular events in vivo.*** *Int J Nanomedicine. 2016;11:1367-82.*

II. Karazisis D, Petronis S, Agheli H, Emanuelsson L, Norlindh B, Johansson A, Rasmusson L, Thomsen P, Omar O***. The influence of controlled surface nanotopography on the early biological events of osseointegration.*** *Acta Biomater. 2017;53:559-571.*

III. Karazisis D, Rasmusson L, Petronis S, Palmquist A, Furqan A. Shah FA, Agheli H, Emanuelsson L, Johansson A, Omar O, Thomsen P. ***The effects of controlled nanotopography, machined topography and their combination on the molecular activities, bone formation and biomechanical stability during osseointegration.*** *Manuscript Submitted.*

IV. Karazisis D, Omar O, Petronis S, Thomsen P, Rasmusson L. ***The molecular response to nanopatterned implants in human jaw bone.*** *Manuscript Submitted.*

CONTENT

ABBREVIATIONS

AFM	atomic force microscopy
ALP	alkaline phosphatase
ARB	angiotensin receptor blocker
ARG	arginase
BA	bone area
BIC	bone to implant contact
BMP	bone morphogenetic protein
BSP	bone sialoprotein
BV	bone volume
CatK	cathepsin K
CM	conditioned medium
Col	collagen
COX-2	cyclooxygenase-2
CpTi	commercially pure titanium
CTR	calcitonin receptor
DAMPs	damage-associated molecular patterns
ECM	extracellular matrix
EDX	energy dispersive X-ray spectroscopy
ELISA	enzyme-linked immunosorbent array
EPMA	electron probe microanalysis
FAs	focal adhesions

FE-SEM	field emission scanning electron microscope
FGF	fibroblast growth factor
HA	hydroxyapatite
H&E	hematoxylin and eosin
HF	hydrofluoric acid
HIF	hypoxia inducible factor
HMGB1	high-mobility group box 1
ICAM-1	intercellular cell adhesion molecule-1
IGF	insulin-like growth factor
IHM	immunohistochemistry
IL	interleukin
iNOS	inducible nitric oxide synthase
LCM	laser confocal microscopy
MAPK	mitogen-activated protein kinase
MCP-1	monocyte chemoattractant protein-1
M-CSF	macrophage-colony stimulating factor
MIP-1α	macrophage inflammatory protein-1 alpha
MSCs	mesenchymal stem cells
NF-kB	nuclear factor kappa light chain enhancer of activated B cells
OB	osteoblast
OC	osteocalcin
OPG	osteoprotegerin

OPN	osteopontin
OSM	oncostatin M
Osx	osterix
PDGF	platelet derived growth factor
PGE2	prostaglandin E2
PMMA	polymethylmethacrylate
PMNs	polymorphonuclear neutrophils
PS	polystyrene
PTH	parathyroid hormone
PTHrP	parathyroid hormone-related peptide
qPCR	quantitative polymerase chain reaction
RANK	receptor activator of nuclear factor kappa B
RANKL	receptor activator of nuclear factor kappa B ligand
RT	reverse transcription
RTQ	removal torque
Runx2	runt-related transcription factor 2
SDF-1	stromal cell-derived factor-1
SEM	scanning electron microscope
TEM	transmission electron microscopy
TGF	transforming growth factor
TF	tissue factor
TLRs	toll-like receptors
TNF	tumor necrosis factor

TOF-SIMS	time of flight secondary ion mass spectrometry
TPS	titanium plasma spraying
TRAP	tartrate resistant acid phosphatase
UV	ultraviolet
VCAM-1	vascular cell adhesion molecule-1
VEGF	vascular endothelial growth factor
VSI	vertical scanning interferometry
XPS	X-ray photoelectron spectroscopy
μCT	microcomputed tomography

1 INTRODUCTION

1.1 OSSEOINTEGRATION

The success of dental implant treatment is largely attributed to the process of osseointegration, which is a term that was coined by PI Brånemark in 1976 and defined as direct contact between implants and bone at the light microscope resolution level [1]. This definition implies that a direct anchorage is established by the formation of bone around the implant without the presence of fibrous tissue at the bone-implant interface. The condition is evaluated clinically by the stability of the supra-construction and by radiography to ensure bone accrual and marginal bone preservation. Although dental implants have been in clinical use since 1965 and revolutionized clinical dentistry, the osseointegration process in terms of cellular and molecular events is still not completely understood.

Traditionally, healing around dental implants implies the processes of inflammation, bone regeneration and bone remodeling, with possible overlap on certain occasions [2] (*Figure 1*). Knowledge of the healing process of titanium implants has been correlated with histological and molecular studies of normal bone fracture [3]. The presence of the biomaterial, however, will modulate the healing response with new bone formation through intramembranous ossification, i.e., without an intermediate cartilaginous scaffold [4]. The new bone is either formed through apposition as a continuum to the existing bone at some distance to the implant surface preceding resorption, which is referred to as distant osteogenesis [5], or by de novo synthesis via direct contact with the implant, which is referred to as contact osteogenesis [5].

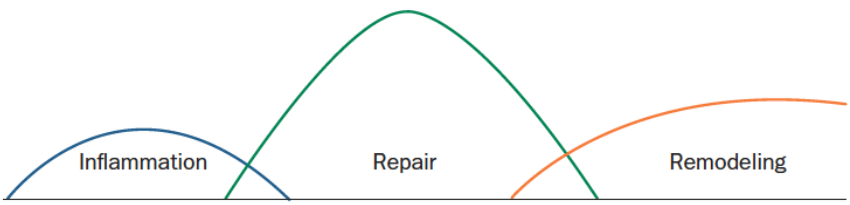

Figure 1. Phases of bone healing after injury and titanium (Ti) implant installation. The transient phase of acute inflammation is followed by bone repair, with some temporal overlap. Thereafter, remodeling ensues, which is lifelong. Reprinted and modified with permission from ref [3].

This process implies that the bone around titanium implants will ossify rapidly without a cartilaginous transition state [6]. Intramembranous ossification involves mesenchymal stem cells (MSCs) directly differentiating into osteoblasts, which in turn deposit mineralized extracellular matrix. The main difference compared to fracture healing is the introduction of a foreign albeit biocompatible material in the osteotomy site. Under optimal conditions, the bone fracture healing process will progress through different maturation phases and result in total morphological and functional restitution of the bone tissue, either via endochondral or intramembranous ossification. This process ultimately implies that the outer cortical bone will seal off the inner trabecular bone with its marrow content, and in the case of installing a titanium implant, the latter will function as an osteoconductive material [7] and modulate subsequent bone healing through its surface characteristics.
Implant surface characteristics have long been recognized as a decisive factor for osseointegration [8]. In the last three decades, the surface properties of titanium implants have been targeted to different modifications to accelerate bone healing, consequently allowing early functional loading. In this thesis, structural elements in the smallest visible dimension, namely, at the nanoscale, have been added to increase the roughness of the titanium implant surface and the biological outcomes of this intervention on osseointegration have been studied *in vivo.*

1.2 BONE HEALING AND OSSEOINTEGRATION: CELLULAR AND MOLECULAR ASPECTS

Bone remodeling and healing under physiological and pathological conditions are highly orchestrated complex biological processes. Morphological and molecular studies on bone fracture healing have provided the basis for understanding bone biology, which has further been correlated with the healing of titanium implants [9]. In the following sections, the complex *in vivo* process of osseointegration around titanium implants is described based on the present level of available knowledge and the sequences of healing are further synthesized with data acquired from wound and bone fracture healing studies.

1.2.1 ACUTE INFLAMMATION

The preparation of the implant bed by drilling results in tissue injury, including vascular damage with extravasation of blood. The coagulation cascade starts immediately after contact of blood plasma with tissue factor (TF) expressed on the membrane of resident macrophages and smooth muscles from the damaged

vasculature, which ultimately leads to blood clot formation, i.e., an organized network of fibrin interacting with activated platelets that bind to fibrin via integrins. Platelets become activated via contact with collagen I in bone tissue, which binds to von Willebrand factor. Platelet activation induces their degranulation, containing among other substances platelet-derived growth factor (PDGF), which is important in angiogenesis, likewise vascular endothelial growth factor (VEGF), which is secreted by endothelial cells [10], macrophages [11] and osteoblasts [12] due to local hypoxia and hypoxia inducible factor-1 (HIF-1) [13]. PDGF has also been shown to stimulate the migration of osteoblasts and mesenchymal progenitor cells [14], while VEGF has been shown to promote the upregulation of bone morphogenic protein (BMP)-2 in endothelial cells, inducing osteogenesis [15]. Histological analysis of angiogenesis and new bone formation around titanium implants in animal studies shows that these processes are positively correlated [16]. The formed blood clot acts as a temporary scaffold for the active invasion of additional inflammatory cells, such as polymorphonuclear neutrophils (PMNs) and macrophages [17].

Furthermore, endogenous molecules are released upon tissue damage, thus leading to activation of the immune system. They are collectively referred to as damage-associated molecular patterns (DAMPs) and consist of proteins, such as heat shock protein, high-mobility group box 1 (HMGB1), inflammatory cytokines, such as interleukin-1 alpha (IL-1α), and small fragments of extracellular matrix (ECM) released during the trauma impact [18]. Pattern recognition receptors, such as Toll-like receptors (TLRs), are involved in the activation of immune cells present on antigen-presenting cells (such as macrophages and dendritic cells). These receptors ultimately induce the activation of transcription factors, such as nuclear factor kappa-light-chain-enhancer of activated B cells (NF-kB), thereby leading to the expression of inflammatory cytokines [18, 19].

The phase of acute inflammation is initiated. The first cells to encounter the damaged tissue are PMN cells, which belong to the innate immune system and present a higher proportion of neutrophils and a lower number of basophils and eosinophils. They are believed to participate in tissue repair by scavenging debris and dead cells [20], although their exact role in bone healing has not yet been elucidated. These cells leave the vasculature under the influence of the proinflammatory cytokines tumor necrosis factor-alpha (TNF-α) and IL-1β and, most importantly, due to the chemotactic cytokine IL-8 also produced by resident macrophages. The expression of all these cytokines has been shown to be modulated by the implant surface, with a downregulation towards moderately roughened implants [21-23]. The extravasation of PMN cells is

highly controlled and completed through initial tethering and rolling by endothelial selectins, activation, arrest, diapedesis and migration. In particular, PMN cell activation is facilitated through a unique receptor, IL-8R [24], which binds to the chemokine IL-8. This specific receptor-ligand interaction affects the affinity of integrins that are essential for cell arrest in the next step by inducing conformational changes in their extracellular domains. Integrins are a family of heterodimeric transmembrane cell adhesion molecules, and their expression is upregulated rapidly by chemokines [25]. Leukocyte-restricted β2 integrins ($\alpha L\beta_2$, $\alpha M\beta_2$, $\alpha X\beta_2$ and $\alpha D\beta_2$) [26] bind to endothelial intercellular cell adhesion molecule (ICAM-1), thereby facilitating cell arrest. Thereafter, it is possible for the recruited PMN cells to transmigrate through the endothelium and basal membrane and migrate through the interstitial tissue to the site of injury under the guidance of a chemotactic gradient. Although PMN cells are recruited within the initial hours, their presence is transient and wanes rapidly thereafter within 24 hours, thus leaving place for the action of monocytes/macrophages, which increase in number after 24 hours, with a peak accumulation at 4-7 days [27-29]. Neutrophils secrete various cytokines and growth factors that trigger the migration of more neutrophils and promote the migration of other immune cells, such as macrophages, to the injury site [30].

1.2.2 CELL RECRUITMENT AND ADHESION DURING INFLAMMATION

Monocytes/macrophages constitute a critical cell type, and their actions lead to either implant osseointegration or failure [31]. The recruitment of peripheral monocytes follows the same procedure as PMN cells and is stimulated by the secretion of IL-6, which is produced by macrophages and stimulates the secretion of monocyte chemoattractant protein-1 (MCP-1) [32, 33]. This chemokine is implicated in the early healing of implants in the homing of monocytes by binding to its receptor CCR2 and further positively correlated with the expression of the proinflammatory cytokines TNF-α and IL-1β [24].

Another important chemokine that provides local and systematic migration axes for mesenchymal stem cells (MSCs) to sites of tissue repair and regeneration is stromal cell-derived factor-1 (SDF-1), which is expressed by both hematopoietic cells , such as macrophages, and nonhematopoietic cells, such as endothelial cells, fibroblasts and mesenchymal stem cells [34, 35]. The release of SDF-1 is induced by low local oxygen tension in the tissue due to trauma and the expression of the transcription factor HIF-1α [36, 37]. MSCs are potent progenitor cells capable of differentiating into various mesenchymal tissues. The homing process of MSCs in osseointegration is promoted early at the interface zone [24, 38] and resembles that of PMN cells. Cell activation is

promoted by the binding of chemotactic SDF-1 to its receptor CXCR4, which is expressed by MSCs [24]. Subsequent cell arrest occurs through the binding of integrins to endothelial vascular cell adhesion molecule-1 (VCAM-1). Integrin α4β1 has been suggested to be important for MSC recruitment [39]. An animal fracture study showed that MSC migration exclusively relied on CXCR4 and was time- and dose-dependent [40], which is consistent with that observed for titanium implants [24, 41]. However, other receptors are possibly also involved since MSCs express a magnitude of other receptors, including CCR1, CCR2, CCR4, CCR7, CCR9, CCR10, CXCR5, CXCR6 and CXCR7, the functions of which are not entirely described. [42]. It has been shown that CXCR7 can similarly bind to SDF-1 and facilitate the homing of MSCs to various tissues [43].

1.2.3 MESENCHYMAL STEM CELL (MSC) DIFFERENTIATION AND BONE REGENERATION

MSCs in the bone marrow, endosteum and perivascular cells, both at local and distant sites, are the most important sources for skeletal repair. Stem cell populations are established in niches, i.e., specific anatomic locations that regulate their actions and population maintenance by self-renewal [44]. MSCs have trilineage potential within their own mesenchymal origin, meaning that they can differentiate into chondroblasts, osteoblasts and adipocytes [45]. Differentiation of MSCs through the osteogenic lineage is stimulated mainly by growth factors belonging to the transforming growth factor β (TGF-β) superfamily and mainly by bone morphogenetic proteins (BMPs) [19, 46, 47], with BMP-2, -4, -5, -6, -7 and -9 exhibiting high osteogenic activity [48, 49]. BMPs transduce intracellular signals via the canonical Smad-dependent signaling pathway and the noncanonical Smad-independent pathway through p38 mitogen-activated protein kinase (p38 MAPK) (*Figure 2*). Both of these signaling pathways converge at runt-related transcription factor 2 (Runx2), which promotes osteoblast differentiation from mesenchymal precursor cells [50] (*Figure 2*) and ultimately enhances bone formation and implant anchorage [21, 51]. The coexistence and crosstalk with other signaling pathways induced by critical cytokines, such as Wnt, Hedgehog, Notch, parathyroid hormone-related peptide (PTHrP) and fibroblast growth factor (FGF), emphasize the complexity of the osteogenic differentiation process.

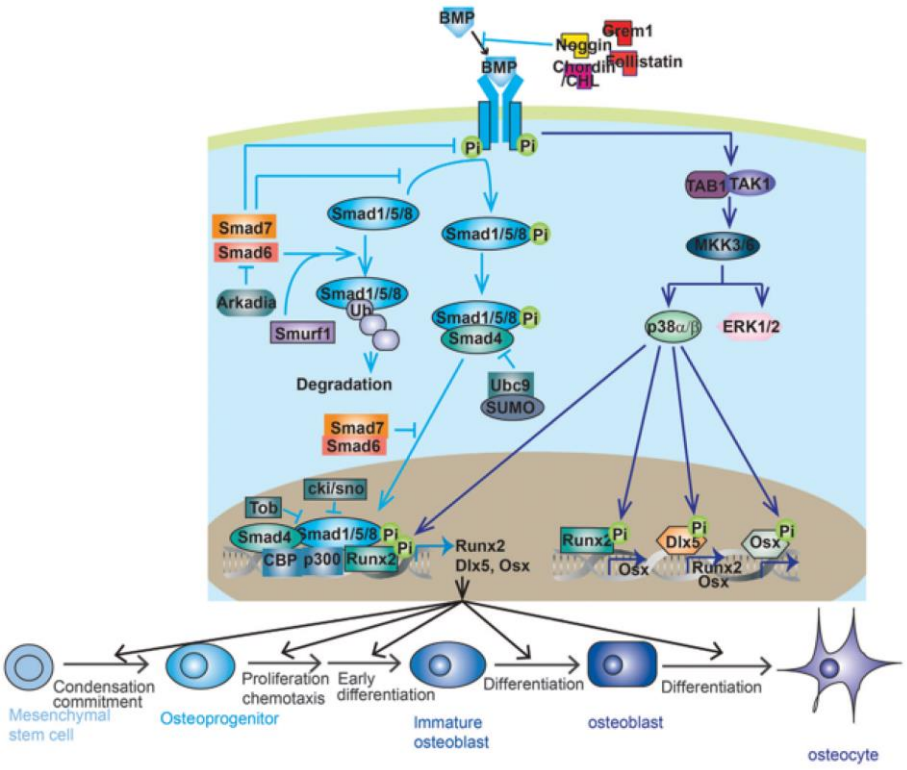

Figure 2. BMP signaling pathways in bone. Both the Smad-dependent and Smad-independent pathways converge into the transcription factors Runx2, Osx and Dlx5, which promote every step during osteoblast differentiation and maturation. Reprinted and modified with permission from ref [50].

Runx2 is the transcription factor expressed and required for commitment of progenitor cells to the osteogenic lineage and excludes divergence options towards the chondrogenic or adipogenic lineages [52]. Its crucial role has been demonstrated in Runx2 knockout mice, which show a cartilaginous skeleton with a complete lack of ossification [53]. Although indispensable in the early commitment to the osteogenic lineage, Runx2 is also important in later stages by promoting the transcription and production of characteristic osteogenic phenotype proteins, such as collagen type I, alkaline phosphatase (ALP), osteocalcin (OC) and bone sialoprotein (BSP). An upregulation of these osteogenic markers has been shown *in vivo* towards microroughened and/or chemically modified titanium implant surfaces [21, 22, 51, 54, 55]. ALP is regarded as a late osteoblast marker that is essential in the process of matrix mineralization [56]. OC and BSP are early expressed noncollagenous proteins embedded in the bone ECM, with BSP serving as a nucleating site for

hydroxyapatite (HA) crystal formation [57]. Bone regeneration occurs through MSC proliferation and condensation around a profuse capillary network to form a center of calcification, where the progenitors differentiate into osteoblasts and bind to noncollagenous matrix proteins via integrins in an RGD-dependent manner (arginine-glycine-aspartic amino acid motif), preferably via α5β1, which is the most abundantly expressed integrin throughout osteoblastic differentiation [58]. In addition to matrix adhesion, it is believed that integrin binding might contribute to osteoblast differentiation. After binding, osteoid is laid and replaced by lamellar bone through remodeling [59, 60]. It has been demonstrated in animal studies that the differentiation of osteoblasts begins sooner at the bone implant interface than osteotomy sites alone [61]. Osteoblasts embedded in their own bone matrix become osteocytes that function as mechanosensory cells and lead to direct adaptive changes of the skeleton under mechanical loading [62]. At the molecular level, osteocytes lose their ability to express several of the characteristic osteoblast markers, such as collagen I, ALP, OC, BSP and Runx2 [63]. They are involved in normal bone homeostasis and remodeling and communicate with the bone surface, the quiescent osteoblasts termed lining cells, from their lacunae with cytoplasmic processes passing through small channels called canaliculi [64]. Similarly, osteocytes play an important role in the long-term maintenance of osseointegration [65].

1.2.4 MSCs AND MACROPHAGES: RECIPROCAL CROSSTALK

After diapedesis of MSCs through the vascular wall, their chemotaxis depends on signals released upon tissue injury. Cytokines and chemokines secreted by activated macrophages, such as TNF-α, IL-6, SDF-1 and IL-8, and growth factors, such as PDGF-AB and insulin-like growth factor (IGF)-1, are important [39, 66]. In an *in vitro* setting, MSCs preincubated with TNF-α upregulate their receptors CCR2, CCR3 and CCR4 and promote their migration [67, 68]. Furthermore, the inflammatory chemokine IL-8 also stimulates MSCs to secrete regenerating factors, such as VEGF [69, 70].

Macrophages seem to interact closely with MSCs and determine their ultimate osteogenic differentiation. Nonactivated macrophages have been shown *in vitro* to promote MSC proliferation and enhance their osteogenic activity by increasing the expression of ALP, OC and osteopontin (OPN) through BMP-2 production [71, 72]. Another *in vitro* setting demonstrated that these effects were mediated by the cytokine oncostatin M (OSM) secreted by monocytes in a dose-dependent manner after direct cell-to-cell contact with MSCs [73].

Classically activated macrophages (M1) also induced the expression of BMP-2, Runx2 and ALP in human bone MSCs *in vitro* [74]. Similarly, another *in vitro* study showed that lipopolysaccharide (LPS) stimulation of macrophages induced the production of OSM via induction of cyclooxygenase-2 (COX-2) and prostaglandin E2 (PGE2), and OSM signaling on MSCs led to enhanced osteogenesis [75]. Compared with these findings, OSM has been shown to be produced by alternatively activated macrophages (M2) instead [76]. The findings from another *in vitro* study were extrapolated and indicated that M1 macrophages promote MSC-mediated osteogenesis in the early and middle stages without matrix mineralization via secretion of OSM while M2 macrophages promote increased matrix mineralization via BMP-2 production [77]. These findings show that the exact mechanisms by which macrophages promote bone formation through MSCs remain to be determined. This lack of knowledge is also apparent in the osseointegration of titanium implants.

Reciprocal crosstalk also occurs. MSCs regulate macrophage chemotaxis by secreting the chemokine CCL2 (MCP-1), among others [78]. Furthermore, they exert broad immunomodulatory effects on both the innate and adaptive responses of the immune system. Regarding innate immunity, MSCs suppress proinflammatory cytokines (TNF-α, IL-1β, and IL-6) and prevent M1 macrophage polarization while promoting M2 polarization [78].

1.2.5 MACROPHAGES AND BONE HOMEOSTASIS AND REGENERATION

Macrophages play a central role in the inflammatory response and the recruitment of progenitor cells. Evidence supporting an equally important role in bone homeostasis and regeneration is emerging, and they appear to participate in regulating physiological bone responses and homeostasis [79]. This role has been primarily highlighted in macrophage depletion study models, which have shown that the resident macrophages that normally reside with bone lining cells, occasionally termed osteomacs, within both the periosteum and endosteum participate in the remodeling process in close approximation to activated cuboidal osteoblasts [80]. When macrophages were depleted, the remodeling process was compromised [81]. In bone fracture studies of the mouse tibia, the depletion of macrophages from sites of intramembranous healing resulted in impaired woven bone deposition [82], whereas during endochondral healing, cartilaginous callus formation was impaired instead [83]. In both healing types, depletion of macrophages was more detrimental if it occurred immediately before or at the time of injury, showing that the greatest contribution of macrophages to bone and cartilage formation occurs during the early inflammatory phase. However, the exact

mechanisms by which macrophages contribute to bone regeneration remain unclear.

The general paradigm relies on the initial action of inflammatory macrophages that amplify the inflammatory process and clearance of damaged tissue by classically activated or M1 macrophages. They secrete a wide variety of proinflammatory cytokines, including TNF-α, IL-1β, IL-6, IL-12, matrix metalloproteinase (MMP) 2 and MMP9 [84]. Thereafter, a transition to regenerative macrophages occurs during late healing. These M2 macrophages also secrete a wide variety of regenerative cytokines, including PDGF-BB, transforming growth factor-1 (TGF-1), VEGF, IL-4, IL-10 and CCL18 [84]. Interestingly, moderate titanium implant surface roughness seems to modulate the expression of cytokines and thereby macrophage phenotype by decreasing the expression of proinflammatory cytokines [22-24] and increasing the expression of anti-inflammatory cytokines [85].

By secreting these cytokines, macrophages regulate both inflammation and MSC migration and commitment to the osteogenic cell lineage, as highlighted previously, as well as osteoblast function. The M1 phenotype, with its constitutively produced paracrine factors, seems to negatively influence bone formation, whereas M2 macrophages seem to promote bone regeneration [18] (*Figure 3*). However, their exact role in bone healing has not been fully elucidated.

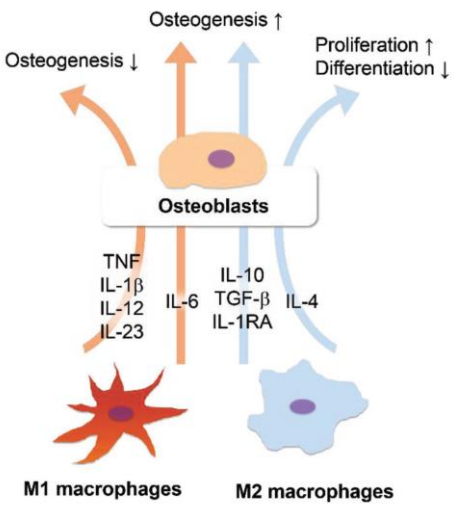

Figure 3. Schematic illustration of the impact of the various macrophage phenotypes on osteogenesis. Reprinted with permission from ref [18].

The number of macrophages decreases after transient acute inflammation around the implants [85], thus reaching low levels during the bone regeneration process, while in the remodeling phase, they are almost absent, thus leaving room for the coordination of this process through another cell of the myeloid lineage, namely, the osteoclast.

1.2.6 BONE REMODELING

Bone remodeling is a physiological process for maintaining normal bone mass and calcium homeostasis and repairing microdamage, and it is active throughout life. Bone is resorbed in prospected sites by osteoclasts and reformed by osteoblasts, with resorption of bone in implant contact regions and bone formation in noncontact regions [86]. Osteoclasts are multinucleated cells at terminal differentiation, and they are generated by the fusion of precursors from the monocyte lineage. This process is promoted by macrophage-colony stimulating factor (M-CSF) and TNF-related receptor activator of nuclear factor kappa B ligand (RANKL), which are both produced by osteoblasts. RANKL is a membrane-associated factor on osteoblasts, and a physical interaction with osteoclast progenitors expressing the receptor activator of nuclear factor kappa B (RANK) receptor is mandatory for their terminal differentiation. Osteoprotegerin (OPG), a soluble decoy receptor mainly produced by osteoblasts, acts competitively and binds RANKL, inhibiting osteoclast differentiation [87]. It has been shown that anti-inflammatory IL-4 secretion can stimulate osteoblasts to generate OPG [88].

During inflammation due to bone tissue injury, osteoclastogenesis through the RANK-RANKL-OPG triad can also be augmented by the inflammatory cytokines TNF-α and IL-1 [89-91]. Furthermore, TNF-α and IL-1 modulate this system primarily by stimulating M-CSF production and by directly increasing RANKL expression [92]. Microroughened titanium implants show a higher RANKL/OPG ratio at early healing, thus denoting early bone remodeling and ultimately bone maturation compared to machined implants [91].

Mature osteoclasts bind to exposed RGD sequences of noncollagenous bone proteins and native collagen type I at the site of prospected resorption via integrins, primarily αvβ3 (vitronectin receptor) and α2β1 (collagen type I receptor), respectively [58]. This binding forms a tightly sealed zone under which bone resorption can occur. A highly acidic microenvironment is created, leading to mineral dissolution followed by enzymatic degradation of the organic constituents via lysosomal proteases, such as cathepsin K (CatK), and tartrate-resistant acid phosphatase (TRAP) degrading phosphoproteins,

including OPN [93]. The expression of calcitonin receptor (CTR) also correlates well with bone resorption [94], and this process is followed by bone formation by osteoblasts at the resorption pits, which are also called Howship's lacunae. Osteoblasts are recruited and differentiated through signals released from the ECM during the osteolytic process, such as insulin growth factor 1 (IGF-1), TGF-β and BMP-2. New ECM deposition and mineralization restitute the bone tissue.

Systemically, bone remodeling is controlled by the action of three calcium-regulating hormones: parathyroid hormone (PTH) and 1,25$(OH)_2$-D3, which stimulate resorption, and calcitonin (CT), which inhibits osteoclastic resorption. Calcitonin binds to CTR on osteoclasts and disrupts the ruffled border and further inhibits the secretion of proteolytic enzymes terminating bone resorption [95].

Bone healing and osseointegration involve pro- and anti-inflammatory responses, progenitor cell recruitment, osteoinduction, growth factor/transcription factor expression, signaling pathway regulation, and extracellular matrix production, all of which are intricate physiological mechanisms that are highly and properly controlled and regulated [19]. The above presentation is rather simplified in an effort to spatially and temporally delineate the different molecules of interest investigated by quantitative PCR (qPCR). For a more comprehensive description of the process, the reader may refer to reviews in the field [96-99].

1.3 DESCRIPTIVE HISTOLOGY, HISTOMORPHOMETRICAL CONSIDERATIONS AND BIOMECHANICS OF THE BONE IMPLANT INTERFACE

The temporal sequences of osseointegration of titanium implants with moderate microscale surface roughness in humans are presented here based on descriptive histological details [4, 5]. Bone formation is evident within the first week of implant healing. This bone is woven in structure and recognized by numerous large osteocyte lacunae, emerging from the surface of the cut bone and by distant osteogenesis, thus forming a scaffold of tiny trabeculae growing towards the implant surface. Occasionally, minor areas of woven bone appear de novo in direct contact with the implant, which is referred to as contact osteogenesis. After two weeks, the regions of woven bone increase in volume with bridging to the implant surface. At the same time, osteoclastic activity is

evident in areas under pressure, which confers initial stability. These areas are located mainly at the pitches of the implant threads, which are replaced by new bone. In parallel, the process of replacing the woven bone by organized and mechanically superior lamellar bone is almost completed after 4 weeks. Bone remodeling continues thereafter throughout life, and it involves even the bone-implant interface and might transiently expose earlier bone-covered implant surfaces.
Compared with humans, rat models show higher bone turnover. Early signs of bone formation appear in the first 3 days after implantation, with complete bone formation around the implants achieved at 28 days [100, 101].
The method of choice for evaluating the amount of bone in contact with the implant surface is histomorphometry. The bone-to-implant contact (BIC) is measured as the percentage of the implant surface covered by bone. Furthermore, a higher BIC, which is influenced by implant physicochemical properties, has been shown to positively affect implant biomechanical interlocking as measured by push-out, pull-out or removal torque analyses [4]. The greater the forces needed to loosen the implant, the greater the osseointegration strength.

1.4 IMPLANT-RELATED FACTORS AFFECTING OSSEOINTEGRATION

Decisive factors associated with the titanium implant and their role in osseointegration are briefly presented.

The implant bulk material and its chemical composition are important for providing the mechanical properties required for its application. Additionally, the implant design, referring to its macroscopic shaping and geometry, is critical for the primary fixation of the implant. Implant surface characteristics are of the greatest importance for the rate and quality of healing [102] and influence the adhesion of proteins that in turn influence cell adhesion and assembly onto the surface, thus determining cell dynamics at an early crucial stage of tissue healing [103] (*Figure 4*).

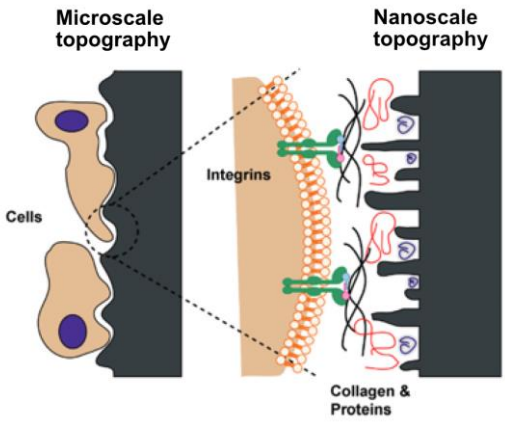

Figure 4. Schematic illustration of the interactions between bone and implant surface at different length scales. Reprinted and modified with permission from ref [104].

The implant surface characteristics can be divided into (1) mechanical, (2) topographic and (3) physicochemical properties. The mechanical properties of the implant surface refer to fatigue strength, hardness, friction and resistance to wear and fracture. Most of these properties directly correlate with the core material properties. Titanium implants are currently composed of commercially pure titanium (cpTi) grades 1 through 4. The material hardness increases with the grade through the incorporation of small amounts of Fe and O. An increased hardness of grade 4 is preferably utilized in small diameter implants to avoid mechanical fractures [105].

The topography can be divided at different length scales. Hence, the definition of micro- and nanoscale topography applies to features with at least one dimension smaller than 100 μm and 100 nm, respectively (the term submicron-scale is also frequently encountered in the literature encompassing features smaller than 1 μm but larger than 100 nm). The role of topography in osseointegration is comprehensively evaluated in the following sections.

The physicochemical properties are characterized by the surface chemical composition, crystallinity, wettability (surface energy) and surface charge (zeta potential). Commercially pure titanium (cpTi) spontaneously forms an oxide layer on its surface when exposed to atmosphere. This mainly amorphous native TiO_2 can form three different crystalline structures. Rutile is the most common, although anatase and brookite are also observed. The most common crystallization method is annealing [106]. The effects of the various crystalline structures on osseointegration are unclear. Contradictory *in vitro*

results have been reported, although they showed a superior effect of anatase, which promotes enhanced fibronectin adsorption and conformational changes that subsequently lead to increased osteoblast adhesion [107]. On the other hand, crystallinity and thickness do not have an effect on osteoblast or fibroblast viability [108]. Concerning wettability, *in vitro* studies have shown that hydrophilicity is a superior surface property for cell attachment, spreading, integrin expression, differentiation, ECM protein secretion and mineralization [109]. In the *in vivo* setting, pronounced new bone formation and bone-to-implant contact after 2 and 4 weeks occur for hydrophilic implants [47, 110]; however, these effects are no longer evident after 6-8 weeks [111], thus showing that the role of hydrophilicity being uncertain and unexplored in the long term [105].

The surface chemical composition has been explored and exploited to the same degree as the surface topography. HA coatings have been addressed with the theoretical advantage of sharing the same chemistry as bone that promotes chemical bonding. Clinical evaluations, however, have shown unacceptable marginal bone loss due to loosening of the coating [112]. Chemical modifications by incorporating Ca, P, Sr, F, NaOH and Mg have been shown to provide a strong bone response [105]. In particular, alkali treatment has been shown to alter the topography of the implant by inducing the formation of a fine porous network structure with pore size in the nanometer range, which positively affects mineral deposition *in vitro* and bone formation *in vivo* [113]. The roughness produced by alkali treatment is time dependent, with increasing values correlated with increasing immersion time [114]. Finally, surface charge is essential for protein adsorption in the *in vivo* environment and further cellular adhesion. Titanium surfaces are negatively charged at physiological pH, and many extracellular proteins, such as fibronectin, which are important in osteoblast adhesion. Changing the surface charge of the titanium surface towards electropositivity would promote the adhesion of proteins [115] and cell membranes of osteoblasts [116] via electrostatic forces. However, it is very difficult to control the surface charge of implant interfaces.

Other nonimplant-related factors affecting osseointegration include the general medical health of the patient as well as the local conditions of the recipient tissue site as determined by the bone quantity and quality [117]. Finally, the surgeons' acquired skills and the carefully planned loading conditions of the suprastructure by prosthodontists must account for the short- and long-term success of the implant [117].

1.4.1 SURFACE TOPOGRAPHY AND EFFECTS ON OSSEOINTEGRATION

1.4.1.1 MICROTOPOGRAPHY

As mentioned previously, load-bearing implants have intentionally been developed to include specific surface designs at the macroscopic level because implant shape affects the initial mechanical support and hence the strength of the implant integration [4]. Additionally, microscale surface features further contribute to better biomechanical anchorage.

In vitro studies have shown that microroughened titanium surfaces increase osteogenic activity and promote osteoblastic differentiation, as revealed by increased ALP activity, type I collagen production and Runx2 gene expression [118]. Furthermore, these surfaces seem to modulate the initial inflammatory response by causing a decrease in proinflammatory cytokines and an increase in anti-inflammatory cytokines compared to smooth surface substrates [119].

Likewise, *in vivo* studies support the beneficial results of microroughness in terms of increased BIC and biomechanical anchorage compared to machined implants [21, 120]. Furthermore, early *in vivo* downregulation of the inflammatory response through decreased cytokine TNF-α and IL-1β expression levels as well as early increased osteogenic activity markers, as revealed by higher expression levels of ALP and OC, relative to that of machined implants has been proven [22, 24]. These differences are thought to be feasible through earlier homing of MSCs, as proven by the early upregulation of CXCR4 [24]. The degree of microroughness can modulate bone formation with stronger responses towards moderately rough surfaces (Sa between 1.0 and 2.0 μm) relative to smoother or rougher surfaces [121]. Histological studies in animals have shown that microroughness also promotes contact osteogenesis compared with machined or polished surfaces, where bone healing occurs solely by distant osteogenesis.

The main production methods used for fabrication of microroughened surfaces on commercially available dental implants today are mainly based on subtractive techniques. The surface is subjected to removal or reorganization of the superficial surface layer. These techniques include blasting, blasting and etching or oxidization. Additive methods, such as titanium plasma spraying (TPS) and HA coatings, have been previously used, resulting in either to rough surfaces with increased failure rates [122] or coating detachment with impaired osseointegration as a result [112, 123].

1.4.1.2 NANOTOPOGRAPHY

Adding nanoscale patterns on the surface of bone implants is part of the biomimicking concept in an effort to emulate its hierarchical structure. Indeed, bone is a natural composite mineralized tissue with both organic and inorganic constituents at the nanoscale, collagen fibrils and hydroxyapatite (HA) crystals, respectively. HA self-assembly takes part in the gap zones created between the collagen fibrils, which are 67 nm in width after their cross linking [124]. It has also been observed that under physiological bone remodeling and during osteoclastic activity, microscale resorption lacunae are created with a diameter of 30 to 100 μm. In these pits, collagen tufts and fibers are exposed, creating a specific nanotopography [104]. It has been hypothesized that these structural and biochemical remnants could be the signals required by osteoblasts when prospecting areas in need of new bone formation. Therefore, expertise and methods from widely separated fields, such as nanotechnology, material engineering and biology, have come together in an endeavor to mimic this nanoscale microenvironment and recreate it on bone implant surfaces that would predictably promote bone formation and osseointegration.

1.4.1.3 METHODS FOR PRODUCING NANOPATTERNED SURFACES

Nanofabrication technology has grown tremendously in recent years, thus facilitating the generation of controlled nanoengineered topographies. These developmental advances have led to reproducible production following standardized protocols, which enables their biological evaluation by researchers in a controlled and repetitive manner.

The methods for fabricating titanium nanopatterns can be divided into two approaches. The first type implies subtractive techniques that require the removal of material from the bulk, and they are also denoted top-down methods. The second type consists of organizing small entities, such as atoms, molecules or nanoparticles, to build up the desired nanoscale surface architectures, and they are also termed bottom-up methods [125].

1.4.1.3.1 Top-down methods

Photolithography uses ultraviolet (UV) light as the source of radiation. A UV nontransparent material called a photoresist is used as a mask, with the desired pattern positioned on top of a photosensitive surface. After exposure to UV light, the photosensitive material not covered by the mask can be chemically removed by a developer solution. Only micron- and submicron-scale features can be produced due to limitations set by the diffraction of the light. However, this limit can be overcome by the replacement of UV light by electron or X-

ray beams. Thus, *electron beam and X-ray lithography* can produce nanostructures less than 100 nm at a very high resolution, even without using a mask [126, 127]. Irradiation with light beams from a laser source can be utilized directly for modifying solid materials, such as metals, ceramics and polymers. The patterns of ordered lines or dots are created by the method referred to as *laser interference lithography* [128]. Correspondingly, different nanotopographies can be produced by lithography as nanopits, nanodots and nanogrooves [125, 129].

Etching is another method of choice using either plasma or aggressive chemicals. Plasma is utilized to remove material from the substrate surface. By reactive ion etching, both organized and random nanotopographies can be produced depending on whether a mask is used [128]. In chemical etching, the substrate is immersed in strong chemicals termed etchants or exposed to their vapor [130, 131]. By varying the acids or peroxides by using them in combination or in different concentrations and exposure times, the amount of removed material can be adjusted, thus leading to the production of random nanotopographies. After treatment, it is possible to obtain nanopits with variable sizes ranging from 20-100 nm [125].

Anodization (or anodic oxidation) is an electrochemical process that adds to the natural oxide layer onto the surface of titanium or Ti-alloys, thus leading to a partially ordered nanotube formation [132, 133]. The diameter of the pores, thickness of the wall and height of the tubes can be precisely determined by varying the chemistry of the electrolyte, voltage and current density. In addition, by adjusting the applied potential, it is also possible to transform the protective amorphous oxide layer into one of its crystalline forms [134].

Additionally, selected patterns can be replicated in thermoplastic polymers by *nanoimprinting*. A thin layer of thermoplastic material can be coated on a substrate, heated above its glass transition temperature and pressed against a nanotopography intended to imprint. By *replica molding,* an elastomeric polymer is used instead. The reproduction of the intended nanotopography is generated once again by pressing, although the elastomer hardens once it is treated at high temperatures. A range of different nanotopographies, such as nanopits, nanopillars or nanogrooves, can thus be reproduced [125].

1.4.1.3.2 Bottom-up methods

Colloidal self-assembly involves the spontaneous organization of predetermined micron- or nanosized particulates on substrates that can be used either as topographical features or as masks for subsequent lithography. When used as masks, etching by UV, e-beam or ion irradiation can be employed, and

the method is referred to as colloidal lithography. Further deposition of material on top of the colloidal assembly is possible [135-137]. The assembly of nanocolloids on the surface can be improved by chemical pretreatment of the surface to facilitate electrostatic or covalent binding. Particulates can be synthesized with controlled diameters and positioned in predetermined densities after surface pretreatment or the electrostatic particle-particle interaction can be exploited to generate a well-controlled nanotopography [125].

Interconnecting pores in a foam-like structure or nanodots can be created by *phase separation or polymer demixing*. This phenomenon is utilized when mixing a polymer or a polymer blend in a solvent beyond its ability to solubilize it, thus resulting in a polymer-rich end and a polymer-thin end. The polymer-rich end will solidify, while the polymer-thin end will ultimately be removed. The technique is applicable to polymers and solvents, and the production parameters can be precisely regulated, resulting in random interconnected pores of predetermined size and density with surface nanopatterns, such as islands, fibers, pores and grooves [125].

Fibers or threads with average diameters below 100 nm can be produced from solutions of complex and large polymers by *electrospinning.* The method uses a high electrical charge that leads to electrostatic repulsion, ultimately overcoming the surface tension when applied to a droplet of a polymer-based solution, which results in the eruption of the droplet and the generation of a liquid jet that forms nanosized fibers. The arrangement can be controlled to yield random or unidirectional fibers [125].

By employing these methods, the resulting nanotopography can be either random, partially ordered or ordered (*Table 1*).

Table 1. Nanotopography types categorized by degree of order with the coupled fabrication method and pattern shape production.

Nanotopography type	Fabrication method	Pattern/shape
Random	- etching - electrospinning	- pits - fibers
Partially ordered	- phase separation/polymer demixing - low-voltage anodization - colloidal lithography	- islands/pits - tubes - protrusions/pits
Ordered	- electron/X-ray beam lithography - laser interference lithography - nanoimprinting, replica molding	- free shape - grooves, dots, pits - free shape

1.4.1.4 CHARACTERIZATION OF THE SURFACE NANOTOPOGRAPHY

The most common method applied for analyzing nanotopography is scanning electron microscopy (SEM) [138], in which a focused electron beam interacts with the atoms of the substrate to produce various signals. The signals of interest in the production of contrast images of the nanotopography are from the secondary electrons emitted by atoms at the top few nanometers of the sample; these electrons are excited by the electron beam and captured using a secondary electron detector. The acquired images may have a resolution of less than 2 nm, and the image can be recorded in a few seconds; however, the substrate needs to be electrically conductive or coated with a thin metallic film to prevent charging due to exposure to the e-beam.

The quantitative information obtained from SEM is limited to the vertical axis, meaning that this method can be used to characterize the shape and lateral size of nanopattern features (width, diameter, and interparticle distance) but cannot provide accurate information about vertical dimensions, such as the height of nanopillars or depth of nanopits/grooves. This limitation can be circumvented by the atomic force microscopy (AFM) method, which can be used to quantify both lateral and vertical dimensions of nanopatterns [139]. This method combines a mechanical interaction with the substate through a probe that reproduces a surface image at a resolution of atomic sizes. The main disadvantages are long image recording times (minutes to hours), small field of view, limited z-range and possibility of image artifacts due to tip geometry.

1.5 *IN VITRO* STUDIES OF NANOTOPOGRAPHY AND BONE REGENERATION

Various *in vitro* cell models have been used to understand the effects exerted by nanotopography. Herein, we review the major modulatory cellular effects of nanotopography observed *in vitro* to understand the interactions of mesenchymal stem cells, osteoprogenitors and osteoblasts, and the immunomodulatory effects mediated by macrophages (*Table 2*). Depending on the order of the nanofeatures, a distinction has been made among random, partially ordered and ordered patterns. Random patterns are produced with limited or no control over orientation and geometry. Since these patterns are difficult to reproduce, quantifying the cellular effects provoked by the supposed individual nanofeatures is challenging. On the other hand, semiordered patterns have features with controllable dimensions in a short-range array while ordered patterns consist of precisely defined geometric features in large arrays, which makes it easier to study the different cellular responses and relate them to specific characteristics of the pattern [109]. Therefore, even if these studies represent all the degrees of order for narrative reasons, preferential selection of mainly semiordered and ordered nanopatterns produced on titanium substates is performed whenever possible since some nanotopographies are still technically difficult to reproduce on Ti substates, such as ordered nanopits and nanogrooves. Patterns exceeding 100 nm in all three dimensions were excluded since, by size definition, they are not considered nanopatterns.

Table 2. Description of in vitro studies using nanopatterns for bone regeneration applications.

Pattern shape and degree of order	***Pattern material/* microroughness**	***Fabrication method***	***Nanopattern dimensions***		***Surface characterization (topography)/*chemistry**	***Cell type***	***Main cell response***	***Ref***
			***Diameter/* inter-particle distance or density**	***Height/ depth***				
Nanopit random patterns	*cpTi/* polished	Etching - acid oxidation and peroxidation (H_2SO_4/ H_2O_2)	*10 nm/* NR	NR	*FE-SEM/* **NR** - but different fabrication methods employed for test and control substrates	rat calvarial osteo-progenitors	- enhanced osteogenic activity based on higher expression of OPN and BSP assayed by immunofluorescence on nanostructured substrates after 4 days compared to the polished substrates - increased matrix mineralization after 10 and 14 days	[131]
Nanopit random patterns	*cpTi/* flat	E-beam evaporation	*40 nm, > 100 nm/* NR	4 and 30 nm respectively	*SEM, AFM/* **NR**	human monocyte cell line	- decreased adhesion of macrophages after 4, 12 and 24 hours on the nanoroughened substrates with 40/4 nm nanofeatures (Ø/height) assayed by immunofluorescence when compared to the substrates with >100/40 nm submicroroughness (Ø/height) and flat controls - the same trend after 12 and 24 hours could also be seen after LPS stimulation of the macrophages (nano < submicro < flat control) - decreased TNF-α, IL-1β and IL-6 cytokine release as evaluated by ELISA after 4, 12, 24 and 36 hours on both substrates with nano and submicroroughness compared to the flat controls	[140]
						hOBs	- increased osteoblast adhesion after 4 hours assayed by immunofluorescence on both substates with nano and submicroroughness compared to the flat controls (submicro < nano < flat)	[141]
Nanopit random patterns	*cpTi and Ti6Al4V/* machined	Etching - acid oxidation and peroxidation (H_2SO_4/ H_2O_2)	*10 nm/* NR	NR	*FE-SEM/* **NR** - but different fabrication methods employed for test and control substrates	rat calvarial osteo-progenitors	- enhanced osteogenic activity by higher expression of OPN after 6 hours and 3 days, and BSP after 3 days assayed by immunofluorescence on nanostructured CpTi and Ti6Al4V substrates compared to the machined substrates	[130]

Nanotubes partially ordered patterns	*cpTi/* flat	Anodization	*80 nm/* NA	400 nm	*SEM/* **NR** - but different fabrication methods employed for test and control substrates	rat MSCs	- higher adhesion after 1 day and higher proliferation (40% higher) of MSCs cultured on Ti substrates with 80 nm tubes in comparison to flat Ti substrates - enhanced osteogenic activity by higher expression of ALP (50% increase) assayed by immunofluorescence after 3 weeks - greater bone mineral deposition after 3 weeks on the substrates with 80 nm nanotubes determined by XPS and compared to the flat Ti substrates	[142]
Nanotubes partially ordered patterns	*cpTi/* smooth	Anodization	*70 - 80 nm/* NA	100 - 200 nm	*FE-SEM, AFM/* **different surface chemistry** between test and control implants as determined by XPS	hOBs	- greater bone mineral deposition on the substrates with 70 - 80 nm tubes (75% more calcium deposition) after 3 weeks of culturing compared to the smooth substrates	[143]
Nanotubes partially ordered patterns	*cpTi/* polished	Anodization	*30 nm, 80 nm/* NA	NR	*FE-SEM/* **NR** - but different fabrication methods employed for test and control substrates	mouse derived macrophage cell line	- enhanced macrophage adhesion and proliferation after 4, 24 and 48 hours on the substrate with 80 nm tubes compared to the corresponding with 30 nm and the control polished substrate - the secretion of the proinflammatory cytokine TNF-α and chemokine MIP-1α as evaluated by qPCR were downregulated across the substates with 80 nm tubes after 24 and 48 hours of culturing compared to the control substrates - the secretion of the chemokine MCP-1 evaluated by qPCR was downregulated across the substates with 80 nm tubes after 48 hours of culturing compared to the control substrates	[144]
Nanotubes partially ordered patterns	*cpTi/* flat	Anodization	*30 - 40 nm, 70 - 80 nm/* NA	NR	*FE-SEM, AFM/* **different surface chemistry** between test and control implants as determined by XPS	murine derived macrophage cell line, mouse derived pre-osteoblast cells and human umbilical vein	- higher protein adsorption on the substrates with 70 – 80 nm tubes after 3 hours compared to the 30 – 40 nm tubes and the flat controls - decreased adhesion and proliferation of macrophages after 1, 2 and 3 days on the nanotubular surfaces and especially the substrate with 70 – 80 nm tubes compared to the 30 – 40 nm tubes and the flat controls - decreased expression of TNF-α and IL-1 β and increased expression of IL-10 and ARG-1 after 12 hours of culturing on substrates with 70 – 80 nm compared to the 30 – 40 nm tubes and the flat	[145]

						endothelial cells	controls as evaluated by immunofluorescence and qPCR promoting M2 polarization - enhanced osteogenic activity by higher expression of ALP, OPN, OC and COLX after 24 and 72 hours culturing with CM from macrophages on substrates with 70 – 80 nm tubes as evaluated by qPCR - enhanced angiogenesis after 24 hours culturing with CM from macrophages on substrates with 70 – 80 nm tubes as evaluated by qPCR	
Nanotubes partially ordered patterns	*cpTi/* polished	Anodization	*30 nm, 100 nm/* NA	NR	*FE-SEM, AFM/* **NR -** but different fabrication methods employed for test and control substrates	mice BMSCs, mice derived macrophage cell line	- increased expression of osteoblastic differentiation genes BMP-2 and Runx2 determined by qPCR on substrates with 100 nm tubes after culturing of BMSCs for 3 days compared to the 30 nm and polished control substrates - enhanced osteogenic activity by higher expression of ALP as determined by qPCR after 1 week on substrates with 100 nm tubes and mineralization after 3 weeks - a lower M1/M2 ratio was detected across substrates with 30 nm tubes as indicated by a higher expression of ARG-1 and IL-10 determined by qPCR and verified by immunofluorescence after 3 days - a higher M1/M2 ratio was detected across substrates with 100 nm tubes as indicated by higher expression of iNOS and IL-6 determined by qPCR and verified by immunofluorescence after 3 days - increased expression of osteoblastic differentiation genes BMP-2 and Runx2 determined by qPCR on substrates with 30 nm tubes after culturing of BMSCs in corresponding topography-mediated macrophage CM for 3 days compared to the 100 nm and polished control substrates - enhanced osteogenic activity by higher expression of ALP determined by qPCR on substrates with 30 nm tubes after culturing of BMSCs in corresponding topography-mediated macrophage CM after 1 week	[133]

Nanotubes partially ordered patterns	*cpTi/* polished	Anodization	*30 nm, 80 nm/* NA	102.4 ± 13.2 nm and 679.7 ± 21.7 nm	*FE-SEM/* **NR** - but different fabrication methods employed for test and control substrates	human monocyte/ macrophage cell line, human BMSCs	- higher proliferation and migration of BMSCs when cultured in corresponding topography-mediated macrophage CM on the substates with nanotubes compared to the polished controls after 7 days, and after 24 hours, respectively - enhanced osteogenic activity of BMSCs and ECM mineralization when cultured in corresponding topography-mediated macrophage CM on the substates with nanotubes after 7, 14 and 21 days - osteoclastic activity was affected by BMSCs cultured in 30 nm substrates with corresponding topography-mediated macrophage CM as they expressed the lowest amount determined by ELISA of RANKL, M-CSF, and highest OPG after 7 days of culturing	[132]
Nanopillars partially ordered patterns	*cpTi/* polished	Block copolymer templated anodization	*21 nm/* approx. 30 nm [146]	15 nm	*SEM, AFM/* **different surface chemistry** between test and control implants as determined by XPS [147]	Coculture of human bone marrow stromal cells (hBMSCs) and human bone marrow hemato-poietic cells (hBMHCs)	- enhanced osteogenic activity by higher expression of ALP as determined by qPCR on substrates with 15 nm nanopillars compared to the polished substrates after 14 and 28 days of coculturing - the expression of TRAP was decreased based on qPCR and histochemical analysis of the substrates with the nanopillars after 28 days, while OPG was elevated on the same substrates after 28 days - the expression of IL-6 was elevated determined by qPCR on substrates with 15 nm nanopillars compared to the polished substrates after 28 days - the expression of OPN and calcium deposition was higher on substrates with 15 nm nanopillars after 28 days assayed by immunofluorescence	[148]
Nanorods partially ordered patterns	*cpTi/* flat	Anodization	*20 nm/* (0.88 ± 0.02) × 10^{10}/cm^2 - Low density; (1.79 ± 0.04) × 10^{10}/cm^2 - Medium	100 nm	*SEM, AFM/* **Only the elemental composition of Ti was shown to be the same between test and control substrates** as determined by EDS and EPMA	mouse derived pre-osteoblast cells	- the substate with medium density nanorods promoted protein adsorption after 4 hours and cell adhesion after 30, 60 and 120 min of incubation compared to the control flat substate and the low and high density nanorod substrates - enhanced cell proliferation on medium density nanorods after 1, 3 and 5 days compared to all other surfaces - enhanced osteogenic activity by higher expression of ALP determined by qPCR after 14	[149]

			density; (4.51 ± 0.06) × 10^{10}/cm^2 - High density				days on medium density nanorods compared to all other surfaces - increased expression of osteoblastic differentiation genes Runx2 determined by qPCR after 14 days on medium density nanorods compared to all other surfaces	
Nano-dots/pillars partially ordered patterns	*cpTi/* polished	Anodization through a porous alumina mask	*28.1 ± 3.48 nm, 41.0 ± 5.58 nm, 55.5 ± 8.49 nm/* 40.1 ± 3.87 nm, 74.1 ± 11.8 nm, 115 ± 15.6 nm, respectively	15.4 ± 4.19 nm, 55.4 ± 3.94 nm, 100 ± 5.38 nm respectively	*SEM, AFM/* **NR -** but different fabrication methods employed for test and control substrates	hMSCs	- well-spread cells with highly organized cytoskeleton after 4 days of culturing on samples with 15 nm high dots - large FAs after 4 days of culturing on samples with 15 nm high dots assayed by immunofluorescence - enhanced osteogenic activity by higher expression of OPN and OC after 21 days of culturing on samples with 15 nm high dots assayed by immunofluorescence compared to the polished substrates	[150]
Nano-dots/pillars partially ordered patterns	*cpTi/* polished	Anodization through a porous alumina mask	*22.2 ± 3.81 nm, 30.5 ± 4.27 nm, 39.2 ± 6.78 nm/* 41.1 ± 4.32 nm, 75.8 ± 6.76 nm, 105 ± 10,2 nm, respectively	16.1 ± 3.81 nm, 53.5 ± 8.39 nm, 90.7 ± 6.34 nm respectively	*SEM, AFM/* **NR-** but different fabrication methods employed for test and control substrates	hMSCs	- enhanced osteoblastic differentiation based on higher expression of Runx2 on the substrates with 15 nm dots assayed by immunofluorescence after 2 and 21 days of culturing compared to the other nanopatterned surfaces and the polished substrates - increased FAs, in both number and size, on the polished substrates compared to the others surfaces. The substrates though with 15 nm dots showed FAs with a greater proportion of larger size compared to the other nanopatterned substrates	[151]
Semi-spherical nano-protrusions partially ordered patterns	*cpTi/* flat	Colloidal lithography	*238 ± 2 nm, 130 ± 2 nm, 88 ± 2 nm/* 462 ± 8 nm	186 ± 2 nm, 104 ± 2 nm, 51 ± 1 nm respectively	*SEM, AFM/* **identical surface chemistry** between control and test implants as determined by TOF-SIMS, TEM and XPS	hMSCs	- enhanced proliferation after 2 weeks of culture in osteogenic media on substrates with 238 nm compared to the substrates with 88 nm and the flat control substrate as evaluated by SEM - increased expression of the osteoblastic differentiation gene Runx2 after 2 weeks of culture in osteogenic media on substrates with 238 nm compared to the substrates with 88 nm and the flat control substrate determined by qPCR	[152]

							- increased osteogenic activity after 2 weeks of culture in osteogenic media on substrates by higher expression of ALP on substrates with 238 nm compared to the substrates with 88 nm and the flat control substrate as determined by qPCR - increased mineralization after 4 weeks by calcium phosphate deposition on substrates with 238 nm and 130 nm compared to substrates with 88 nm and the flat control substrate determined by TOF-SIMS	
Nanopit ordered patterns	*Polycaprolone/* flat	Photo-lithography	*30 µm/* NR	80 nm, 220 nm, 333 nm	*SEM/* **NR**	hMSCs	- increased cell adhesion on pits with 80 nm depth as expressed by vinculin after 3 days assayed by immunofluorescence compared to the the other surfaces and the flat control substrate - promoted osteoblastic differentiation on pits with 80 and 220 nm depth as expressed by Runx2 after 3 days assayed by immunofluorescence compared to the other substrates and the flat control substrate - higher osteogenic activity on pits with 220 nm depth as expressed by OPN and OC after 28 days identified by immunofluorescence compared to the other substrates and the flat control substrate	[126]
Nano-grooves ordered patterns	*Polysterene/* smooth	EBL, laser interference lithography (LIL) and reactive ion etching (RIE)	*500 – 75 nm (width) /* Nanogroove-to-ridge ratio 1:1, 1:3 and 3:1	158 - 33 nm (depth)	*SEM, AFM/* **NR**	rat femoral osteo-progenitors	- osteoblast-like cell alignment increased to grooves with dimensions down to 75 nm in width and 33 nm in depth assayed by immunofluorescence after 24 hours of culturing - calcium phosphate deposition was found to be aligned after 12 and 16 days to even smaller nanopatterns (50 nm width and 17 nm depth) - FAs resided mainly on top of the ridges assayed by immunofluorescence of vinculin after 24 hours of culturing with decreased FA alignment with decreased groov pitch - enhanced osteogenic activity by higher expression of ALP, OC, BSP, ColI and osteoblastic differentiation by higher expression of Runx2 after 3 and 6 days on grooved substrates confirmed by qPCR compared to the smooth control substrates	[128]

CpTi: commercially pure titanium, NR: not reported, NA: not applicable, FE-SEM: field emission scanning electron microscope, XPS: X-ray photoelectron spectroscopy, EPMA: electron probe microanalysis, OPN: osteopontin, BSP: bone sialoprotein, Ø: diameter, hMSCs: human mesenchymal stem cells, OC: osteocalcin, AFM: atomic force microscopy, EDS: energy dispersive X-ray spectroscopy, TOF-SIMS: time-of-flight secondary ion mass spectrometry, TEM: transmission electron microscopy, FAs: focal adhesions, ALP: alkaline phosphatase, Col: collagen, Runx2: runt-related transcription factor 2, XPS: X-ray photoelectron spectroscopy, hOBs: human osteoblasts, MIP-1α: macrophage inflammatory protein, qPCR: quantitative polymerase chain reaction, TNF-α: tumor necrosis factor - alpha, IL-1β: interleukin-1 beta, ARG: arginase 1, CM: conditioned medium, BMP-2: bone morphogenetic protein – 2, BMSCs: bone marrow mesenchymal stem cells, IL-10: interleukin 10, iNOS: inducible nitric oxide synthase, ECM: extracellular matrix, ELISA: enzyme-linked immunosorbent array, RANKL: receptor activator of nuclear factor kappa B ligand, TRAP: tartrate resistant acid phosphatase, M-CSF: macrophage-colony stimulating factor, OPG: osteoprotegerin, TOF-SIMS; time of flight secondary ion mass spectrometry

In summary, the majority of the *in vitro* studies conducted on titanium have studied the effects of random nanofeatures and partially ordered nanopatterns, and these studies are mainly performed by superimposing the nanotopography on polished surfaces, thus eliminating the biological effects that microtopography may provoke. Unfortunately, the production methods employed for the creation of the nanotopography have induced chemical alterations on the surface of the test implants. These chemical changes on the test implants differentiate them from their controls. Moreover, because the overwhelming majority of the studies reviewed here did not report on the chemical characterization of the surfaces used, the observed biological responses are difficult to attribute solely to the created nanotopography.
Nonetheless, all the presented *in vitro* studies have repeatedly observed enhanced osteogenic activity, osteoblastic differentiation and matrix mineralization towards nanopatterned implants. Furthermore, enhanced protein adsorption, cell-protein interactions leading to large focal adhesions, and MSC migration and proliferation are commonly observed.

1.6 *IN VIVO* STUDIES OF NANOTOPOGRAPHY AND OSSEOINTEGRATION

In vitro studies are necessary to initially delineate cellular and molecular interactions and acquire data to indicate the cytocompatibility of the substrates. However, *in vitro* conditions can rarely fully recapitulate the multifactorial and dynamic microenvironment of living tissues. As a direct consequence, *in vitro* findings may not be predictive of *in vivo* performance. For this reason, animal models are required to confirm the next step.

The major difference between *in vitro* and *in vivo* settings is the cellular interaction pattern, which implies that cells will not directly interact with the implant surface under *in vivo* conditions. The processes of implant hydration and protein adsorption with subsequent protein-cellular interactions are highly complex and thus far have been partly studied *in vitro*. After the insertion of the implant into its prepared site, it will immediately adsorb water molecules [153]. Proteins from blood plasma will subsequently adsorb to the hydrated surface. The specific protein profile adsorbed will be determined by the implant surface properties (topography, chemistry, wettability, crystallinity and charge) and further determine the cellular response [154]. Some of the interacting proteins will be associated with the host inflammatory response, such as fibrinogen and complement molecules, while others are involved in cell adhesion and migration, such as fibronectin and vitronectin [155]. It has been shown that vitronectin preferably adsorbs on nanoscale substrates,

enhancing osteoblast adhesion [156]. The protein layer will ultimately even affect proliferation and differentiation. Although the cells do not interact directly with the implant surface, they can sense topographical cues as well as the ECM though the extension of structures, such as filopodia. Filopodia are responsible for the cytoskeletal reorganization observed under cell migration to identify sites for attachment. This attachment occurs via integrins. Surface integrin receptors bind to specific peptide ligands that recognize RGD (arginine-glycine-aspartate acid) sequences located in ECM proteins. Integrin binding leads to focal adhesions (FAs) that further affect the arrangement of the cytoskeleton and influence intracellular genetic pathways, ultimately leading to cell proliferation, migration and differentiation [157]. A principal difference between nanostructured implants and microroughened implants is that the former provides a larger area to adsorb proteins and more adhesion sites for integrins.

In vivo studies evaluating the biological responses induced by ordered surface nanotopography are limited. There are technical challenges regarding the reproduction of identified useful patterns from soft materials onto metallic materials. To the author´s knowledge, only surfaces with semiordered or randomly produced nanotopography on titanium implants have been evaluated in bone, and they are presented below.

Herein, we review the effects of nanotopography on osseointegration observed *in vivo* (*Table 3*). Only studies using Ti implants have been included, and these implants present geometrical shapes similar to that of dental endosseous implants (cylindrical or screw shaped or a combination); thus, the following are excluded: disc-formed implants [158], polymers [159], biocomposites [160], HA- or CaP-coated implants [161, 162], nanotubes further treated by UV altering wettability [163], and chemically [164] or electrically modified conditioned implants that affect surface charge [165].

Table 3. Description of in vivo studies using nanopatterns on titanium surfaces and their effects on osseointegration.

Pattern shape and degree of order	**Pattern material/** *macroscopic design/* **microroughness**	**Fabrication method**	***Dimensions***		***Surface characterization (topography)/* chemistry**	***Animal modeling***	***Main biological outcome***	***Ref***
			***Diameter/* interparticle distance or density**	***Height/ depth***				
Nanosized random spherical globular patterns	***Ti6Al4V (1), cpTi (2)/*** *screw- shaped implants/* **machined**	Laser ablation	NR	NR	FE-SEM, AFM/ **NR**	Rabbit tibia (1), Rabbit femur and tibia (2)	- higher torque removal after 8 weeks (270% increase) and 6 months (170% increase) as compared to machined surfaces - intimate bone growth on the nanosized surface titanium oxide	[166, 167]
Nanotubes partially ordered patterns	***cpTi/*** *screw-shaped implants/* **polished**	Anodization	30 nm, 80 nm/ NA	102.5 ± 13.2 nm and 679.7 ± 21.7 nm	FE-SEM/ **NR -** but different fabrication methods employed for test and control substrates	Rat femur	- higher BV% and BIC% at substates with 30 nm as compared to 80 nm and polished controls after 2, 4 and 12 weeks	[132]
Nanotubes partially ordered patterns	***cpTi/*** *cylindrical implants/rods/* **polished**	Acid etching and anodization	30 nm, 100 nm/ NA	NR	*FE-SEM, AFM/* **NR** - but different fabrication methods employed for test and control substrates	Mice, femur	- thicker trabecular bone around the implants with 30 nm tubes as determined by measures on µCT after 3 weeks in comparison to implants with 100 nm and polished controls - higher push-in resistance of the implants with 30 nm tubes after 3 weeks	[133]

								- a lower macrophage M1/M2 ratio could be seen IHC across the implant surface with 30 nm tubes while the highest ratio could be seen at 100 nm as compared to control polished surfaces	
Nanotubes partially ordered patterns	***cpTi/*** *cylindrical implants/rods/* **machined**	Anodization	30 nm, 70 nm, 100 nm/ NA	NR	FE-SEM/ **NR** - but different fabrication methods employed for test and control substrates	Minipigs, frontal skull bone		- enhanced osteogenic activity in implant adherent cells as determined by higher expression of ALP and ColI and osteoblastic differentiation by higher expression of Osx determined by qPCR after 1, 2, 3, 4 and 5 weeks on the nanostructured implants and especially 70 nm on all time points and compared to machined implants - enhanced TRAP expression in peri-implant bone as determined by qPCR after 1, 2, 3, 4 and 5 weeks on the nanostructured implants and especially 70 nm on all time points and compared to machined implants - higher BIC at implants with nanotubes as compared to machined surfaces at 3, 5 and 8 week, especially at 70 nm tubes	[168]
Nanorods partially ordered patterns	***cpTi/*** *cylindrical implants/rods/* **flat**	Anodization	20 nm/ (0.88 ± 0.02) x 10^{10}/cm^2 - Low density; (1.79 ± 0.04) x 10^{10}/cm^2 - Medium density; (4.51	100 nm	SEM, AFM/ **Only the elemental composition of Ti was shown to be the same between test and control**	Rabbit, tibia		- enhanced push-out forces of implants with medium density (1.79 ± 0.04) x 10^{10}/cm^2) nanorods as compared to plain Ti-implants after 12 weeks	[149]

			± 0.06) x 10^{10}/cm^2 - High density		**substrates as determined by EDS and EPMA**			
Nanopillars partially ordered patterns	***cpTi/*** *cylindrical implants/rods/* **polished**	Block copolymer templated anodization	21 nm/ approx. 30 nm [146]	15 nm	SEM, AFM/ **different surface chemistry** between control and test implants as determined by XPS [148]	Rabbit, femur	- 20% higher BIC in the nanopillar surfaces after 2 months of healing as compared to polished controls	[148]
Nano-protrusions partially ordered patterns	***cpTi/*** *combination of screw shaped and cylindrical implants/* **machined**	Colloidal lithography	60 nm, 120 nm, 220 nm/ 157 nm, 238 nm, 436 nm, respectively	45 nm, 90 nm, 160 nm, respe-ctively (appr 3/4 of Ø)	SEM, optical profilometry/ **identical surface chemistry** between control and test implants as determined by XPS	Rat, tibia	- enhanced BIC on implants with 60 nm semispherical protrusions as compared to 120 and 220 nm and machined control implants after 28 days	[137]

CpTi: commercially pure titanium, NR: not reported, NA: not applicable, FE-SEM: field emission scanning electron microscope, AFM: atomic force microscopy, BV: bone volume, BIC; bone-implant contact, ALP: alkaline phosphatase, Col: collagen, Osx: osterix, qPCR: quantitative polymerase chain reaction, TRAP: tartrate-resistant acid phosphatase, µCT: microcomputed tomography, IHM: immunohistochemistry, Ø: diameter

In summary, the *in vivo* studies reviewed repeatedly report enhanced BIC and biomechanical anchorage. The limitations regarding *in vitro* studies are also apparent in the *in vivo* studies reviewed. The fabrication procedures mainly adopted for the production of nanoscale topographies on Ti implants used *in vivo* involve etching with or without peroxidation, etching and grit blasting, anodic oxidation and different coating techniques. All these procedures result in a random nanotopography with the exception of anodic oxidation at low voltage, which leads to partially ordered nanotubes. However, all of these methods can cause alterations in the surface chemistry since entities from either the solutions used or the blasting media or the coating material can become incorporated into the oxide layer. Thus, the biological effects provoked are difficult to assign to a specific surface property, such as the chemistry nor nanotopography. Additionally, topographic features on the microscale has been present on the implants used in a high proportion of these *in vivo* studies, further impeding the interpretation of the biological responses. Finally, a remarkable observation is the limited volume of studies that have evaluated the molecular and cellular responses towards nanopatterned implants.
In conclusion, *in vitro* but especially *in vivo* studies on the nanotopography of titanium implants in a partial or highly ordered pattern configuration are limited, which is associated with the methods required to produce highly ordered patterns, such as X-ray, electron or laser lithography, nanoimprinting and replica molding, which are technically demanding and inapplicable to curved materials. Furthermore, they require serial production in short arrays, which is costly in terms of time and resources. Additionally, the production setup is highly expensive.

Despite the limitations presented above, *in vitro* and *in vivo* assessments of nanopatterned titanium implants indicate that they modulate the initial inflammatory response by downregulating the expression of proinflammatory cytokines while enhancing the production of anti-inflammatory cytokines. Furthermore, the differentiation of MSCs to osteoblastic precursors is enhanced in the short term with increased mineral deposition in the long term. In this thesis, these responses are reevaluated for implants with identical chemistry as well as microtopography, with the only variable between the control and test implants being the nanotopography. Such nanotopographies have been reproduced on titanium implants with colloidal lithography. Our group has previously shown that semispherical nanoprotrusions with a diameter of 60 nm promote bone formation and bone-to-implant contact after 28 days. However, the molecular and cellular responses to these effects have not been explored.

2 AIM

The overall aim of this thesis was to study the pure influence of predetermined and well characterized topographic nanopatterns on titanium implants on the process of osseointegration in an *in vivo* experimental model as well as in human.

2.1 SPECIFIC AIMS

- The aim of our first study was to evaluate the implant-tissue interface by exploring the cellular and molecular events underlying the enhanced osseointegration using cylindrical implants embellished with 60-nm semispherical nanopatterns.

- Due to methodological improvements, the same nanopatterns could be transferred to complex three-dimensional titanium implants resembling clinical dental implants. The aim of this study was to reveal the cellular and molecular events, both in a temporal and spatial manner, occurring early in the healing process. This was achieved in combination with visualization of the interface with ultrastructural methods.

- The mid-early to late healing events were the focus of the third study, using methodologies within molecular evaluation at the interface, cellular structural relationships evaluated under the light microscope and biomechanical evaluation of the interface. The same implants and topography as used in the second study was used even in this study.

- This study constitutes the transition from experimental animals to human practice. Mini implants with almost identical geometry and topography as in our second and third studies were used. A comparison of the molecular events taking place at the healing site in human maxillary bone was the main aim in this study.

3 MATERIALS AND METHODS

3.1 IMPLANTS, IMPLANT PREPARATIONS AND NANOPATTERNING

The implants used in Paper I were machined implants made of commercially pure titanium (Ti) (grade II) but had threads only at the top (2.0 mm in diameter, 0.5 mm in length), intended to engage the cortical bone (*Figure 5*A). The part of the implant facing the bone marrow was specially designed as a cylinder (1.8 mm in diameter, 1.5 mm in length). Only the cylindrical part was nanopatterned, and the biological response was studied and compared to the native machined surface as control. All implants (test and control) were sputter-coated with titanium (10-nm-thick layer) unifying the chemistry of the implants.

The implants used in Papers II and III were made by turning commercially pure Ti (grade IV) and were screw-shaped (2.0 mm diameter, 2.3 mm in length) (*Figure 5*B). Four different surface modifications of the implants were made to supply implants with different combinations of micro- and nanoscale topographies: polished surface (P), polished nanopatterned surface (PN), machined surface (M) and machined nanopatterned surface (MN). Electrochemical polishing of the selected surfaces was performed using a perchloric acid-based electrolyte at 22.5 V constant potential. To create a homogeneous chemistry on the implant surfaces, a 30-nm-thick titanium layer was sputter-coated on all the implants.

In Paper IV, screw-shaped machined implants made of commercially pure Ti (grade II) were used (*Figure 1*B). The dimensions of the implants were 2 mm in diameter and 5 mm in length. Two subsets of implants were tested, one group with a machined surface (M) and another with superimposed nanotopography (MN). All implants had identical surface chemistry produced by a 30-nm-thick titanium layer that was sputter-coated.

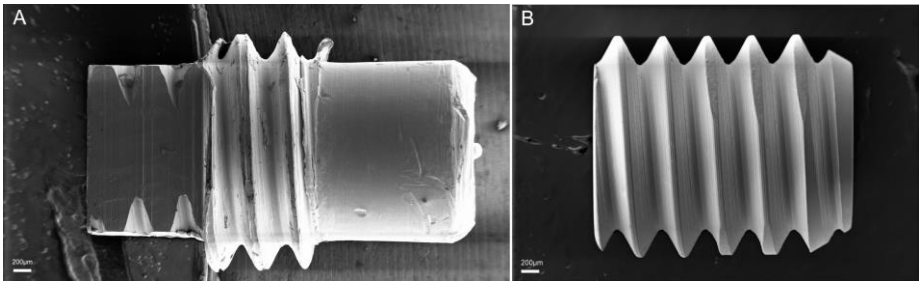

Figure 5. SEM micrographs showing the overall geometry of the implants used. The implants used in Paper I (A) and screw-shaped implants used in Papers II, III and IV (B).

The nanopatterning of all implants (Paper I - cylindrical part, Papers II-IV - entire implant length) was performed using colloidal lithography. In brief, all the implants were cleaned in acetone, isopropanol and Milli-Q water (Millipore Corp, USA) ultrasonic baths and then dried under a nitrogen stream. To produce a sufficient positive surface charge on the implant surfaces, they were soaked in 5% wt/wt aluminum chloride hydroxide (chlorohydrol, Summit Reheis, Huguenot, NY, USA) solution for two minutes, rinsed in Milli-Q water and blow-dried by nitrogen. Then, the charged implants were soaked in a 2% wt/wt colloidal solution of negatively charged spherical nanoparticles (105 ± 5-nm-diameter surfactant-free white polystyrene latex, Invitrogen Corp, Carlsbad, CA, USA – Paper II and III; 41 ± 6-nm-diameter surfactant-free white polystyrene latex, Invitrogen Corp, Carlsbad, CA, USA – Paper IV) for 1 minute, allowing the nanoparticles to self-assemble on the implant surface because of electrostatic interactions. Nonadsorbed particles were removed from the implant surfaces by extensive rinsing in Milli-Q water. The adsorbed polymeric particles were further fixed to the surface by heat treatment above the polystyrene glass transition temperature (approximately 110°C). This was done by soaking the implants in hot ethylene glycol (Sigma-Aldrich, Stockholm, Sweden) for 10 seconds, followed by rinsing under Milli-Q water and blow-drying by nitrogen. The dimensions of the polymeric particles were reduced to approximately 60 nm in diameter by exposure to microwave oxygen plasma (plasma strip TePla 300PC, TePla AG, 150 W, 5 minutes). Furthermore, all implants were sputter-coated with a thin Ti layer to ensure the same surface chemical composition (*Figure 6*). Finally, all the implants except those in Paper I were annealed at 500°C (High Temperature Furnace, AWF 12/65, Lenton, Parsons Lane, Hope, UK) for 5 hours and kept in 70% ethanol until surgery.

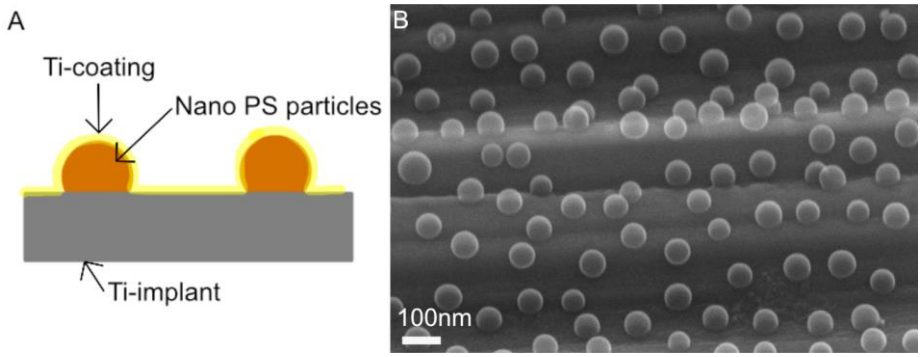

Figure 6. Schematic cross-section of the nanopatterns on the Ti implant (A) and SEM micrograph showing nanoparticles superimposed on the underlying microrough titanium surface (B).

3.2 IMPLANT SURFACE CHARACTERIZATION

3.2.1 **SURFACE TOPOGRAPHY**

The surface topography, from the micro- to nanoscale, was characterized by a combination of different methods [169].

The microscale surface roughness of all implants (Papers I, II, III and IV) was characterized by an optical profiler (Wyko NT 1100) in vertical scanning interferometry (VSI) mode. SPIP software (Image Metrology A/S, Denmark) was used to calculate the surface roughness parameters. Due to the limited lateral resolution of the optical profiler being well below the size of the nanopatterned semispheres, only the surfaces of the control implant group were analyzed. Instead, the characterization of the nanopatterns and background roughness was performed with atomic force microscopy (AFM) (Bruker Dimension 3100 SPM) (Papers II and III). The measurements were performed on polished silicon wafers due to the limited vertical operating range of the method.

Finally, scanning electron microscopy (SEM) (Zeiss Supra 40VP) imaging was performed directly on all implant types (Papers I, II, III, and IV), enabling the visualization of the lateral dimensions and distribution of the nanopatterned semispheres, as well as the background microroughness. SEM images were processed by image analysis software (ImageJ, U.S. National Institutes of Health, Bethesda, Maryland, USA, http://imagej.nih.gov/ij/, 1997-2014) to

quantify the nanofeature diameter, surface coverage, density, interparticle distance and induced surface area.

3.2.2 SURFACE CHEMISTRY

The surface chemistry of the implants was analyzed by different methods [169].

The surface chemical composition of the implants in Paper I and IV was analyzed by a surface energy-dispersive X-ray spectroscopy (EDX) system (IXRF Systems, USA and Oxford Instrument, UK respectively) integrated into a SEM instrument.

The surface chemistry of the implants in Papers II and III was analyzed by X-ray photoemission spectroscopy (XPS, Kratos AXIS Ultra^{DLD}, Kratos Analytical, Manchester, UK). The analysis area was below 1 mm^2, with most of the signal originating from a 700 × 300-µm area. Survey spectra were run within the analysis to detect the elements that were present in the surface layer. The relative surface compositions were obtained from the quantification of detailed spectra run for each element. Additionally, the high-resolution carbon spectra were curve fitted, showing chemical shifts within the carbon signals because of different functional groups.

Finally, time-of-flight secondary ion mass spectrometry (TOF-SIMS V, ION-TOF Technologies GmbH, Münster, Germany) was used in Paper II, III and ÍV to further verify the chemical homogeneity of the outermost 10 Å of the surfaces. Nanopatterned (PS nanoparticles coated by a 30-nm Ti layer) and control (only a 30-nm Ti layer) surfaces before and after the heat treatment (500°C for 5 hours) were evaluated. Since a chemical difference could be caused by the presence of uncoated PS nanoparticles on nanopatterned surfaces, ion signals associated with Ti (Ti^+, TiO^+, TiO_2H^+, $Ti_2O_3^+$, $Ti_2O_4H^+$, $Ti_3O_5^+$, $Ti_3O_6H^+$, $Ti_4O_6^+$, $Ti_4O_7^+$, TiO_2^-, TiO_3H^-, $O_4Ti_2^-$, $Ti_2O_5H^-$, $Ti_3O_6^-$, and $Ti_3O_7H^-$) and polystyrene ($C_4H_3^+$, $C_4H_7^+$, $C_4H_9^+$, $C_5H_3^+$, $C_5H_9^+$, $C_6H_5^+$, $C_7H_7^+$, C_3H^-, CNO^-, C_4H^-, NO_3^-, and $C_5H_2^-$) were compared.

3.3 SURGICAL PROCEDURE

3.3.1 ANIMAL STUDIES: PAPERS I, II AND III

The animal studies were approved by the Local Ethical Committee for Animal Research in Gothenburg (Dnr 301/2009 and Dnr 36/2012). Male Sprague-

Dawley rats (250-380 g) were used. The surgery was performed under general anesthesia introduced with isoflurane inhalation (4.1% with an air flow of 650 mL/min) in a Univentor 410 anesthesia unit and maintained by the continual administration of isoflurane (2.3% with an air flow of 450 mL/min) via a mask. After shaving and cleaning (chlorhexidine 0.5 mg/ml) the recipient leg, the medial aspect of the proximal tibial metaphysis was exposed through skin incision, muscle reflection and periosteal elevation after infiltration with a local anesthetic solution (1 ml lidocaine with epinephrine; 10 ml/ml + 5 µg/ml). The implantation sites were prepared under profuse saline irrigation. Two implants were inserted unicortically in each proximal tibial metaphysis, employing a predesigned placement schedule to ensure rotation for the various implant surfaces (proximal/distal position, right/left side) (*Figure 7*). After installation, the myocutaneous flap was closed in layers subcutaneously by resorbable polyglactin sutures (Vicryl 4-0, Ethicon), whereas the skin was adapted and closed with transcutaneous resorbable poliglecaprone sutures (Monocryl 4-0, Ethicon). The rats received postoperative buprenorphine analgesic (Temgesic 0.03 mg/kg) subcutaneously and were housed in groups with food and water *ad libitum*.

The retrieval of the implants was also performed under general anesthesia by blunt dissection through the skin and subcutaneous tissues. The animals were thereafter euthanized using an overdose of sodium pentobarbital (pentobarbital sodium vet; APL 60 mg/ml).

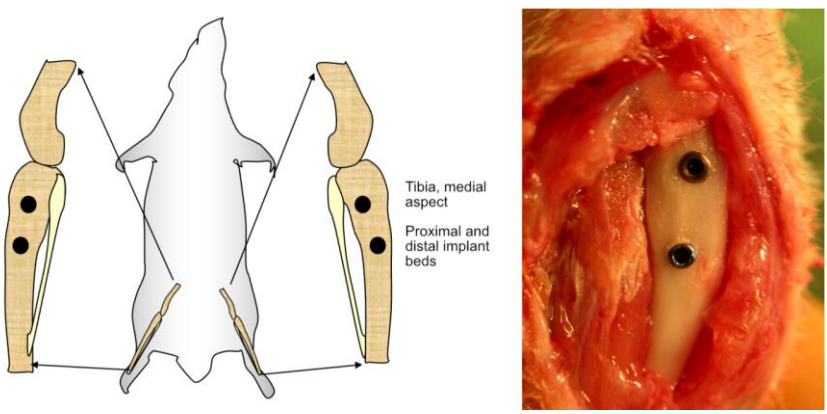

Figure 7. *Schematic drawing of the implant sites in rat tibia and a photograph showing the implants after installation.*

3.3.2 HUMAN STUDY: PAPER IV

The study protocol was approved by the Ethical Committee on Human Subject Research at the University of Göteborg, Sweden (Dnr 620-16). The participants were recruited at the clinic of oral and maxillofacial surgery, Sahlgrenska University Hospital. They were all referred to the clinic for implant placement in the posterior maxilla. Patients with good general health devoid of active oral pathologies (marginal or apical periodontitis) were included. Pregnancy, ongoing smoking, uncontrolled metabolic diseases or medications affecting the immune system or bone metabolism and previous radiation therapy to the head and neck were conditions for exclusion. Ten patients were included, four men and six women, between the ages of 42 and 87 years with a mean age of 61.7 years. Informed written consent to participate in the study was obtained for each patient.

After local anesthesia, a mucoperiosteal flap was reflected buccally and palatally exposing the recipient bone. Only patients with enough bone volume, judged radiographically, to receive implants in the posterior maxilla without the need for prior augmentation were included. Clinical implants were installed, and the experimental mini implants were installed more posteriorly in the edentulous posterior maxilla. Each patient received a nanopatterned and a control mini implant on the same side of the maxilla. A single 2.0-mm-diameter twist osteotomy drill was used at 1500 rpm under profuse sterile saline irrigation. Drills reached a depth of 5 mm whereupon the self-tapping mini implants could be installed and good primary stability ensured. The wound was thereafter closed with nonresorbable polyamid 6 sutures (Ethilon 4-0, Ethicon). A submerged implant installation technique was used and performed under antibiotic coverage given to the patients as one prophylactic dose 1 hour before surgery (2 grams amoxicillin or 600 mg clindamycin perorally). Appropriate analgesics were prescribed postoperatively to each patient. The wound was clinically evaluated 10-14 days postoperatively for signs of infection, and the sutures were removed at that time. The implants were allowed to heal for 6-8 weeks. After that, the surgical site was reentered under local anesthesia, and the clinical implants were provided with healing abutments. The mini implants were removed by reverse threading and immediately preserved in tubes containing RNA preservation medium (*RNALater*, QIAGEN GmbH, Hilden, Germany) for subsequent qPCR analyses. The surgical site was again reapproximated and closed with resorbable polyglactin sutures (Vicryl 4-0, Ethicon).

3.4 QUANTITATIVE POLYMERASE CHAIN REACTION

The implant-adherent cells of all the manually retrieved implants (Papers I, II, II and IV) were subjected to quantitative polymerase chain reaction (qPCR) to provide quantitative measurements of gene expression [170, 171]. The retrieval was performed taking strict precautions for RNA preservation. In brief, the retrieved implants and therefore the adherent biological material were placed in RNA-later solution until analysis. The samples were homogenized using RLT buffer with b-mercaptoethanol and a TissueLyser® instrument (Qiagen GmbH, Hilden, Germany), followed by centrifugation at 16,000 *g* for 3 minutes. RNA was then extracted from the separated aqueous phase using an RNeasy Micro-Kit (Qiagen GmbH). The RNA was purified by DNAse treatment to eliminate contamination from genomic DNA. Reverse transcription (RT) was then performed using a Grandscript cDNA synthesis kit (TATAA Biocenter AB, Gothenburg, Sweden). Complementary DNA (cDNA) was stored at -20°C until separate qPCR analysis. Before qPCR, predesigned validated primers targeting the genes of interest (*Table 4*) were purchased from TATAA Biocenter AB, Gothenburg, Sweden. Additionally, a panel of reference genes was screened in random samples, representing all the groups and time points. The stability of the expression of the reference genes was evaluated using geNorm [172] and Normfinder [173] software to determine the best reference gene(s) for normalization. The analysis used a 10-ml reaction volume in duplicate on a CFX96 platform (Bio-Rad Laboratories, Inc., Hercules, USA) with TATAA SYBR GrandMaster Mix (TATAA Biocenter AB, Sweden). The quantities of the genes were normalized to the expression of the chosen reference gene. The normalized relative quantities were calculated using the delta-delta C_q method and 90% PCR efficiency ($k*1.9^{\Delta\Delta cq}$) [174].

Table 4. The genes of interest analyzed in each study.

Study	Biological processes	Biological markers	Representative genes
In vivo I	Inflammation	Cytokines	TNF-α
	Bone formation	Osteogenic activity and osteoblast differentiation	ALP OC RUNX2
	Bone resorption	Osteoclast markers	CatK CTR
In vivo II	Inflammation	Cytokines	TNF-α IL-1β
	Cell migration and recruitment	Chemokines	CXCR4 MCP-1
	Cell adhesion and attachment	Integrins	Integrin α5 Integrin β1
	Bone formation	Osteogenic activity	ALP OC
	Bone resorption	Osteoclast markers	TRAP CatK
	Cell death	Apoptosis	Caspase 3
In vivo III	Inflammation	Cytokines	TNF-α IL-1β
	Bone formation	Osteogenic activity	ALP OC
	Bone resorption	Osteoclast markers	TRAP CatK
	Bone remodeling	Osteoblast-osteoclast coupling	RANK RANKL OPG
In vivo IV	Inflammation	Cytokines	TNF-α IL-6 MCP-1 IL-10
	Bone formation	Osteogenic activity and osteoblast differentiation	ALP OC RUNX2 BMP-2
	Bone resorption	Osteoclast markers	CatK CTR
	Bone remodeling	Osteoblast-osteoclast coupling	RANK RANKL OPG

3.5 HISTOLOGY, IMMUNOHISTOCHEMISTRY AND HISTOMORPHOMETRY

Implant-bone specimens were retrieved *en bloc* and fixed in formaldehyde, decalcified in 10% EDTA for 10-12 days, dehydrated in an ascending series of ethanol, cleared with xylene and embedded in paraffin. When the paraffin was still in the melting stage, the implants were unscrewed, and the embedding procedure was continued. Subsequently, 3–5-µm-thick sections were produced and mounted on glass and stained with hematoxylin and eosin (H&E). The slides were studied under light microscopy (Nikon Eclipse 600, Japan), and the formation of new bone, bone structure, surrounding cells and soft tissue were evaluated.

Paraffin-embedded sections for immunohistochemistry were mounted on poly-L-lysine slides (Menzel GmbH and Co KG, Braunschweig, Germany) and incubated with antibodies against cellular/molecular markers of interest. Primary antibodies targeting CD163 and periostin (Abcam, Cambridge, UK) were used in Paper I, and CD68 and periostin were used in Paper II. CD163 and CD68 antibodies target surface receptors on macrophages, whereas periostin antibodies target proteins intracellularly, in osteoprogenitors, and extracellularly, indicating active intramembranous bone formation. Negative controls were prepared by omission of the primary antibody and incubated with 1% BSA in PBS. All slides were evaluated qualitatively under light microscopy (Nikon Eclipse 600, Japan). In addition, quantification of CD163- and periostin-positive cells was performed in well-preserved tissue between implant threads (Paper II). Under a higher power field (magnification x40), positive cells extending 200 µm from the implant surface were counted manually in relation to the area studied (cells/mm^2).

The bone implant blocks intended for histomorphometry (Paper III) were fixed and dehydrated as previously described and thereafter embedded in acrylic resin (LR White, London Resin Company Ltd, Berkshire, UK). The implants were sectioned along their long axis (EXACT® cutting and grinding equipment, EXACT® Apparatebau GmbH & Co, Norderstedt, Germany) [175], and the ground sections were prepared and stained with 1% toluidine blue. The sections were examined under an optical microscope (Nikon Eclipse E600, Japan). The proportion of bone within the threads in relation to the total area (bone area, BA%) and the proportion of the implant surface in direct contact with bone in relation to the total surface length (bone-to-implant contact, BIC%) were quantified.

3.6 REMOVAL TORQUE

After surgical exposure of the implants in the proximal tibia (Paper III), a special hexagonal screwdriver connected to the torque test machine was fitted into the implant internal hexagon. The torque measuring equipment is a custom-made device evolved from a previously used device [176, 177] and was calibrated prior to angular torque measurement. For each particular test, the torque was registered versus the rotation angle and followed in real time. After the breakpoint was reached, the procedure continued under constant rotation to determine the plateau phase before complete failure.

3.7 STATISTICS

Statistical comparisons of the gene expression (Papers I, II and III), removal torque (Paper III) and histomorphometry results (Paper III) were performed using nonparametric statistical tests. The Kruskal-Wallis test was used to determine statistically significant differences between the different time points. Furthermore, the Mann–Whitney test was used to determine the statistically significant differences between the implant types at each time point.

In addition to these statistics, in Paper III, Pitman's test was used to study possible time trends between the time points and significant differences. As no major trends could be observed, the time points were pooled, thereby enhancing the statistical power. This was possible since every individual rat had all the implant types represented and was studied only at one time point. The pooled data were also evaluated using two-way multivariate analysis of variance (MANOVA) to statistically determine whether the effects of nano- and microtopographies were dependent on each other and whether there were interaction effects between the two variables on all dependent variables (removal torque, histomorphometry and gene expression). Only dependent variables that showed significant differences using comparative tests on the pooled data were evaluated by two-way MANOVA.

Finally, in Paper IV, and prior to the conduction of the study, a statistical power analysis in an effort to estimate the minimum sample size required to detect an effect was calculated. The hypothesis was to detect gene expression differences in cells adherent on the machined versus nanopatterned implants. Intended statistical power was set to $(1 - \beta) = 0.95$, with type-1 error probability $\alpha = 0.05$ and type-2 error probability $\beta = 0.05$. The G* power tool was used (software version 3.1.9.2) [178] based on previous comparable studies on gene

expression analysis in human [179] indicating that the required sample size per group would be n = 10.

The statistical significant differences in the gene expression between the two implant types was determined with Wilcoxon Signed Ranks in a paired analysis. Further, a Spearman correlation analysis was applied between the expression of different genes and the collected patient demographic data (age, gender, current systemic illness, current medications and the healing time period whether 6, 7 or 8 weeks after implantation).

All statistical tests were conducted with IBM® SPSS® Statistics Versions 22 and 25. *P*-values < 0.05 were considered statistically significant.

The analyses used in the different studies are summarized in *Table 5*.

Table 5. Summary of analyses used in each study.

<table>
<tr><th colspan="7">In vivo I</th></tr>
<tr><td rowspan="3">Time point</td><td rowspan="3">No. of rats</td><td colspan="2">qPCR</td><td colspan="3">Histology and SEM-EDX</td></tr>
<tr><td rowspan="2">Samples retrieved per implant type</td><td rowspan="2">Samples analyzed per implant type (n)</td><td rowspan="2">Samples retrieved per implant type</td><td>Histology</td><td>SEM-EDX</td></tr>
<tr><td>Samples analyzed per implant type (n)</td><td>Samples analyzed per implant type (n)</td></tr>
<tr><td>3 days</td><td>7</td><td>8</td><td>8</td><td>6</td><td>3</td><td>3</td></tr>
<tr><td>21 days</td><td>7</td><td>8</td><td>8</td><td>6</td><td>3</td><td>3</td></tr>
<tr><td>28 days</td><td>7</td><td>8</td><td>8</td><td>6</td><td>3</td><td>3</td></tr>
<tr><th colspan="7">In vivo II</th></tr>
<tr><td rowspan="3">Time point</td><td rowspan="3">No. of rats</td><td colspan="2">qPCR</td><td colspan="3">Histology/IHC and SEM</td></tr>
<tr><td rowspan="2">Samples retrieved per implant type</td><td rowspan="2">Samples analyzed per implant type (n)</td><td rowspan="2">Samples retrieved per implant type</td><td colspan="2">Samples analyzed per implant type (n)</td></tr>
<tr><td>Histology/ IHC</td><td>SEM</td></tr>
<tr><td>12 hours</td><td>16</td><td>10</td><td>10</td><td>6</td><td>3</td><td>3</td></tr>
<tr><td>1 day</td><td>16</td><td>9-10</td><td>10</td><td>6</td><td>1-2</td><td>3</td></tr>
<tr><td>3 days</td><td>16</td><td>10</td><td>10</td><td>6</td><td>3</td><td>3</td></tr>
<tr><th colspan="8">In vivo III</th></tr>
<tr><td rowspan="4">Time point</td><td rowspan="4">No. of rats</td><td colspan="3">Torque and qPCR</td><td colspan="3">Histomorphometry and BSE-SEM</td></tr>
<tr><td rowspan="3">Samples retrieved per implant type</td><td colspan="2">Samples analyzed per implant type (n)</td><td rowspan="3">Samples retrieved per implant type</td><td colspan="2">Samples analyzed per implant type (n)</td></tr>
<tr><td>Torq ue</td><td>qPCR</td><td>Histomor-phometry</td><td>BSE-SEM</td></tr>
<tr><td>6 days</td><td>16</td><td>10</td><td>10</td><td>6-7</td><td>6</td><td>6</td><td>6</td></tr>
<tr><td>21 days</td><td>16</td><td>10</td><td>10</td><td>7-10</td><td>6</td><td>6</td><td>6</td></tr>
<tr><td>28 days</td><td>16</td><td>10</td><td>10</td><td>10</td><td>6</td><td>6</td><td>6</td></tr>
<tr><th colspan="5">In vivo IV</th></tr>
<tr><td colspan="2" rowspan="2">Time point</td><td rowspan="2">No. of patients</td><td colspan="2">qPCR</td></tr>
<tr><td>Samples retrieved per implant type</td><td>Samples analyzed per implant type (n)</td></tr>
<tr><td colspan="2">6-8 weeks</td><td>10</td><td>10</td><td>10</td></tr>
</table>

4 RESULTS

4.1 PAPER I

4.1.1 IMPLANTS AND SURFACE CHARACTERIZATION

The surface topographies of the implants were either machined (M) or machined with a superimposed nanopattern (MN). The surfaces were characterized using optical profilometry and scanning electron microscopy (SEM). The optical profilometry analysis of the cylindrical part of the control M implants revealed microgrooves that were created during the turning process and were aligned perpendicular to the implant's turning axis. The measurements obtained with the profilometer for the M surface were quantified and are presented in *Figure 8*.

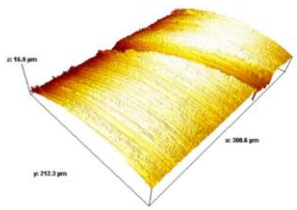

Roughness parameters determined by optical profilometry

	Machined surface (M)
S_a (µm)	0.73 ± 0.01
S_q (µm)	0.94 ± 0.02

Figure 8. Three-dimensional view of the surface microscale roughness of the cylindrical part of a machined titanium implant (M) recorded and measured with an optical profilometer with quantification measurements (n=3). Sa: arithmetical mean height, Sq: root mean square height.

The nanopatterned implant (MN) was characterized via SEM. At low magnification, SEM revealed microtopographical ridges and grooves superimposed with semispherical nanopatterns, which uniformly covered the implant's surface, with an average size of 79 ± 6 nm. The SEM images and measurements are presented in *Figure 9*.

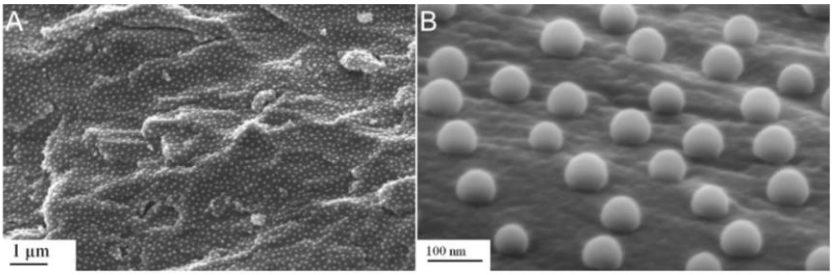

C

Nanoscale topography parameters determined by SEM	
Diameter of the nanohemispheres, nm	79 ± 6
Density of the nanohemispheres, μm^{-2}	31 ± 2
Mean distance (centre to center) between the nanohemispheres, nm	165 ± 28
Surface coverage by the nanohemispheres, %	16 ± 2
Surface area induced by the nanohemispheres, %	34 ± 4

Figure 9. SEM micrographs showing the nanopatterns superimposed over the underlying microrough surface (A), the nanopatterns at a higher magnification (B) and the quantification measurements (n=3) (C) (reprinted after permission from the International Journal of Nanomedicine).

The chemical evaluations of both surfaces were performed with energy-dispersive X-ray spectroscopy (EDX) (penetration depth of 1-3 µm) and showed similar chemical compositions between the M and MN implant surfaces. The spectra were dominated by Ti and O signals (90.2% ± 0.1% and 7.5% ± 0.2%, respectively), with trace amounts of impurities after contact with the coating equipment and the ambient air (Al and Si < 0.2% - Al vacuum chamber and glass vial, C 2.1% ± 0.2% - ambient air, respectively) (*Figure 10*).

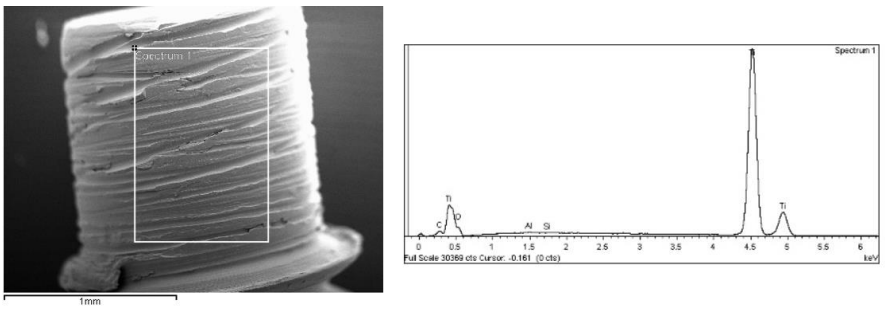

Figure 10. EDX spectra of a representative machined titanium surface showing a dominance of Ti and O signals (n = 2).

4.1.2 EXPERIMENTAL PROCEDURE

The implants were installed pairwise in each rat proximal tibia (control and test surface). After 3, 6 and 28 days of healing, different samples were subjected to various analyses such as gene expression of the implant-adherent cells, histology, immunohistochemistry, and SEM.

4.1.3 GENE EXPRESSION ANALYSIS

Implants were manually unscrewed, and the adherent cells were further processed for quantitative polymerase chain reaction (qPCR) (n=8). The molecular analysis at 3 days revealed significantly lower expression of tumor necrosis alfa (TNF-α) in cells adherent to MN implants than in those adherent to M implants (*Figure 11*). Furthermore, the osteoclastic and bone resorption marker cathepsin K (CatK) differed statistically at 6 days, with a downregulation in cells adherent to the MN implants (*Figure 11*). No major differences could be seen in the expression of osteogenic markers at any of the observation periods.

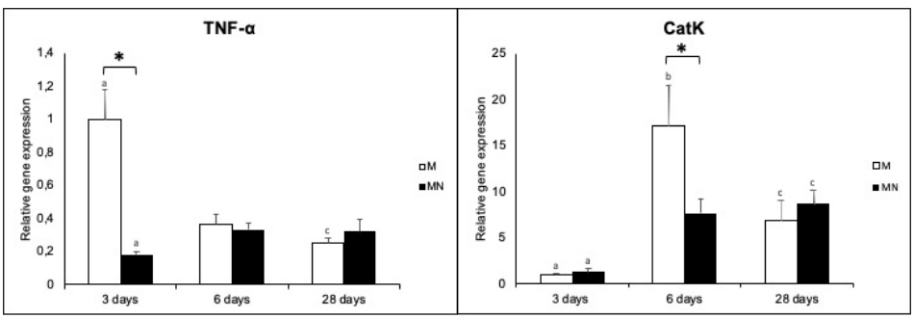

*Figure 11. The column graphs show the gene expression of TNF-α and CatK of implant-adherent cells of M and MN implants. The data are presented as the mean and standard error of the mean (n=8). Statistically significant differences (P<0.05) between the implants at each time point are denoted by * = statistically significant difference between the two implant types at each time point; a=statistically significant difference between 3 and 6 days for each implant type; b=statistically significant difference between 6 and 28 days for each implant type; c=statistically significant difference between 1 and 28 days for each implant type (reprinted after permission from the International Journal of Nanomedicine).*

4.1.4 HISTOLOGY AND IMMUNOHISTOCHEMISTRY

Implants retrieved *en bloc* were further processed for light microscopy evaluation (n=3). Histology and immunohistochemistry revealed, at the cellular level, a higher proportion of CD163-positive macrophages

accumulating in the endosteal and bone marrow compartment across the M surfaces at 3 days of healing than on MN surfaces (*Figure 12*). At 6 days, fewer macrophages could be seen across both implant groups. CD163-positive macrophages were seldom detected after 28 days (*Figure 12*).

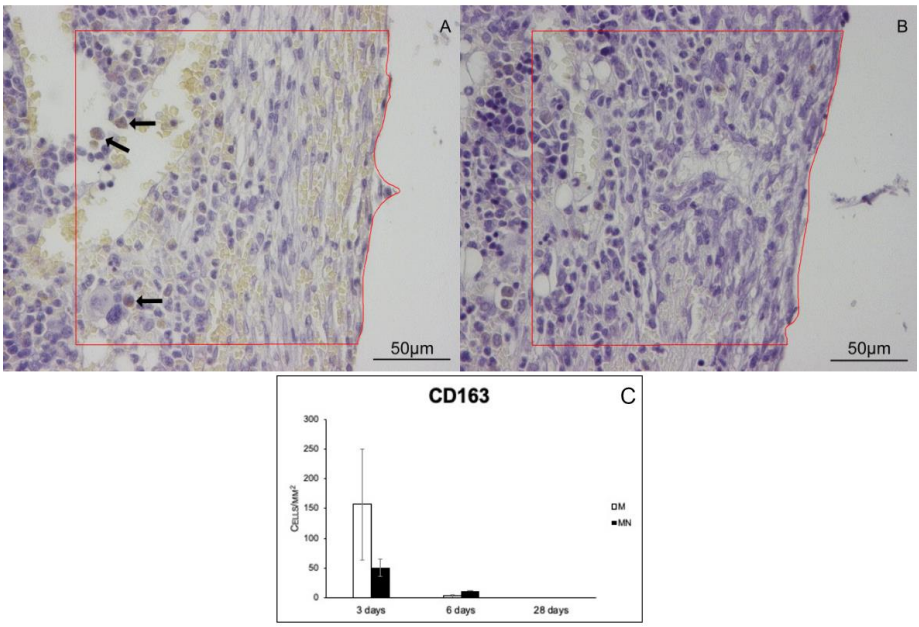

Figure 12. Immunohistochemical analysis of CD163-positive cells. The sections show the positively stained cells at M (A) and MN (B) implants after 3 days of healing. A higher number of CD163-positive cells could be seen at the M than at the MN implants. Positively stained macrophages in the current tissue specimens are indicated by black arrows. The column graph shows the quantification of CD163-positive cells that was performed by counting along the interface and extending 200 µm from the implant surface, expressed as cells/mm^2 (n = 3) (C).

Periostin reactivity, on the other hand, showed a different appearance. At 3 days, periostin was largely confined within positive osteoprogenitor cells and, to a lesser extent, diffuse extracellular staining around these cells. A relatively higher number of periostin-positive cells could be seen across the nanopattened implants. Thereafter, the periostin reactivity appeared mainly as diffuse interstitial staining around and within the newly formed woven bone. At 28 days, a considerable reduction was observed for both implant types, with only a few regions of diffuse staining still detected at the interface (*Figure 13*).

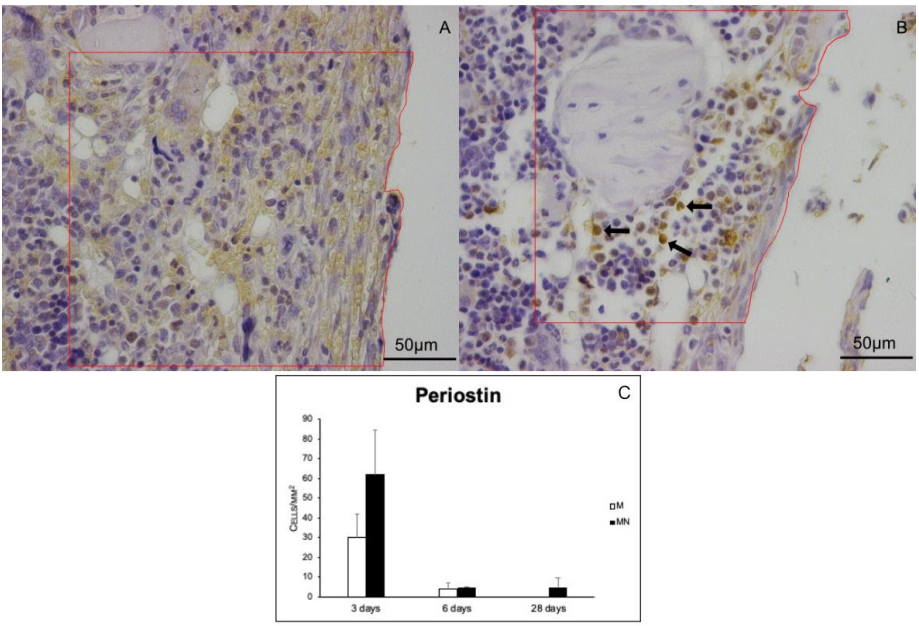

Figure 13. Immunohistochemical analysis of periostin-positive cells and extracellular protein. The sections show the positively stained cells at M (A) and MN (B) implants after 3 days of healing. Positively stained osteoprogenitors in the current tissue specimens are indicated by black arrows. The MN implants showed a higher degree of periostin-stained cells. The column graph shows the quantification of immunostained osteoprogenitors, which was done by counting along the interface and extending 200 μm from the implant surface, expressed as cells/mm² (n= 1-3) (C).

4.1.5 EDX AND SEM ANALYSES

Elemental and morphological analyses on the surface of retrieved implants after 28 days were also performed. These implants were retrieved manually by unscrewing. After 28 days, EDX demonstrated a higher degree of mineralized tissue on the MN implants (*Figure 14*). At that stage, the implant-adherent material had assumed a bone-like appearance at several locations, as defined by SEM (*Figure 14*).

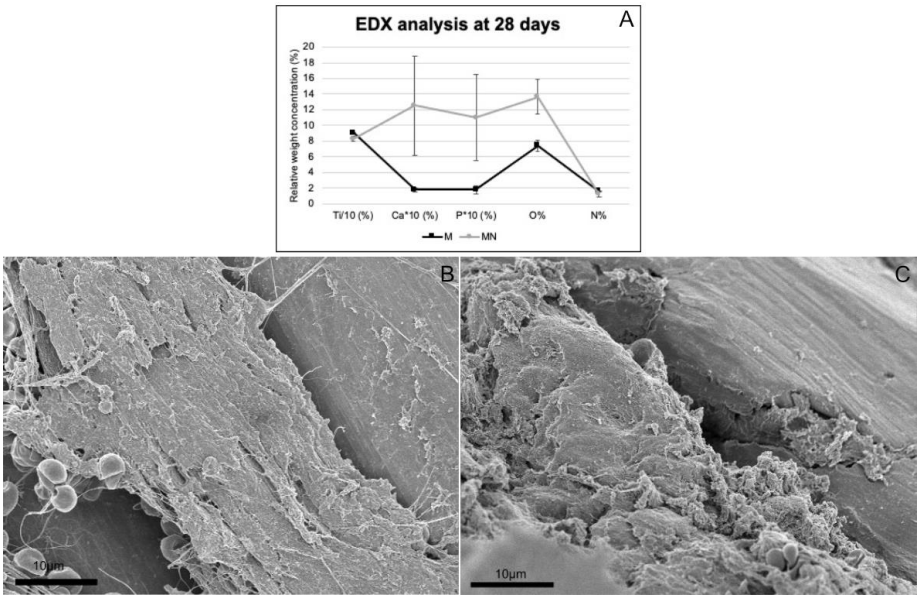

Figure 14. The 2-D line chart shows the relative concentrations of Ti, Ca, P, O and N (n = 2-3) on the surfaces of the retrieved implants after 28 days (A). The SEM micrographs show bone-like tissue formation on both M (B) and MN (C) implants at the same time point (28 days) (reprinted after permission from the International Journal of Nanomedicine).

4.2 PILOT STUDIES

Since colloidal lithography has not been previously used for nanopatterning of complex 3-D surfaces, a series of pilot studies were performed to evaluate the reproducibility of the nanopatterning process and the mechanical stability of the nanopatterns. The switch from cylindrical to screw-shaped implants aimed to simulate commercially available dental implants, on which well-defined nanotopography can be superimposed for the evaluation of the biological response.

The same animal model (rat) was used in the pilot experiments, as well as a similar implantation site (medial aspect of the tibial metaphysis). The surgical procedure, which has been previously described, entails manual insertion and retrieval during the same surgical session. The reproducibility of the nanopatterning process was examined with SEM. Further, four different surfaces were prepared for the following studies (two different microtopographies, machined and polished surfaces, with or without superimposed nanotopography). As the electropolishing process relatively

reduces the diameter of the polished implants, a surgical drill protocol was developed and verified to ensure primary stability upon implant installation.

It was found that increasing the thickness of the Ti coating layer resulted in increased resistance and superior mechanical stability of the nanopatterns. With the acceptance of a titanium layer with a minimum thickness of 10 nm for the cylindrical implants, a 30 nm layer appeared to be superior for screw-shaped implants. Furthermore, heat treatment was applied, and when the implants were subjected to a heat of 500 ºC for 5 hours, the shape of the nanopatterns remained intact. Temperatures above 500 ºC led to decomposition of the nanopatterns. Heat treatment as described above contributed further to the mechanical stability of the nanopatterns, with intact nanopatterns after retrieval from the rat tibia in the range of 95-100%, as evaluated by SEM.

4.3 PAPER II

4.3.1 IMPLANTS AND SURFACE CHARACTERIZATIONS

In this study, four different implants were used. Polished (P), polished with nanopatterns (PN), machined (M) and machined with nanopatterns (MN). The macroscopic geometry and surface chemistry were similar for all implants.

The surface topographies of the screw-shaped implants were characterized by optical profilometry. For the polished surfaces, the microtopography (microgrooves and ridges) of the machined implants was removed by the electropolishing process. The surface parameters of the microtopography of these two implants are summarized in *Figure 15*.

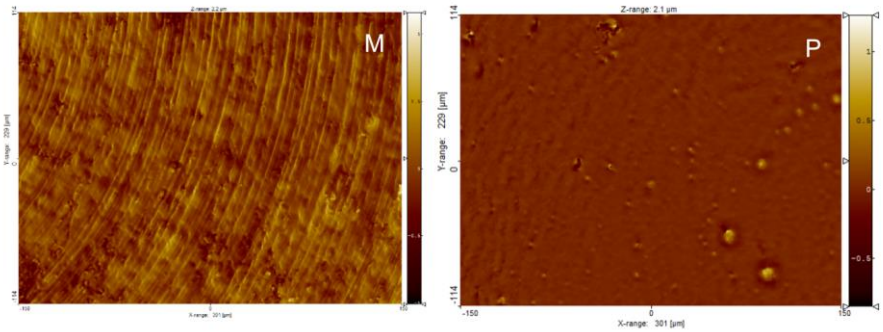

Roughness parameters determined by optical profilometry		
	Machined surface (M)	Polished surface (P)
S_a (nm)	141 ± 8	33 ± 7
S_q (nm)	181 ± 11	56 ± 7

Figure 15. Interferometry of machined (M) and polished (P) implants with quantification of the surface parameters (n = 2).

Since the profiler has a limited lateral resolution of 1 µm, the nanotopography was evaluated by atomic force microscopy (AFM) and SEM. In particular, AFM was performed on Ti-coated silicon wafers before and after annealing to determine if the heat treatment could additionally affect the surface nanoscale roughness. It was found that heat treatment could increase the surface nanoroughness, and this was dependent on sputtered titanium coating, annealing temperature, and ramping. Nevertheless, a heat-induced change in the nanoroughness could be kept at Sq 1.4 nm after optimization of these processes, which is below the height of the nanopatterns (*Table 6*).

Table 6. Atomic force microscopy measurements to determine the effect of the annealing treatment on the surface nanoroughness.

Roughness parameters determined by atomic force microscopy (AFM)		
	Ti-coated silicon wafer	Ti-coated silicon wafer after annealing at 500ºC for 5 hours
S_a (nm)	0.5	1.1
S_q (nm)	0.7	1.4

Finally, SEM was used to characterize the nanopatterns by image analysis and surface modeling. All nanopatterned implant surfaces revealed a uniformly covered surface with semispherical nanopatterns with the same average diameter of 75 ± 8 nm. The measurements obtained with SEM were quantified and are presented in the table of *Figure 16*.

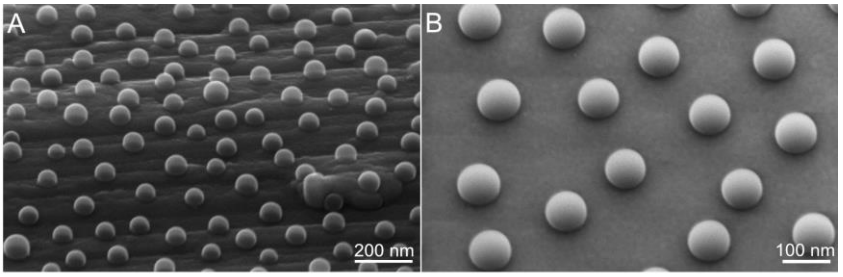

C

Nanoscale topography parameters determined by SEM	
Diameter of the nanohemispheres, nm	75 ± 8
Density of the nanohemispheres, μm^{-2}	50 ± 3
Mean distance (centre to center) between the nanohemispheres, nm	150 ± 22
Surface coverage by the nanohemispheres, %	18 ± 4
Surface area induced by the nanohemispheres, %	50 ± 11

Figure 16. SEM micrographs showing the machined implant with superimposed nanopatterns (MN) (A), the polished implant with superimposed nanopatterns (PN) (B) and the quantification measurements (n=3) (C).

The chemical characterization of the implant surfaces was performed with X-ray photoelectron spectroscopy (XPS). The method is highly sensitive and reveals the chemical composition in atomic % for the outermost 2-10 nm of the surface. XPS provided quantitative data on both the elemental composition and the different chemical states of an element. According to the analysis, titanium oxide and carbon (approximately 46% O, 20% Ti and 31% C, respectively) dominated all the implant surfaces. High-resolution carbon spectra showed unoxidized carbon (75-80% of the total carbon peak), such as hydrocarbon chains/aromatic groups, which are typical surface contaminants due to ambient air exposure. Even other minor contaminants were identical for all surfaces (*Figure 17*).

A

Sample	*Atomic %*								
	C	O	Ti	Cu	Pb	N	Ca	Si	P
M	30.8	46.8	19.7	1.3	0.03	0.6	-	0.7	-
MN	30.8	47.3	19.5	0.9	0.01	0.7	0.07	0.7	-
P	36.4	43.6	16.4	0.9	-	1.8	0.1	0.6	0.1
PN	30.9	47.1	20.0	0.7	-	0.6	0.04	0.6	-

B

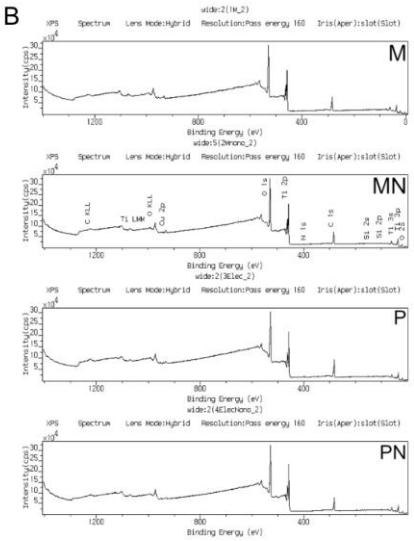

Figure 17. XPS-determined elemental composition (A) and spectra of the four different titanium implant surfaces (B) (n = 1) (figure reprinted with permission from Acta Biomaterialia).

Further verification that the carbon compounds did not originate from polystyrene (PS) was obtained by time-of-flight secondary ion mass spectroscopy (TOF-SIMS). Although polystyrene signals were evident on the flat nanopatterned surface after fabrication, they disappeared after heat treatment, showing a similar chemical composition to the flat heat-treated control surface (*Table 7*).

Table 7. TOF-SIMS analysis of polystyrene exposure on the following implant surfaces: flat Ti film (Flat), polystyrene nanoparticles coated with Ti film (Nano) and the same surfaces after annealing at 500ºC (Flat heat and Nano heat, respectively). The values of Ti, TiOx and PS represent the sum of the area-normalized ion intensity x 10^5 (n = 1) (reprinted with permission from Acta Biomaterialia).

Positive ion species:

	Flat	*Nano*	*Flat heat*	*Nano heat*
Ti	*4832.99*	*5806.89*	*5584.80*	*6135.44*
TiOx	*11226.61*	*12956.15*	*14919.41*	*16131.83*
Ti/TiOx	*0.43*	*0.45*	*0.37*	*0.38*
PS	*1359.13*	*3123.49*	*1275.06*	*1792.05*
PS/(Ti+TiO)	*0.08*	*0.17*	*0.06*	*0.08*

Negative ion species:

	Flat	*Nano*	*Flat heat*	*Nano heat*
TiOx	5994.37	3589.80	8876.40	8607.73
PS	742.82	1074.38	667.31	925.04
PS/TiOx	0.12	0.30	0.08	0.11

4.3.2 EXPERIMENTAL PROCEDURE

The four implant types (P, PN, M and MN) were installed in the tibiae of each rat, with two implants on each side, and followed a predetermined schedule ensuring alternate placement in the proximal and distal tibial bone of the different implants. After 12 hours, 1 day and 3 days of healing, they were retrieved for various analyses.

4.3.3 GENE EXPRESSION ANALYSIS

Implants retrieved manually by unscrewing were processed for gene expression analysis of the implant-adherent cells. qPCR was employed and revealed significantly lower expression of monocyte chemoattractant protein-1 (MCP-1) in the cells adherent to MN and PN implants than in the P implants at 1 day. The temporal expression of MCP-1 revealed a peak at 1 day that was decreased at 3 days for all implants. The expression of the integrin-β1 chain was higher on PN implants than on M and MN implants at 1 day, with increasing temporal expression after 3 days for all implants. Similarly, the temporal expression of the bone formation gene osteocalcin (OC) increased after 1 day and retained peak values at 3 days. At 3 days, significantly higher OC expression was demonstrated for MN and PN implants than for M implants. The osteoclastic gene CatK revealed a steady temporal increase during the evaluation time points, reaching peak expression at 3 days for all

implant types. At 1 day, however, CatK expression was higher in cells adherent to the P implants than in those adherent to the M implants (*Figure 18*).

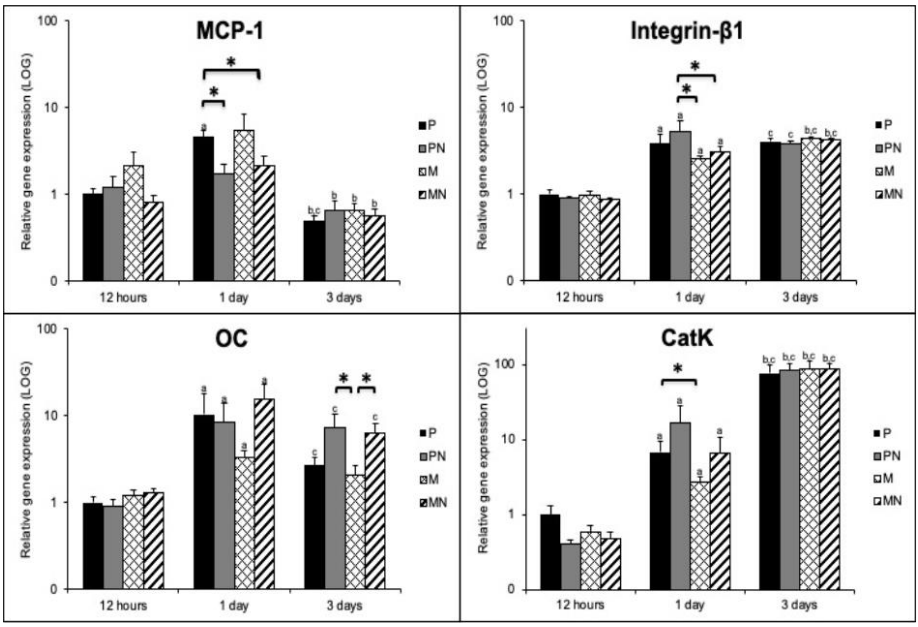

*Figure 18. Column graphs showing the gene expression of MCP-1, Integrin-β1, OC and Catk in implant-adherent cells from polished (P), polished nanopatterned (PN), machined (M) and machined nanopatterned (MN) implants. The data show the mean and standard error of the mean (n = 10). Statistically significant differences ($p < 0.05$) are indicated by asterisks or lowercase letters: *= statistically significant difference between the two implant types at each time point; a=statistically significant difference between 12 hours and 1 day for each implant type; b=statistically significant difference between 1 and 3 days for each implant type; c=statistically significant difference between 12 hours and 3 days for each implant type (the column graphs are reprinted with permission from Acta Biomaterialia).*

4.3.4 HISTOLOGY AND IMMUNOHISTOCHEMISTRY

Microscopic evaluation of new bone formation on sections stained with hematoxylin and eosin (H&E) was performed quantitatively at 3 days. At that time point, new bone formation could be seen either *de novo*, on the marrow part of the implant, or in conjunction with the endosteal bone or bone fragments that had been displaced in the marrow compartment during the preparation procedure. The analysis showed a higher percentage of osteoid and woven bone in the threads of the PN and MN implants when compared to P and M, respectively (*Figure 19*).

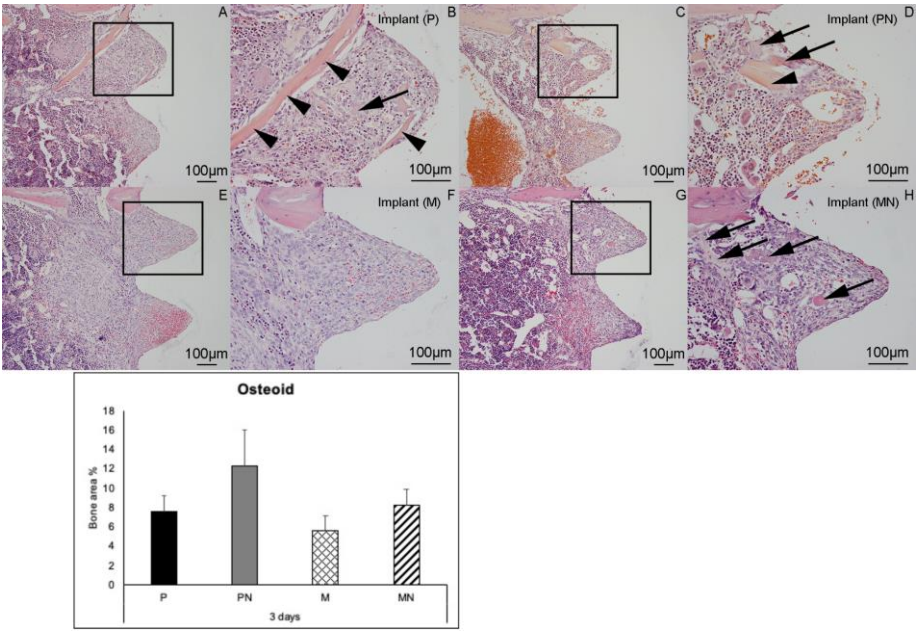

Figure 19. Histological analysis of the tissues around the implants. The survey light micrographs of paraffin-embedded and H&E stained sections show the morphology of the tissue around polished (P) (A, B), polished nanopatterned (PN) (C, D), machined (M) (E, F) and machined nanopatterned (MN) (G, H) implants 3 days after implantation. The evaluations of the sections were performed with a light microscope at magnifications of 4x (not shown here), 10x (A, C, E and G) and 20x (B, D, F and H). After 3 days, well-organized granulation tissue was formed within the threads and the peri-implant area. Sites with minor hematomas can still be observed. Signs of early bone formation were detected, as indicated by the appearance of osteoblastic seams (black arrows). Cortical bone displaced inferiorly through the direction of the preparation is occasionally seen (black arrowheads). The column graph shows the relative proportion of newly formed bone in the tissue threads of the polished (P), polished nanopatterned (PN), machined (M) and machined nanopatterned (MN) titanium implants (I). The data show the mean and standard error of the mean (n = 3).

The higher proportion of new bone formation in relation to PN and MN agreed with the periostin staining assessment. The immunohistochemical analysis showed that the nanopatterned implants, MN and PN, showed a higher degree of periostin staining in contrast to M and P. The periostin staining appeared to be diffusely spreading in the extracellular matrix, indicating active intramembranous bone formation (*Figure 20*).

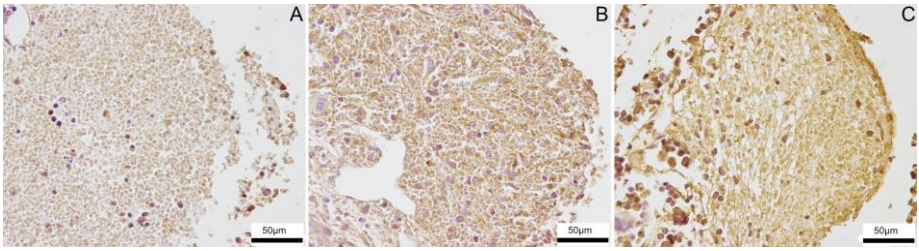

Figure 20. Immunohistochemical analysis of periostin-positive cells and extracellular protein. The analysis was performed after 12 hours (A), 1 day (B) and 3 days (C). The present figure shows tissue between the threads of a PN implant at the abovementioned time points and is used here to demonstrate the overall periostin allocation over time, even confirmed histologically on the other implant types. Periostin mainly accumulated intracellularly at 12 hours and 1 day, while after 3 days of healing, it was diffusely spread extracellularly as a sign of intramembranous bone formation.

A combined qualitative and quantitative evaluation of CD68-positive monocytes/macrophages was also performed. This analysis showed a temporal increase with a peak monocyte/macrophage number at the M and MN implants at 1 day, while the peak was delayed for 3 days for the P and PN implants. The MN implants showed a lower number of CD68-positive cells than the M implants, particularly after 1 and 3 days, while this was evident for PN versus P implants only after 3 days of healing (*Figure 21*).

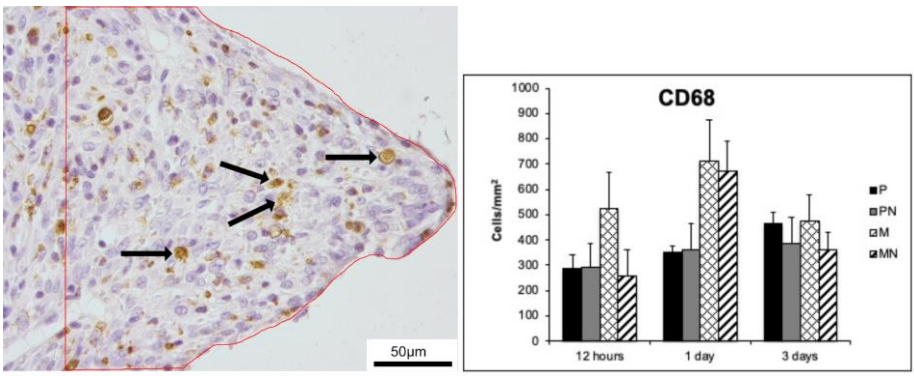

Figure 21. Immunohistochemical analysis of CD68-positive monocytes/macrophages. The analysis was performed under light microscopy using a high-power field (magnification x40) on well-preserved tissue in between threads representing all the implants and studying time points. Positively immunostained monocytes/macrophages in the current tissue specimen are indicated by black arrows, and the section represents the healing response towards a machined (M) implant after 3 days. The relative number of monocytes/macrophages counted towards the polished (P), polished

nanopatterned (PN), machined (M) and machined nanopatterned (MN), expressed as cells/mm^2, is shown in the column graph. The data show the mean and standard error of the mean (n = 1-3) (the column graph is reprinted with permission from Acta Biomaterialia).

4.3.5 **SEM**

SEM evaluation indicated greater spreading of cells on the surface of the nanopatterned implants, where the cells suggested adhesion via direct physical interaction through cell filopodia sensing of the nanopatterns (*Figure 22*).

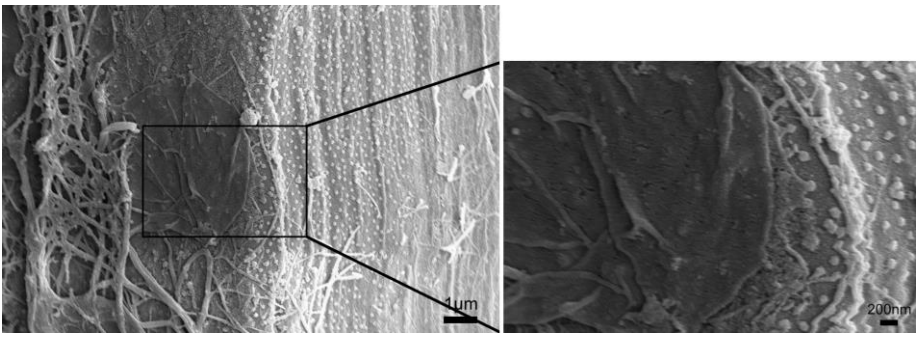

Figure 22. Scanning electron analysis of retrieved implants. The SEM micrograph shows the surface of a machined nanopatterned (MN) implant retrieved after 3 days of healing. A cell, partly covered with a fibrinous material, is spread over the surface and interacts with the nanopatterns through filopodia.

4.4 PAPER III

In this study, four different implant surfaces were used, as in study II: polished (P), polished nanopatterned (PN), machined (M) and machined nanopatterned (MN). Since these implants belonged to the same fabrication batch as the implants used in Paper II, the same characterization of the surface topography and chemistry described above applies. The implants were placed in the rat tibial bone and removed after 6, 21 and 28 days, and their biomechanical anchorages were evaluated and processed further for molecular and morphological analyses.

4.4.1 REMOVAL TORQUE

After 6 days of healing, the MN implants showed significantly higher removal torque values than the P, PN and M implants. Similarly, at 21 days, higher torque values were recorded for the MN implants, with statistically significant differences in comparison to P and PN implants. At 28 days, both the M and MN implants showed higher torque values than the P and PN implants; however, the only significant difference was found between the M and PN implants. In general, the torque values of all implants, except PN, increased until 21 days, reaching a plateau at 28 days. In contrast, a modest increase in torque was recorded for PN during the evaluation period, where the highest values were recorded at 28 days (n=10) (*Figure 23*A). When the data from the three time points were pooled according to the implant surfaces (n=30), the MN implants showed significantly higher values than the P and PN implants (*Figure 23*B).

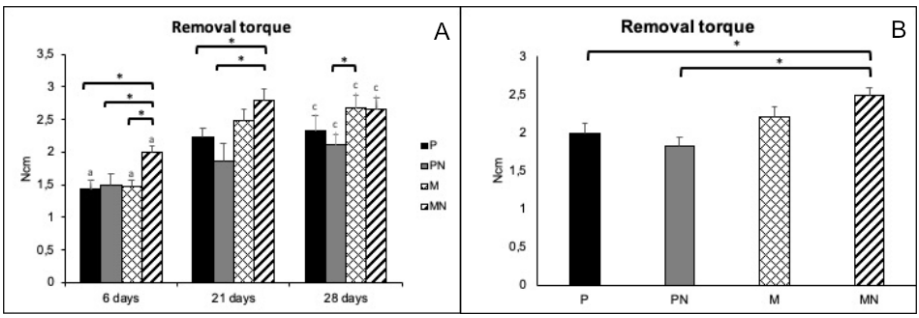

Figure 23. Column graph showing the removal torque measured at the interface between recipient bone and polished (P), polished nanopatterned (PN), machined (M) and machined nanopatterned (MN) after 6, 21 and 28 days of healing. The mean and the standard error of the mean are illustrated, and significant differences ($p < 0.05$) are indicated by asterisks between the implants at the same time point and lowercase letters for significant differences between the time points: (a) between 6-21 days, (b) between 21 and 28 days and (c) between 6 and 28 days (A). Column graph showing the removal torque of the implant surfaces after the time points have been merged into one. The mean and the standard error of the mean are illustrated, and significant differences ($p < 0.05$) are indicated by asterisks (B).

4.4.2 HISTOMORPHOMETRY

The histomorphometric measurements revealed a significantly higher percentage of bone-to-implant contact (BIC) at MN implants after 6 days than the P implants. A temporal increase in BIC was observed for all implants from 6 to 21 days. This trend continued after 28 days for the P implants, which showed a progressive increase in BIC. At 28 days, a statistically higher BIC%

was found at P versus PN implants. Further, at this time point, MN implants demonstrated statistically higher values than PN implants (*Figure 24*A). When the BIC data from the three time points were pooled, the BIC% of MN implants was higher than that of the other implants, reaching a statistically significant difference when compared to P implants (*Figure 24*B).

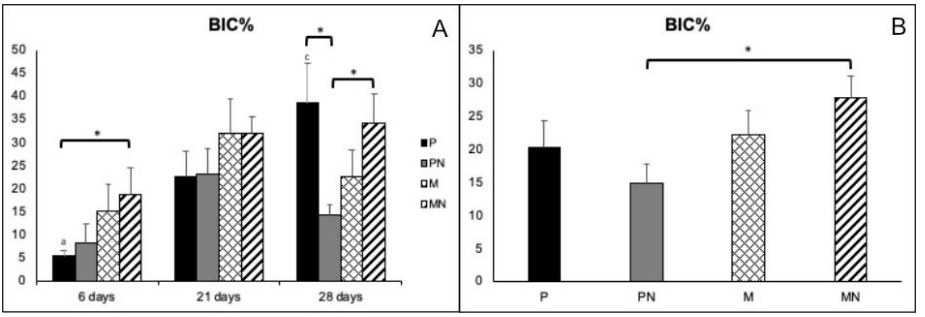

Figure 24. Column graph showing the bone-implant contact (BIC %) measured for polished (P), polished nanopatterned (PN), machined (M) and machined nanopatterned (MN) implants after 6, 21 and 28 days of healing. The mean and the standard error of the mean are illustrated, and significant differences ($p < 0.05$) are indicated by asterisks between the implants at the same time point and lowercase letters for significant differences between the time points: (a) between 6-21 days, (b) between 21 and 28 days and (c) between 6 and 28 days (A). Column graph showing the bone-implant contact (BIC%) after the time points have been merged into one. The mean and the standard error of the mean are illustrated, and significant differences ($p < 0.05$) are indicated by asterisks (B).

The bone area percentage (BA%) formed within the threads showed a gradual temporal increase for all implants until 21 days and leveled out at 28 days. The P implants showed a statistically significant increase at 21 days compared to MN implants (*Figure 25*A). When the BA values measured at different time points were pooled for each implant surface, no differences could be found (*Figure 25*B).

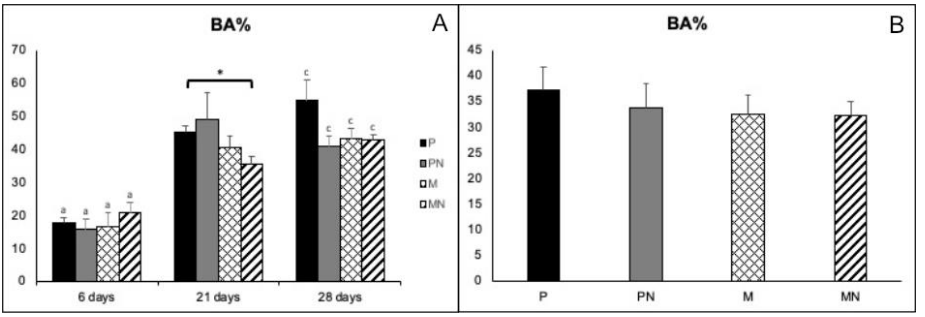

Figure 25. Column graph showing the bone area (BA%) relative to the total bone area measured at polished (P), polished nanopatterned (PN), machined (M) and machined nanopatterned (MN) implants after 6, 21 and 28 days of healing. The mean and the standard error of the mean are illustrated, and significant differences ($p < 0.05$) are indicated by asterisks between the implants at the same time point and lowercase letters for significant differences between the time points: (a) between 6-21 days, (b) between 21 and 28 days and (c) between 6 and 28 days (A). Column graph showing the bone-implant contact (BIC%) after the time points have been merged into one. The mean and the standard error of the mean are illustrated (B).

4.4.3 GENE EXPRESSION ANALYSIS

At the molecular level, qPCR was used to investigate the gene expression patterns of cells adherent to the different implant surfaces. The expression of the proinflammatory cytokine TNF-α was downregulated at 6 and 21 days at MN implants compared to their corresponding control M implants. This difference was statistically significant at 21 days. The temporal expression of TNF-α showed an increase from 6 days to 21 days and decreased thereafter. The expression of TNF-α in cells adherent to P implants at 28 days was significantly higher than that in the PN implants (*Figure 26*).

The expression of receptor activator of nuclear factor kappa B ligand (RANKL) in cells adherent to MN implants at 6 days was significantly lower than that in cells adherent to PN and M implants. At this time point (6 days), the highest RANKL expression was found at the M implant. The expression of RANKL remained lower in cells adherent to MN at 21 days, but the differences were not statistically significant. At 28 days, the expression levels were slightly increased at all implants (*Figure 26*).

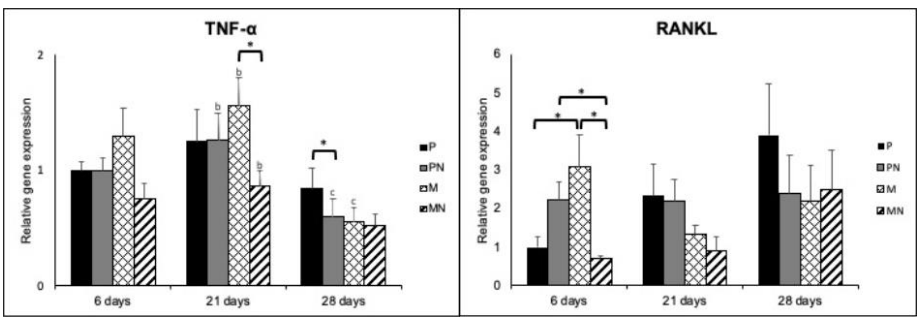

*Figure 26. Column graphs showing the gene expression of TNF-α and RANKL in implant-adherent cells of polished (P), polished nanopatterned (PN), machined (M) and machined nanopatterned (MN) implants. The data show the mean and standard error of the mean (n = 10). Statistically significant differences ($p < 0.05$) are indicated by asterisks or lowercase letters: *= statistically significant*

difference between the two implant types at each time point; a=statistically significant difference between 6 and 21 days for each implant type; b=statistically significant difference between 21 and 28 days for each implant type; c=statistically significant difference between 6 and 28 days for each implant type.

When the qPCR data regarding the expression of TNF-α were pooled, lower expression levels could be seen for MN implants than for the remaining implant surfaces. Statistically lower expression was observed for MN implants versus the P implants (*Figure 27*). Furthermore, when the data for the expression of RANKL were pooled, the MN implants showed significantly lower expression values than all other implant surfaces (*Figure 27*).

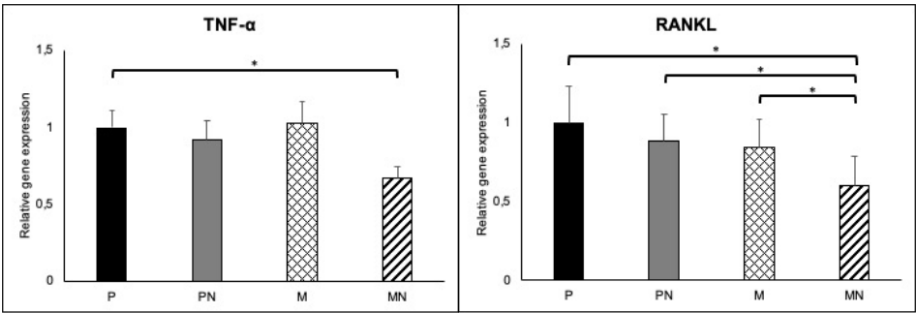

Figure 27. Column graphs showing the gene expression of TNF-α and RANKL in implant-adherent cells of polished (P), polished nanopatterned (PN), machined (M) and machined nanopatterned (MN) implants after pooling the time points. The data show the mean and standard error of the mean (n = 30). Statistically significant differences (p < 0.05) are indicated by asterisks.

Correlation analysis of the pooled data was utilized to evaluate the effect of the surface variables *per se* (nano- and microtopography) and the interaction between them regarding the dependent variables (removal torque, histomorphometry and gene expression).

The analysis showed that the machined topography (microtopography) had a significant effect on removal torque, BIC and the TNF-α expression. On the other hand, nanotopography *per se* statistically affected the expression of TNF-α. The combination of nano- and machined topographies (nanotopography superimposed on machined topography) had a profound effect on the removal torque and the expression of TNF-α (*Table 8*).

Table 8. Table showing the main effects of each surface topography per se and their interaction effects when considering the dependent variables RTQ and BIC, and the molecular expression of TNF-α and RANKL. The significant differences (p values < 0.05) are denoted with asterisks.

Factors	**Nanotopography**	**Microtopography (machined topography)**	**Combined topography (current nanotopography superimposed on the machined topography)**
	p-value	*p-value*	*p-value*
RTQ	0.2	0.004*	0.015*
BIC	0.7	0.045*	0.14
TNF-α	0.005*	0.007*	0.002*
RANKL	0.2	0.3	0.35

4.5 PAPER IV

4.5.1 IMPLANTS AND SURFACE CHARACTERIZATION

In this human study, two different implant surfaces were selected and used: machined (M) and machined nanopatterned (MN). The surface topography was characterized with optical profilometry and SEM. The measurements were quantified and are presented in the *Table 9*.

A

Roughness parameters determined by optical profilometry		
	Machined surface (M)	Machined nanopatterned surface (MN)
S_a (μm)	0.296 ± 0.019	0.261 ± 0.032
S_q (μm)	0.374 ± 0.02	0.325 ± 0.037

B

Nanoscale topography parameters determined by SEM	
Diameter of the nanohemispheres, nm	51 ± 9
Density of the nanohemispheres, μm^{-2}	40 ± 5
Mean distance (centre to center) between the nano hemispheres, nm	130 ± 11
Surface coverage by the nanohemispheres, %	8 ± 3
Surface area induced by the nanohemispheres, %	9 ± 3

Table 9. Interferometry quantification measurements of machined (M) and machined nanopatterned (MN) implants (n = 4) (A) and SEM quantification measurements (n=4) (B).

The chemical characterization of the surfaces was performed with EDX and TOF-SIMS. EDX showed similar chemical compositions between the M and MN implant surfaces, with spectra dominated by Ti and O signals (55,3% ± 2% and 40,45% ± 1,95%, respectively). Furthermore, TOF-SIMS showed a similar chemical composition without contamination of the MN surfaces with PS carbon compounds.

4.5.2 SURGICAL PROCEDURE

The implants were installed in the posterior maxilla pairwise at the same time that the clinical implants were installed, with alternate proximal and distal placement ensuring rotation between the implant types.

4.5.3 GENE EXPRESSION ANALYSIS

The test implants were retrieved by unscrewing after 6-8 weeks of healing at the same surgical session as the clinical implants received their healing abutments. The implant-adherent cells were subjected to molecular analysis using qPCR. No significant differences could be seen when comparing the expression of the cytokines TNF-α, interleukin (IL)-6, MCP-1 and IL-10 between the two implant surfaces. In contrast, the expression of bone formation markers was higher in cells adherent to the MN in comparison to M implants. Statistically significant differences were demonstrated for the higher expression of runt-related transcription factor 2 (RUNX-2), alkaline phosphatase (ALP) and OC at the MN implants. The expression of bone morphogenetic protein (BMP)-2 was also higher at MN implants but did not reach statistical significance (*Figure 28*). Finally, when evaluating the expression of the osteoclastic and remodeling markers calcitonin receptor (CTR), CatK, receptor activator of nuclear factor kappa B receptor (RANK), RANKL and osteoprotegerin (OPG), no significant differences could be observed.

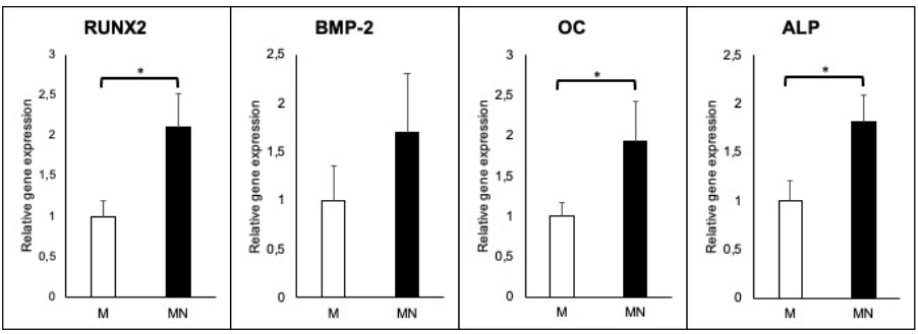

Figure 28. Column graphs showing the gene expression of genes denoting osteoblastic differentiation, RUNX2 and BMP-2, and osteogenic activity, OC and ALP, in adherent cells of machined (M) and machined nanopatterned (MN) implants. The data show the mean and standard error of the mean (n = 10). Statistically significant differences (p < 0.05) are indicated by asterisks.

Furthermore, the correlation analysis suggested that older age was positively associated with expression of the pro-inflammatory cytokines TNF-α and

MCP-1 at the M implant, while an increased expression of the anti-inflammatotory cytokine IL-10 was associated with the MN implant. Additionally, a negative association with expression of pro-osteogenic growth factor BMP-2 at the MN implant was seen (*Table 10*). The female gender was associated with an increased expression of osteogenic commitment gene, RUNX2, and a decreased expression of the osteoclastic gene RANK at the M implant. In contrast, the MN implants were positively associated with MCP-1 and OPG at the female gender. Hypertension and pharmacological substitution with angiotensin receptor blocker (ARB) increased the expression of MCP-1 at M implants, while hypercholesterolemia and substitution with statins were negative correlated with IL-6 at MN implants.

Table 10. Correlation analysis showing negative and positive associations between patient demographic data and gene expression in cells adherent to machined (M) and machined nanopatterned (MN) implants (n = 10).

	M		**MN**	
	Negative correlations - *r (P-value)*	**Positive correlations - *r (P-value)***	**Negative correlations - *r (P-value)***	**Positive correlations - *r (P-value)***
Older the age	-	TNF-α - 0.7 (0.02) MCP-1 - 0.8 (0.001)	BMP-2 - -0.7 (0.03)	IL-10 - 0.7 (0.3)
Female gender	RANK - -0.7 (0.02)	RUNX2 - 0.8 (0.002)	-	MCP-1 - 0.7 (0.02) OPG - 0.8 (0.008)
Hypertension	-	MCP-1 - 0.7 (0.02)	-	-
Angiotensin receptor blocker	-	MCP-1 - 0.7 (0.02)	-	-
Hypercholesterolemia	-	-	IL-6 - -0.7 (0.02)	-
Several illnesses	-	-	IL-6 - -0.7 (0.03)	-
Statin medication	-	-	IL-6 - -0.7 (0.02)	-
Several medications	-	-	IL-6 - -0.7 (0.03)	-

5 DISCUSSION

In the current thesis, the role of well-characterized, intentionally created topographic nanopatterns has been studied in an attempt to elucidate the cellular and molecular events taking place at the bone implant interface and how these cellular and molecular events correlate with histological and biomechanical analyses. Modulatory effects induced by the nanotopography on inflammatory responses and on osteoblastic and osteoclastic activities were evaluated. Determination of the effects of nanotopography *per se* was achieved since all other implant surface parameters, such as microroughness and chemistry, were unified between the test and control implants, with the only variable being the nanotopography.

5.1 IMPLANT DESIGN AND NANOPATTERN FABRICATION

The nanotopography was produced by colloidal lithography. Before applying this fabrication method on screw-shaped Ti implants for *in vivo* testing, it was evaluated by our group both *in vitro* and *in vivo*. In brief, an *in vitro* study using semispherical nanopatterns with diameters of 238, 130 and 88 nm showed an increased proliferation of hMSCs, similar to osteoblastic differentiation and osteogenic activity, in favor of substrates with 238-nm protrusions [152]. The *in vivo* study used specially designed implants [137]. These titanium implants had threads only at the coronal top, intended to ensure implant stability, while the apical part, which was narrower and was positioned after installation in the marrow compartment, was cylindrical. Only this portion without threads of the implant was nanopatterned. The advantage of this setup enabled the analysis of the nanotopography on a smooth portion of the implant. Furthermore, the idea of this implant design was to avoid detachment of the assembled nanopattern during installation of the implant through the cortical bone. The results showed a higher BIC for 60-nm protrusions than for 120- and 220-nm protrusions. However, it was not suitable for functional osseointegration tests after longer healing times, e.g., removal torque measurements, due to the low mechanical strength of induced nanopatterns. In the next stage, the stability of the nanopatterns was improved by increasing the coating thickness and thermal annealing at 500 °C for 5 hours, which provided the possibility to apply and stabilize the nanopattern on entirely three-dimensional, screw-shaped implants resembling commercially available endosseous dental implants.

Both the early and early to mid-late effects of titanium nanotopography in the implant-tissue interface were studied in a rat tibia model. In these two studies (Papers II and III), machined and polished implants with and without nanopatterns were used. Thus, implants with smooth surfaces (machined) and very smooth surfaces (polished) at the microscale were combined with nanotopography. However, a limitation of these studies originates from the fabrication method of the electropolished implants, which resulted in implants with a 12% reduction in the macroscopic dimensions with a concomitant reduction in surface area.

Finally, in the human study (Paper IV), the healing process in the posterior maxillary bone was evaluated by means of molecular tools. Due to practical and ethical issues, hard biomechanical and histological data were omitted, which is an apparent limitation of this study.

5.2 CELL RECRUITMENT, INFLAMMATORY RESPONSES AND ADHESION

At the early healing time points (12 hours – 3 days) evaluated in Paper II, lower expression levels of the MCP-1 were found for the PN and MN implants at 1 day. Even though not statistically significant, the same trend could be seen for TNF-α, with a 4.5-fold lower expression in cells adherent to MN implants at 1 day. This trend was even consistent with the expression of IL-1β at 1 day, with 1.8- and 1.5-fold lower expression being observed for the MN and PN implants, respectively. In Paper I, the expression of the proinflammatory cytokine TNF-α was significantly downregulated at 3 days in cells adherent to MN implants. These findings are in line with previous studies in the same animal model that evaluated the healing of moderately roughened Ti implants in the tibia [22, 24]. In these studies, it was shown that MCP-1 is involved in the recruitment of monocytes/macrophages [24], while microroughened oxidized implants downregulated the expression of TNF-α and IL-1β from 3 hours until up to 6 days after implantation [22, 24]. This is also in agreement with human studies showing downregulation of the expression of TNF-α in the jaw bone 24 hours after implantation of oxidized implants compared to machined implants [23]. Thus, it seems that nanopatterned implants, in addition to downregulating the expression of the proinflammatory cytokines TNF-α and IL-1β, also downregulate the expression of the chemoattractant cytokine MCP-1, unlike oxidized implants.

The immunohistochemical analysis in Paper II corroborated the gene expression data, revealing fewer CD68-positive macrophages at the MN

implants at 12 hours and 1 day and at both MN and PM implants at 3 days. In Paper I, immunohistochemistry also revealed fewer CD163-positive stained macrophages at the MN implants after 3 days of healing.

The results are also in agreement with *in vitro* studies that evaluated the inflammatory response. A decrease in macrophage adhesion was observed *in vitro* after 4, 12 and 24 hours of human monocyte culture on titanium substrates with 40-nm nanopits compared to substrates with submicron roughness (features with a diameter > 100 nm and height of 30 nm) or flat surfaces [140]. Compared to nanotubes with an 80-nm diameter or polished surfaces, titanium nanotubes with a diameter of 30 nm also decreased the adhesion and proliferation of mouse-derived macrophages after 4, 24 and 48 hours of culture [144]. In contrast, another *in vitro* study showed that compared to substrates with 30- to 40-nm nanotubes, titanium nanotubes with diameters of 70-80 nm impeded murine-derived macrophage adhesion and proliferation after 1, 2 and 3 days [145]. Despite these contradictory results, both studies described an attenuated inflammatory response. In the first study [144] the secretion of the chemokine MIP-α and the proinflammatory cytokine TNF-α was decreased after 24 and 48 hours, while the expression of the chemokine MCP-1 was also downregulated after 48 hours across substrates with 80-nm nanotubes. In another study [145], substrates with 70- to 80-nm nanotubes decreased the inflammatory response by lowering the expression levels of TNF-α and IL-1β after 12 hours, as evaluated by qPCR. These molecular findings are further in line with one of the pioneering *in vitro* experiments showing that compared to flat surfaces of the same material, titanium nanotubes with a diameter of 79 nm significantly reduced inflammation [180].

In the present work, the lower expression levels of TNF-α, IL-1β and MCP-1 proinflammatory cytokines coincided with fewer CD68-positive macrophages in the peri-implant tissue (Paper II). This surface marker is found on macrophages of both phenotypes, i.e., M1 and M2 macrophages. Taken together, these findings suggest that reduced production of proinflammatory cytokines would result in fewer proinflammatory M1 macrophages and therefore a lower M1/M2 ratio at the nanopatterned implants. This assumption is in line with an *in vivo* study performed on mouse femurs in which the M1/M2 ratio was lower at titanium cylindrical implants with nanotubes with a diameter of 30 nm than at polished implants and nanotubes with a diameter of 100 nm [133]. However, fewer CD163-positive macrophages, i.e., M2 macrophages, were found to be associated with 79-nm nanopatterns in Paper I. The polarization of macrophages seems to be dependent on nanopattern size, according to the conclusions of *in vitro* investigations [163, 181]. One of these studies using UV-treated titanium nanotubes showed that M1 macrophage

polarization was promoted at nanotubes with a 80-nm diameter, while M2 macrophage polarization was promoted at nanotubes with a 30-nm diameter [163]. Another recent *in vitro* study showed that nanotopography does not affect the population of M1 macrophages, while nanotubes larger than 80 nm reduces the proportion of M2 macrophages [181]. This might reflect another aspect of surface modulation since M2 macrophages have a more complex range of functions, with subtypes that are both anti- and proinflammatory (M2a and M2b, respectively), interact with cells of the adaptive immune response (M2b) and affect matrix formation and tissue remodeling (M2c) [182]. Despite their anti-inflammatory functions, M2 macrophages have not been studied as extensively as proinflammatory M1 macrophages. It is obvious that knowledge about the inflammatory response to nanopatterned titanium implants is mainly based on *in vitro* molecular studies, as a limited number of *in vivo* studies are available.

In summary, the nanopatterned implants used in our first studies (Papers I and II) seem to attenuate the initial inflammatory response. The expression of the proinflammatory cytokine MCP-1 is downregulated, leading to reduced recruitment of macrophages to the nanopatterned implants. Additionally, TNF-α expression is downregulated. These findings may be consistent with those of wound- and bone fracture-healing studies. The administration of a low concentration of TNF-α to a murine tibial fracture model within 24 hours after injury resulted in augmented fracture repair [183]. Conversely, high doses of TNF-α had deleterious effects on the fractured ribs of rats with inhibited bone repair [184]. The effect of TNF-α seems to be time- and concentration-dependent, with its main effect being on the recruitment of mesenchymal stem cells [66, 185]. This suggests that an initial “moderate” increase in the secretion of a “moderate” amount of TNF-α by proinflammatory M1 macrophages after tissue trauma induced by the implantation process is mandatory for successful osseointegration. Disruption of this transient increase in TNF-α secretion, by, for example, paracrine regulatory secretion of IL-4 and IL-10 by M2 macrophages [186], may instead lead to fibrosis and encapsulation of the titanium implant [181]. Future research should aim to further characterize the molecular events of this inflammatory phase of bone healing.

In Paper III, the expression of TNF-α at the later phase of healing (6 days - 28 days) was significantly higher in cells on M implants than in those on MN implants after 21 days of healing. At 28 days, statistically higher expression was noted in cells on P implants compared to PN implants. This is in line with the expression levels of TNF-α and IL-1β at oxidized implants studied in the same animal model [21]. Both proinflammatory cytokines were expressed at

higher levels at machined implants during the observation period from 6 to 28 days of healing. After merging the time points in Paper III, significantly lower expression of TNF-α at MN implants was observed, with a significant difference between MN implants and P implants. Correlation analysis was performed to assess the synergistic effect of micro- and nanoscale roughness in downregulating the expression of TNF-α and thereby provide novel evidence of surface-specific modulation capabilities in the inflammatory phase.

Finally, the correlation analysis in Paper IV highlighted some additional interesting findings regarding the levels of inflammatory mediators in our patient group. Increasing age was associated with increased expression of proinflammatory TNF-α at the machined implants, which could have been a function of the additive effects of local and systemic factors. Machined implants elevate local expression of TNF-α [21-23]. Additionally, old age is associated with dysregulation of the cytokine network and homeostasis. The levels of proinflammatory cytokines, such as TNF-α, IL-1 and IL-6, can be elevated, while those of anti-inflammatory cytokines, such as IL-10, TGF-β and IL-37, can be reduced systemically [187]. An interesting finding, however, was that MN implants promoted the expression of the anti-inflammatory cytokine IL-10 instead. IL-10 has been implicated in the inhibition of bone resorption [125]. These findings warrant further investigation to determine the impact of these cytokines on the molecular mechanisms of osseointegration.

5.2.1 SYNERGISTIC EFFECTS OF TITANIUM IMPLANTS WITH MICRO- AND NANOSCALE ROUGHNESS ON OSSEOINTEGRATION

Nanotopography has been reported to have immunomodulatory properties due to the downregulation of TNF-α expression *in vitro* [140, 144, 145] (described in the Introduction, *Table 2*) and *in vivo* [135, 136] (Papers I and II). Thus, it seems that this effect can be further augmented for implants with combined nano- and microscale roughness (Paper III). To the author´s knowledge, this is reported here for the first time. Therefore, a review of the current knowledge about the synergistic effects of micro- and nanoscale characteristics on osseointegration was performed (*Table 11*). Only *in vitro* and *in vivo* studies comparing titanium implants with a well-characterized microroughness to implants with the same microroughness but additional well-characterized nanotopography were included.

Table 11. In vitro and in vivo studies emphasizing synergistic biological effects of micro- and nanoscale roughness on titanium surfaces.

Nanopattern shape/ degree of order/ production method	***Nanopattern dimensions*** ***Diameter /inter-particle distance or density/*** height or depth	***Micro-roughness pattern/ production method/ material***	***Surface characterization (topography)/ chemistry***	***In vitro/ in vivo***	***Main cell response or biological outcome***	***Ref***
Pits/ random roughness/ etching	*20 - 30 nm, 30 - 50 nm, 50 - 100 nm/* NR/ NR	Grooves in inconsistent directions, 0.5 - 1.0 μm, 1.0 - 1.5 μm, 1.5 - 2.0 μm/ Polishing and etching/ cpTi	*FE-SEM, AFM/* **different surface chemistry** between test and control implants determined by EDS	*In vitro*, h-BMMSCs *in vivo*, rat tibia	- number of adherent cells was higher based on immuno-fluorescence after 30 minutes, 1 hour and 2 hours on the substrates with combined micro- and nanotopography compared to polished substrates - ALP production and mineralization evaluated by ALP- and Alizarin Red staining, respectively, were both increased on the substrates with combined micro- and nanotopography compared to polished substrates - higher expression of Runx2, ALP and OC after 1-14 days of the growing cells by qPCR on the substrates with combined micro- and 50 – 100 nm nanotopography compared to polished substrates - higher BIC values after 3 months at the screw-shaped implants with combined micro- and nanotopography compared to polished screw-	[188]

					shaped implants with the implants with 1.5 – 2.0 µm microroughness and 50 – 100 nm features showing the highest values - higher pullout force values after 12 weeks at the screw-shaped implants with combined micro- and nanotopography compared to polished screw-shaped implants with the implants with 1.5 – 2.0 µm microroughness and 50 – 100 nm features showing the highest values	
Nano-protrusions/ random roughness/ oxidation	*73 nm, 61 nm on smooth micro- and rough-microscale substrates, respectively/* **NR/** NR	NR/ Machining (smooth microscale) or double acid etched (rough microscale/ Ti-alloy (Ti6Al4V)	*SEM, AFM, LCM/* **different surface chemistry** between control and test implants determined by XPS	*In vitro*, hOBs *in vitro*, hOBs	- enhanced osteogenic activity by higher expression of OC, BSP and osteoblastic differentiation by higher expression of BMP-2 and 4, GREM1 and NOG (= BMP-2 and 4 inhibitors) measured by qPCR (*mRNA levels*) after 7 days on rough microscale substrates with and without nanofeatures compared to smooth microscale substrates with and without nanofeatures - enhanced ALP and OC as well as VEGF and OPG *protein levels* assayed in the conditioned media after 24 hours culturing without supportive media on rough microscale substrates with nanofeatures compared to rough microscale and smooth microscale substrates with and without nanofeatures	[189] [190]
Nanotubes/ partially ordered/ anodization	*55 nm, 85 nm/* **NR/** NR	Micro-grooves with 100 µm, 50 µm, 20 µm, 10 µm and 5 µm width,	*SEM, AFM/* **NR –** but different fabrication methods employed for test	*In vitro*, human osteoblast-like cells	- higher cell viability determined by cell viability assays after 3 days on the substrates with combined micro- and nanotopography compared to microroughened substrates, with the highest values on substrates with microgrooves of 10 µm	[191]

		2 μm and 3,6 μm depth/ Photo-lithography, ICP-etching/ cpTi	and control substrates		width and 2 μm depth combined with 85 nm nanotubes	
Nanopores/ partially ordered/ anodization	50 nm, 70 nm/ **NR/** 8 μm, 12 μm	Micro-grooves/ Machining/ cpTi	FE-SEM, AFM/ **NR** - but different fabrication methods employed for test and control substrates	*In vitro*, primary murine BMM and murine cell line macrophages, hOBs, human gingival fibroblasts	- reduced proliferation of both macrophage cell types determined by cell counting after 1, 4 and 7 days on the substrate with combined microroughness and 70 nm nanopores compared to substrates with the same microroughness - osteoblasts and fibroblasts were morphologically elongated and confluent evaluated with SEM on the substrates with combined micro- and nanotopography suggesting improved adherence	[192]
Nanotubes/ partially ordered/ anodization	30 nm, 50 nm, 80 nm/ **NA/** NR	10-30 μm pits and 1-3 μm micropits/ Sandblasting with large grit and acid etching/ cpTi	FE-SEM/ **NR** - but different fabrication methods employed for test and control substrates	*in vitro*, hOBs	- higher protein adsorption rate as assayed after 1, 2 and 6 hours on the substrates with combined micro- and nanotopography compared to substrates with microroughness with the highest amount on the microroughened substrates with 30 nm nanotubes - number of adherent cells was higher determined by immunofluorescence after 30 minutes, 1 and 2 hours on the substrates with combined micro- and nanotopography compared to substrates with microroughness with the highest number on the microroughened substrates with 30 nm nanotubes	[193]

				in vivo, beagle dog tibia	- higher expression of Runx2 after 1 and 2 weeks in implant adherent cells evaluated by qPCR on the microroughened screw-shaped implants with 50 nm nanotubes compared to the other groups and control without nanotubes - higher expression of ALP and OC after 1 and 2 weeks in implant adherent cells evaluated by qPCR on the microroughened screw-shaped implants with 80 nm nanotubes compared to the other groups and control without nanotubes - higher BIC and BA values both after 2 and 4 weeks at the screw-shaped implants with combined micro- and nanotopography compared to screw-shaped implants with microroughness with the highest values on the microroughened with 80 nm nanotubes	

NR: not reported, CpTi: commercially pure titanium, NR: not reported, NA: not applicable, ICP etching: inductively coupled plasma etching, SEM: scanning electron microscope, AFM: atomic force microscopy, FE-SEM: field emission SEM, EDS: energy dispersive X-ray spectroscopy, XPS: X-ray photoelectron spectroscopy, hOBs: human osteoblasts, BIC: bone-to-implant contact, BA: bone area, BMM: bone marrow-derived macrophages, hBMMSCs: human bone marrow-derived mesenchymal stem cells, LCM: laser confocal microscopy, OC: osteocalcin, BSP: bone sialoprotein, BMP: bone morphogenetic protein, qPCR: quantitative polymerase chain reaction, ALP: alkaline phosphatase, OC: osteocalcin, VEGF: vascular endothelial growth factor, OPG: osteoprotegerin

In summary, nanotopography superimposed on microscale roughened surfaces seems to exert synergistic effects *in vitro* on the adhesion of MSCs, their differentiation towards the osteogenic lineage and the promotion of osteogenic activity and mineral deposition. The available *in vivo* evidence indicates that these synergistic effects results in a higher BIC, BA and biomechanical strength. During the promotion of bone formation, osteoclastogenesis was decreased. Furthermore, the proliferation of macrophages was inhibited.

5.2.2 INTEGRIN-MEDIATED CELL ADHESION

While the integrins expressed by osteoclasts are mainly $\alpha_v\beta_3$ integrin, which binds to several noncollagenous protein ligands, and $\alpha_2\beta_1$ integrin, which binds to collagen type I [194], osteoblasts seem to display a more complex integrin repertoire that depends on the degree of differentiation. The fibronectin receptor $\alpha_5\beta_1$ is abundantly expressed by osteoblasts and is critical for their differentiation *in vitro* [195]. Furthermore, the collagen receptor $\alpha_2\beta_1$ has also been shown to be expressed by osteoblasts at rather high levels during initial differentiation and at much lower levels after terminal differentiation, indicating its role in osteoblast differentiation from early progenitors [196]. It becomes apparent that the cell phenotype and the degree of differentiation can affect the expression profiles of integrins. In Paper II, higher expression of the single integrin chain β_1 was observed in the cells adherent to PN implants compared to those adherent to microroughened implants with and without nanopatterns after 1 day. Since this chain can be expressed in osteoblasts, osteoclasts [197] and MSCs [39], this finding is difficult to interpret. However, it corroborates the *in vitro* findings revealing that higher expression of integrin-β_1 in mouse BMSCs cultured on titanium nanopits compared to substrates with a combined submicro- and nanoscale topography accelerates osteoblast differentiation [198]. Although speculative, the nanotopography studied in the present research may upregulate the expression of these integrins, reflecting enhanced adhesion of both MSCs and osteoblasts and osteoclasts and leading to early osteogenic differentiation and accelerated bone regeneration and remodeling.

5.3 BONE REGENERATION

In Paper II, which evaluated the early molecular events of bone healing, the expression of the early osteoblastic marker OC in implant-adherent cells was significantly elevated at both nanopatterned implants (PN and MN) compared to their corresponding polished and machined controls after 3 days of healing. The same trend could also be seen for ALP, the expression of which was increased 2.2- and 2.6-fold at the PN and MN implants, respectively. These

findings are also in line with the findings for oxidized implants retrieved from rat tibia, which showed peak OC and ALP expression compared to those at machine implants after 3 days of healing [21, 22].

Furthermore, the enhanced osteogenic capacity of titanium nanotubes with diameters of 70 – 80 nm has been shown *in vitro* [145]. Cultured mouse-derived preosteoblast cells showed higher osteogenic activity due to higher gene expression levels of OC and ALP and OPN and ColX than Ti substrates with 30- to 40-nm nanotubes and flat controls, respectively, after 24 hours and 3 days. Additionally, culturing h-BMMSCs on Ti substrates with combined micro- and nanotopography compared to polished structures led to higher gene expression levels of OC, ALP and Runx2 [188]. Enhanced osteogenic activity was also confirmed *in vivo* in screw-shaped Ti implants with combined microroughness created by sandblasting with large grit and acid etching and thereafter embellished with 80-nm nanotubes via anodization, and upregulation of OC and ALP gene expression levels at such implants compared to control microroughened substrates with other nanotubes was observed in the beagle dog tibia after 1 and 2 weeks [193].

These molecular findings of increased OC and ALP gene expression levels were corroborated by histological evaluations in Paper II, which revealed increased osteoid formation at 3 days at both PN and MN implants. Immunohistochemistry (Papers I and II) showed higher extracellular periostin staining at the same time point, indicating intramembranous bone formation [199].

The enhancement of osteogenic activity, as determined by the expression of OC and ALP in implant-adherent cells in the human study (Paper IV), is in line with our findings in a small rodent animal model (Papers I and II) with the exception of temporal differences. Furthermore, the finding that osteoblastic differentiation results from higher expression levels of the growth factor BMP-2 and the transcription factor Runx2 extends previous findings in *in vitro* murine BMSCs cultured on substrates with 100-nm nanotubes compared to 30-nm nanotubes and polished substrates for 3 days [133]. Moreover, in an *in vivo* setting, cylindrical anodized implants were studied in the frontal skull bones of minipigs. Increases in both osteogenic activity (ALP and ColI expression) and osteoblastic differentiation (the expression of osterix, OSX; a transcription factor downstream of Runx2) were demonstrated in implant-adherent cells on 70-nm nanotubes compared with machined implants after 1, 2, 3, 4 and 5 weeks [168]. Furthermore, in a human study, random nanotopography in the range of 50 – 200 nm created on grit-blasted Ti implants by acid etching led to significant elevation of the expression levels of OC and

OSX after seven days [179]. In this study, nanotopography was created by hydrofluoric acid (HF) treatment, implying that the surface was chemically altered and resulting in a confounding factor that has to be considered.

In summary, the nanopatterned topography under investigation with semispherical protrusions with diameters 51 – 79 nm seems to enhance bone formation. This was confirmed by the higher expression levels of both osteoblastic differentiation and osteogenic activity markers. This is the first human study to report the molecular mechanisms involved in osseointegration of titanium implants with a well-defined and characterized nanotopography.

5.4 REMODELING

While there is a plethora of *in vitro* studies supporting the osteogenic capacity of nanopatterned titanium surfaces [126, 128, 130-133, 142, 143, 145, 148-150, 152], only a few studies are available on the effect of nanotopography on osteoclasts. In Paper II, osteoclast activity assessed by CatK expression, which was upregulated early at 1 day for the PN and MN implants but downregulated at MN implants in Paper I after 6 days. This was in line with the significantly lower expression of RANKL at MN implants than at all the other implants at the same time point in Paper III. In the same animal model, gene expression analyses of cells adhered to machined and oxidized implants showed that CatK and TRAP are expressed early, with levels peaking at 3 days, and the increase in expression levels at oxidized implants was maintained until the end of the observation period of 28 days [21, 22]. While these findings disagree with the present results, the downregulatory effects of osteoclast activity and osteoclastogenesis caused by surface nanotopography, as seen in Papers I and III, have been described *in vitro*. Lower expression levels of RANKL and M-CSF and higher expression of OPG were observed after BMSCs were cultured on titanium substrates with 30-nm nanotubes in conditioned medium originating from macrophages cultured on the same substrates compared to polished substrates after 7 days [132]. Similarly, the expression of TRAP in osteoclasts was downregulated after hBMSCs and hBMHCs were cocultured on titanium substrate with 15-nm nanodots after 28 days, while the expression of OPG was also elevated at the same time [148]. Moreover, compared to implantation of machined implants, implantation of 70-nm nanotubes produced by anodization in the frontal skull bones of minipigs resulted in enhanced expression of TRAP after 1, 2, 3, 4 and 5 weeks of healing [168]. However, these results were obtained in peri-implant bone samples rather than implant-adherent cells.

The relationships between titanium implant surface properties, the osteoclastic markers CatK and TRAP and the RANK-RANKL-OPG triad during bone healing are not understood. The present *in vivo* studies (Papers I and III) indicate that osteoclast function is decreased at MN implants with 75- to 79-nm semispherical nanopatterns. It can be hypothesized that such inhibitory effects on osteoclasts are linked to the anti-inflammatory and immunomodulatory properties of particular nanopatterns. For instance, it is known that TNF-α enhances IL-1 expression, which in turn can induce RANKL expression [200]. Consequently, the decrease in the expression of TNF-α induced by the nanotopography might inhibit osteoclastogenesis through the RANKL/RANK/OPG pathway. However, this assumption requires additional verification.

5.5 STRUCTURAL AND FUNCTIONAL ASPECTS OF OSSEOINTEGRATION OF NANOPATTERNED IMPLANTS

The early osteoblastic activity and inhibitory effects on bone resorption at MN implants may lead to a higher net bone formation at an earlier time point. This assumption is supported by the higher BIC at MN implants seen after 6 days of healing. A higher BIC and bone volume in the rat femur have been seen for screw-shaped implants with 30-nm nanotubes than for implants with polished surfaces after later healing time points of 2, 4 and 12 weeks [132]. These findings have been further extended to cylindrical implants with nanodots 15 nm in height implanted in the rabbit femur and retrieved after 2 months, which showed 20% higher BIC than the polished controls [148].

Bone-to-implant contact, which is influenced by surface physicochemical properties, has been shown to be positively correlated with RTQ [4, 201]. This was found for MN implants after 6 and 21 days of healing in Paper III. Compared to machined implants, machined screw-shaped implants with random nanotopography produced by laser ablation increased removal torque 270% and 170% after 8 weeks and 6 months of healing, respectively, in a rabbit model [166, 167]. This synergistic effect of micro- and nanoscale topography was in line with our findings in Paper III.

In summary, nanotopography seems to enhance early BIC and RTQ. The effect on RTQ is potentiated by a synergistic effect of the different length scale topographies (nanoscale superimposed on microscale topography).

5.6 SIGNIFICANCE OF NANOPATTERN SHAPE, SIZE AND INTERPARTICLE DISTANCE ON BONE FORMATION AND INFLAMMATION

Research on the effects of titanium implants with topographic nanopatterns on osseointegration is still in its infancy. A clear advantage of nanopatterns is that they increase the surface area, offering a larger area for protein and protein-cell interactions. The optimal geometry and scale of nanotopography on titanium implants for enhancing osseointegration are largely unknown due to the limited number of studies using ordered or partially ordered nanotopography. The effects of randomly produced nanotopography are challenging to quantify due to poor reproducibility.

Regarding *in vitro* studies employing both titanium and polymers, some trends can be seen in shape, size and interparticle distance. Grooves appear to modulate bone healing at the microscale. In an *in vitro* study, compared to flat surfaces, grooves with depths on the micron- and submicron scales, i.e., ranging from 306 nm to 2 μm, on poly(lactic-co-glycolic acid) substrates promoted osteoblast alignment [202]. However, it has also been shown that osteoblast cell alignment is increased on grooves with dimensions as small as 75 nm in width and 33 nm in depth compared to grooves with varying widths (500 – 75 nm) and depths (158 – 33 nm) and smooth polystyrene substrates [128]. The same study indicated that both osteoblast alignment and focal adhesions (FAs) decrease with a decrease in groove pitch. Modulation of the inflammatory response by nanogrooves is limited, as a combined *in vitro/in vivo* study showed that the expression of the proinflammatory cytokines TNF-α and IL-β was upregulated at nanogrooves created on Si-wafers and coated with a titanium layer with depths of 33, 49 and 158 nm and compared to smooth surfaces after subcutaneous implantation for 14 days in mice [203].

Compared to those with smaller diameters created on polycaprolactone, pits with diameters on the microscale, i.e., in the range of 30 – 40 μm, promote osteogenic activity [204]. Nanopits with a 120-nm diameter and a depth of 100 nm on polycarbonate have been shown to have negative effects on osteoblasts, reducing spreading and adhesion [205]. The authors claimed that the reason for these effects might be that ordered pits cannot provide sufficient cues for osteoblasts. Random placement instead of the same pits with a center-to-center spacing of 300 nm on polymethylmethacrylate (PMMA) increased osteogenic activity of human osteoprogenitors and cultured MSCs after 21 and 28 days of culturing, respectively [206]. The inflammatory response of these nanopits

(120 nm in diameter, 100 nm in depth and 300 nm in pitch) was evaluated in a combined *in vitro*/*in vivo* study by another research group [159]. Compared to those on polystyrene, which was used as a control, nanopits manufactured on biodegradable polyester inhibited the secretion of IL-6 and TNF-α by murine fibroblasts after 72 hours of culture.

Unlike polished surfaces and taller pillars, dots on titanium with a size of 15 nm and a center-to-center spacing of 40 nm have been reported to promote the osteoblastic differentiation of hMSCs [150, 151]. Moreover, unlike 20-nm dots and 35-nm dots on SiO_2 substrates, 50-nm pillars with a center-to-center distance of 50 nm have been shown to promote osteoblastic differentiation of MSCs [207]. When evaluating the inflammatory response, higher expression of TNF-α in mouse macrophages was observed on 50-nm dots than on 10-nm dots fabricated on Si wafers sputter-coated with tantalum nitride and aluminum prior to anodization and after 72 hours of culture [208].

Nanotubes on titanium substrates promote osteogenic differentiation *in vitro*. Nanotubes with a diameter of 15 nm enhance MSC differentiation after 2 weeks, osteoblast proliferation after 3 days and osteoclast differentiation after 7 days, unlike nanotubes with a diameter of 100 nm, which inhibit these processes [209, 210]. Another *in vitro* study showed the opposite results: nanotubes in the range 70-100 nm enhanced the osteogenic activity of mouse osteoblasts after 48 hours, while smaller 30-nm tubes elicited higher adhesion in the first 2 days [211]. Furthermore, nanotubes in the range of 70-100 nm have been shown in other *in vitro* studies to ultimately promote bone formation [133, 142, 143, 145] (described in the Introduction, *Table 2*). The diameter of titanium nanotubes that promoted the bone response *in vivo* is in accordance with the *in vitro* studies. Therefore, *in vivo* evidence suggests that nanotubes that are 30 nm [132, 133] and 70 nm [168, 212, 213] in diameter more strongly induce osteoconductivity. Regarding the inflammatory response, compared to 30- to 40-nm nanotubes and flat controls, titanium nanotubes that are 70-80 nm in diameter have been shown to decrease the expression levels of TNF-α and IL-1β in murine macrophages after 12 hours of culture to promote M2 polarization [145]. In contrast, another study indicated a lower M1/M2 ratio of mouse macrophages at substrates with 30-nm nanotubes compared to those with 100-nm nanotubes after 3 days of culture [133]. The optimal nanotube size continues to be debated since the chemical composition of TiO_2 is simultaneously affected during the manufacturing process, as is the crystallinity since annealing is often applied.

In summary, there have been only a limited number of *in vivo* studies on partially ordered or highly ordered topographic nanopatterns on titanium

implants. Some trends in osteogenic capacity and inflammatory modulation in relation to dimensional parameters can be seen from these studies in conjunction with the *in vitro* studies on titanium and other polymers, as outlined above. However, more studies are needed to further support these results.

5.7 CONCLUDING REMARKS

The present thesis has contributed to the development of an experimental screw-shaped implant with partially ordered nanotopography stabilized on background microtopography. This nanotopography is highly reproducible, offering the capacity to amplify favorable patterns. Moreover, it can also be used to tune the nanopattern dimensions in a controllable manner, providing the opportunity to further investigate the biological responses elicited during osseointegration across other sizes.

In the current thesis, it was shown that semispherical nanopatterns with diameters of 51-79 nm attenuate the early inflammatory response. Furthermore, this nanotopography positively affects bone formation while decreasing bone resorption in the early healing phase. The early molecular findings, i.e., decreased TNF-α, MCP-1, CatK and RANKL expression and increased OC expression at nanopatterned implants, corroborated the morphological and biomechanical findings. The early enhanced bone-to-implant contact is coupled to increased initial implant anchorage, as measured by the RTQ of implants with a combined micro- and nanoroughened topography. Finally, the osteogenic capacity of nanotopography shown in experimental animals was also confirmed in humans for the first time.

6 CONCLUSION

Titanium implant surfaces with well characterized nanotopography consisting of semispherical patterns with diameter 51-79 nm downregulated the early inflammatory phase. Furthermore, early osteogenic activity was increased in conjunction with a decreased osteoclastogenesis and osteoclastic activity. These processes led to an early higher bone-to-implant contact at the nanopatterned surfaces superimposed on implants with a machined microtopography. This morphologic observation was further corroborated with higher removal torque values denoting an early biomechanical anchorage of the implants with combined nano- and microscale topography.

7 FUTURE PERSPECTIVES

The present thesis demonstrated that titanium surface nanotopography attenuates the initial inflammatory reaction while promoting bone formation. Furthermore, osteoclastogenesis and osteoclast activity were downregulated. These findings are mainly based on our experimental animal studies, with the human study confirming the osteogenic effect of the nanopatterns used. Therefore, it would be interesting to further verify the molecular findings in humans with proteomics and further correlate to morphological (histology) and biomechanical (removal torque) evaluations.

Additionally, the exploration of the early inflammatory phase with both molecular and morphological tools would also be very intriguing in humans since the knowledge in this field is very limited. The biological effects in the bone tissue interface of commercially available implants with moderate microroughness but with the addition of the studied nanotopography would be of value. The hypothesis is that the synergistic topographic effects downregulate the initial inflammatory reaction and promote early bone formation. The clinical application of these implants would be in the elderly population and patients with degenerative diseases such as rheumatoid arthritis, osteoarthritis and osteoporosis, all leading to a disturbance of the inflammatory cytokine homeostasis towards the proinflammatory state. Thus, the regulation of inflammation in early bone regeneration is a promising area in these patient groups. Nanotopography has a potential to be standard on different biomaterials in the future but more investigations are needed.

ACKNOWLEDGEMENT

I wish to express my sincere gratitude and appreciation to all who made this thesis possible.

First of all, I would like to thank my main supervisor Lars Rasmusson for your encouragement and guidance throughout these years. You always made time to discuss everything, from science and clinics to life itself. I am forever grateful for your support.

My deepest gratitude to my co-supervisor Peter Thomsen who gave me the opportunity to perform research within the field of biomaterials. I ´m deeply impressed of your broad knowledge and willingness to share and help, always respecting the ethical and academic values.

My sincere gratitude to my co-supervisor Omar Omar for always being available to support and guide me. Always enthusiastic with plenty of knowledge and full of innovative ideas. I would not stand here without your contribution.

My sincere gratitude also to my co-supervisor Sarunas Petronis for your patience and encouragement throughout the years. Thank you for sharing your technical expertise and knowledge and involving me in inspiring discussions. Your contribution has been indispensable and I feel very lucky to have you in my project.

The warmest appreciation to my co-authors; Hossein Agheli, Ahmed Ballo, Anders Palmquist and Furqan Ali Shah. Thanks for a very fruitful collaboration!

My deepest thanks to all laboratory co-workers at the department of Biomaterial at University of Gothenburg and especially Lena Emanuelsson, Birgitta Norlindh and Anna Johansson.

Thanks to my mentor at the Department of Oral and Maxillofacial surgery Mats Wallström for all support and giving me time off the clinics to pursue research.

A lot of thanks to all my colleagues and friends at the department of Biomaterials and the administrative team, Magnus Wassenius and Rose Marie

Tschina. All my colleagues and friends at the department of Oral and Maxillofacial surgery.

Finally, I would like to thank my family;
My wife, Vicky, and my children Zoe and Georgios, you are the greatest gift in my life.
My mother Athanasia and my father Georgios for your sacrifices and unconditional support through my life. Dad, you are always with me! My sisters, for your love and encouragement.
My grandparents, Giannis and Sofia, who taught me in an early age the values of family and hard work.

Financial support for different studies in the present thesis was kindly provided by the Swedish Research Council (2018-02891), the BIOMATCELL VINN Excellence Center of Biomaterials and Cell Therapy, the Västra Götaland Region, the Swedish state under the agreement between the Swedish government and the county councils, the ALF agreement (ALFGBG-725641), the TUA/Region Västra Götaland research grant, the Handlanden Hjalmar Svensson Foundation, the IngaBritt and Arne Lundberg Foundation, and the Area of Advance Materials of Chalmers and GU Biomaterials within the Strategic Research Area initiative launched by the Swedish government.

REFERENCES

[1] P.I. Branemark, B.O. Hansson, R. Adell, U. Breine, J. Lindstrom, O. Hallen, A. Ohman, Osseointegrated implants in the treatment of the edentulous jaw. Experience from a 10-year period, Scand J Plast Reconstr Surg Suppl 16 (1977) 1-132.
[2] A. Palmquist, O.M. Omar, M. Esposito, J. Lausmaa, P. Thomsen, Titanium oral implants: surface characteristics, interface biology and clinical outcome, J R Soc Interface 7 Suppl 5 (2010) S515-27.
[3] L. Claes, S. Recknagel, A. Ignatius, Fracture healing under healthy and inflammatory conditions, Nat Rev Rheumatol 8(3) (2012) 133-43.
[4] D.D. Bosshardt, V. Chappuis, D. Buser, Osseointegration of titanium, titanium alloy and zirconia dental implants: current knowledge and open questions, Periodontol 2000 73(1) (2017) 22-40.
[5] G.E. Salvi, D.D. Bosshardt, N.P. Lang, I. Abrahamsson, T. Berglundh, J. Lindhe, S. Ivanovski, N. Donos, Temporal sequence of hard and soft tissue healing around titanium dental implants, Periodontol 2000 68(1) (2015) 135-52.
[6] T.A. Einhorn, L.C. Gerstenfeld, Fracture healing: mechanisms and interventions, Nat Rev Rheumatol 11(1) (2015) 45-54.
[7] T. Albrektsson, C. Johansson, Osteoinduction, osteoconduction and osseointegration, Eur Spine J 10 Suppl 2 (2001) S96-101.
[8] T. Albrektsson, P.I. Branemark, H.A. Hansson, J. Lindstrom, Osseointegrated titanium implants. Requirements for ensuring a long-lasting, direct bone-to-implant anchorage in man, Acta Orthop Scand 52(2) (1981) 155-70.
[9] Z.S. Ai-Aql, A.S. Alagl, D.T. Graves, L.C. Gerstenfeld, T.A. Einhorn, Molecular mechanisms controlling bone formation during fracture healing and distraction osteogenesis, J Dent Res 87(2) (2008) 107-18.
[10] T. Ziebart, A. Schnell, C. Walter, P.W. Kämmerer, A. Pabst, K.M. Lehmann, J. Ziebart, M.O. Klein, B. Al-Nawas, Interactions between endothelial progenitor cells (EPC) and titanium implant surfaces, Clin Oral Investig 17(1) (2013) 301-9.
[11] K.L. Spiller, R.R. Anfang, K.J. Spiller, J. Ng, K.R. Nakazawa, J.W. Daulton, G. Vunjak-Novakovic, The role of macrophage phenotype in vascularization of tissue engineering scaffolds, Biomaterials 35(15) (2014) 4477-88.
[12] A.L. Raines, R. Olivares-Navarrete, M. Wieland, D.L. Cochran, Z. Schwartz, B.D. Boyan, Regulation of angiogenesis during osseointegration by titanium surface microstructure and energy, Biomaterials 31(18) (2010) 4909-17.

[13] A.A. Mamalis, D.L. Cochran, The role of hypoxia in the regulation of osteogenesis and angiogenesis coupling in intraoral regenerative procedures: a review of the literature, Int J Periodontics Restorative Dent 33(4) (2013) 519-24.
[14] A.H. Simpson, L. Mills, B. Noble, The role of growth factors and related agents in accelerating fracture healing, J Bone Joint Surg Br 88(6) (2006) 701-5.
[15] P.J. Bouletreau, S.M. Warren, J.A. Spector, Z.M. Peled, R.P. Gerrets, J.A. Greenwald, M.T. Longaker, Hypoxia and VEGF up-regulate BMP-2 mRNA and protein expression in microvascular endothelial cells: implications for fracture healing, Plast Reconstr Surg 109(7) (2002) 2384-97.
[16] F. Schwarz, M. Herten, M. Sager, M. Wieland, M. Dard, J. Becker, Histological and immunohistochemical analysis of initial and early osseous integration at chemically modified and conventional SLA titanium implants: preliminary results of a pilot study in dogs, Clin Oral Implants Res 18(4) (2007) 481-8.
[17] R.E. Marx, Platelet-rich plasma: evidence to support its use, J Oral Maxillofac Surg 62(4) (2004) 489-96.
[18] J. Lee, H. Byun, S.K. Madhurakkat Perikamana, S. Lee, H. Shin, Current Advances in Immunomodulatory Biomaterials for Bone Regeneration, Adv Healthc Mater 8(4) (2019) e1801106.
[19] S. Ivanovski, S. Hamlet, G.E. Salvi, G. Huynh-Ba, D.D. Bosshardt, N.P. Lang, N. Donos, Transcriptional profiling of osseointegration in humans, Clin Oral Implants Res 22(4) (2011) 373-81.
[20] E. Kolaczkowska, P. Kubes, Neutrophil recruitment and function in health and inflammation, Nat Rev Immunol 13(3) (2013) 159-75.
[21] O.M. Omar, M.E. Lennerås, F. Suska, L. Emanuelsson, J.M. Hall, A. Palmquist, P. Thomsen, The correlation between gene expression of proinflammatory markers and bone formation during osseointegration with titanium implants, Biomaterials 32(2) (2011) 374-86.
[22] O. Omar, S. Svensson, N. Zoric, M. Lenneras, F. Suska, S. Wigren, J. Hall, U. Nannmark, P. Thomsen, In vivo gene expression in response to anodically oxidized versus machined titanium implants, J Biomed Mater Res A 92(4) (2010) 1552-66.
[23] S. Sayardoust, O. Omar, O. Norderyd, P. Thomsen, Implant-associated gene expression in the jaw bone of smokers and nonsmokers: A human study using quantitative qPCR, Clin Oral Implants Res 29(9) (2018) 937-953.
[24] O. Omar, M. Lenneras, S. Svensson, F. Suska, L. Emanuelsson, J. Hall, U. Nannmark, P. Thomsen, Integrin and chemokine receptor gene expression in implant-adherent cells during early osseointegration, J Mater Sci Mater Med 21(3) (2010) 969-80.
[25] C. Laudanna, J.Y. Kim, G. Constantin, E. Butcher, Rapid leukocyte integrin activation by chemokines, Immunol Rev 186 (2002) 37-46.

[26] S.M. Tan, The leucocyte beta2 (CD18) integrins: the structure, functional regulation and signalling properties, Biosci Rep 32(3) (2012) 241-69.
[27] C. Eriksson, J. Lausmaa, H. Nygren, Interactions between human whole blood and modified TiO2-surfaces: influence of surface topography and oxide thickness on leukocyte adhesion and activation, Biomaterials 22(14) (2001) 1987-96.
[28] C. Shi, E.G. Pamer, Monocyte recruitment during infection and inflammation, Nat Rev Immunol 11(11) (2011) 762-74.
[29] G.C. Gurtner, S. Werner, Y. Barrandon, M.T. Longaker, Wound repair and regeneration, Nature 453(7193) (2008) 314-21.
[30] O. Soehnlein, L. Lindbom, Phagocyte partnership during the onset and resolution of inflammation, Nat Rev Immunol 10(6) (2010) 427-39.
[31] J. Kzhyshkowska, A. Gudima, V. Riabov, C. Dollinger, P. Lavalle, N.E. Vrana, Macrophage responses to implants: prospects for personalized medicine, J Leukoc Biol 98(6) (2015) 953-62.
[32] N. Kojima, S. Ozawa, Y. Miyata, H. Hasegawa, Y. Tanaka, T. Ogawa, High-throughput gene expression analysis in bone healing around titanium implants by DNA microarray, Clin Oral Implants Res 19(2) (2008) 173-81.
[33] Y. Nakashima, D.H. Sun, M.C. Trindade, L.E. Chun, Y. Song, S.B. Goodman, D.J. Schurman, W.J. Maloney, R.L. Smith, Induction of macrophage C-C chemokine expression by titanium alloy and bone cement particles, J Bone Joint Surg Br 81(1) (1999) 155-62.
[34] S. Otsuru, K. Tamai, T. Yamazaki, H. Yoshikawa, Y. Kaneda, Circulating bone marrow-derived osteoblast progenitor cells are recruited to the bone-forming site by the CXCR4/stromal cell-derived factor-1 pathway, Stem Cells 26(1) (2008) 223-34.
[35] X. Wang, Y. Wang, W. Gou, Q. Lu, J. Peng, S. Lu, Role of mesenchymal stem cells in bone regeneration and fracture repair: a review, Int Orthop 37(12) (2013) 2491-8.
[36] C. Yellowley, CXCL12/CXCR4 signaling and other recruitment and homing pathways in fracture repair, Bonekey Rep 2 (2013) 300.
[37] D.J. Ceradini, A.R. Kulkarni, M.J. Callaghan, O.M. Tepper, N. Bastidas, M.E. Kleinman, J.M. Capla, R.D. Galiano, J.P. Levine, G.C. Gurtner, Progenitor cell trafficking is regulated by hypoxic gradients through HIF-1 induction of SDF-1, Nat Med 10(8) (2004) 858-64.
[38] C.C. Biguetti, F. Cavalla, E.M. Silveira, A.C. Fonseca, A.E. Vieira, A.P. Tabanez, D.C. Rodrigues, A.P.F. Trombone, G.P. Garlet, Oral implant osseointegration model in C57Bl/6 mice: microtomographic, histological, histomorphometric and molecular characterization, J Appl Oral Sci 26 (2018) e20170601.
[39] M. Ullah, D.D. Liu, A.S. Thakor, Mesenchymal Stromal Cell Homing: Mechanisms and Strategies for Improvement, iScience 15 (2019) 421-438.

[40] F. Granero-Molto, J.A. Weis, M.I. Miga, B. Landis, T.J. Myers, L. O'Rear, L. Longobardi, E.D. Jansen, D.P. Mortlock, A. Spagnoli, Regenerative effects of transplanted mesenchymal stem cells in fracture healing, Stem Cells 27(8) (2009) 1887-98.
[41] C. Zhou, A.T. Xu, D.D. Wang, G.F. Lin, T. Liu, F.M. He, The effects of Sr-incorporated micro/nano rough titanium surface on rBMSC migration and osteogenic differentiation for rapid osteointegration, Biomater Sci 6(7) (2018) 1946-1961.
[42] M. Honczarenko, Y. Le, M. Swierkowski, I. Ghiran, A.M. Glodek, L.E. Silberstein, Human bone marrow stromal cells express a distinct set of biologically functional chemokine receptors, Stem Cells 24(4) (2006) 1030-41.
[43] Y. Shao, F. Zhou, D. He, L. Zhang, J. Shen, Overexpression of CXCR7 promotes mesenchymal stem cells to repair phosgene-induced acute lung injury in rats, Biomed Pharmacother 109 (2019) 1233-1239.
[44] D.T. Scadden, The stem-cell niche as an entity of action, Nature 441(7097) (2006) 1075-9.
[45] T. Squillaro, G. Peluso, U. Galderisi, Clinical Trials With Mesenchymal Stem Cells: An Update, Cell Transplant 25(5) (2016) 829-48.
[46] A. De Ranieri, A.S. Virdi, S. Kuroda, S. Shott, Y. Dai, D.R. Sumner, Local application of rhTGF-beta2 modulates dynamic gene expression in a rat implant model, Bone 36(5) (2005) 931-40.
[47] N. Donos, S. Hamlet, N.P. Lang, G.E. Salvi, G. Huynh-Ba, D.D. Bosshardt, S. Ivanovski, Gene expression profile of osseointegration of a hydrophilic compared with a hydrophobic microrough implant surface, Clin Oral Implants Res 22(4) (2011) 365-72.
[48] K. Abula, T. Muneta, K. Miyatake, J. Yamada, Y. Matsukura, M. Inoue, I. Sekiya, D. Graf, A.N. Economides, V. Rosen, K. Tsuji, Elimination of BMP7 from the developing limb mesenchyme leads to articular cartilage degeneration and synovial inflammation with increased age, FEBS Lett 589(11) (2015) 1240-8.
[49] H.H. Luu, W.X. Song, X. Luo, D. Manning, J. Luo, Z.L. Deng, K.A. Sharff, A.G. Montag, R.C. Haydon, T.C. He, Distinct roles of bone morphogenetic proteins in osteogenic differentiation of mesenchymal stem cells, J Orthop Res 25(5) (2007) 665-77.
[50] M. Wu, G. Chen, Y.P. Li, TGF-beta and BMP signaling in osteoblast, skeletal development, and bone formation, homeostasis and disease, Bone Res 4 (2016) 16009.
[51] M. Monjo, S.F. Lamolle, S.P. Lyngstadaas, H.J. Rønold, J.E. Ellingsen, In vivo expression of osteogenic markers and bone mineral density at the surface of fluoride-modified titanium implants, Biomaterials 29(28) (2008) 3771-80.

[52] G.S. Stein, J.B. Lian, A.J. van Wijnen, J.L. Stein, M. Montecino, A. Javed, S.K. Zaidi, D.W. Young, J.Y. Choi, S.M. Pockwinse, Runx2 control of organization, assembly and activity of the regulatory machinery for skeletal gene expression, Oncogene 23(24) (2004) 4315-29.
[53] T. Komori, H. Yagi, S. Nomura, A. Yamaguchi, K. Sasaki, K. Deguchi, Y. Shimizu, R.T. Bronson, Y.H. Gao, M. Inada, M. Sato, R. Okamoto, Y. Kitamura, S. Yoshiki, T. Kishimoto, Targeted disruption of Cbfa1 results in a complete lack of bone formation owing to maturational arrest of osteoblasts, Cell 89(5) (1997) 755-64.
[54] J. Guo, R.J. Padilla, W. Ambrose, I.J. De Kok, L.F. Cooper, The effect of hydrofluoric acid treatment of TiO2 grit blasted titanium implants on adherent osteoblast gene expression in vitro and in vivo, Biomaterials 28(36) (2007) 5418-25.
[55] S.F. Taxt-Lamolle, M. Rubert, H.J. Haugen, S.P. Lyngstadaas, J.E. Ellingsen, M. Monjo, Controlled electro-implementation of fluoride in titanium implant surfaces enhances cortical bone formation and mineralization, Acta Biomater 6(3) (2010) 1025-32.
[56] S. Vimalraj, Alkaline phosphatase: Structure, expression and its function in bone mineralization, Gene 754 (2020) 144855.
[57] H.I. Roach, Why does bone matrix contain non-collagenous proteins? The possible roles of osteocalcin, osteonectin, osteopontin and bone sialoprotein in bone mineralisation and resorption, Cell Biol Int 18(6) (1994) 617-28.
[58] H.M. Horton MA, Integrins and Development: Integrins in Skeletal Cell Function and Development, Database https://www.ncbi.nlm.nih.gov/books/NBK6331/ Austin (TX): Landes Bioscience; 2000-2013.
[59] T.A. Einhorn, The cell and molecular biology of fracture healing, Clin Orthop Relat Res (355 Suppl) (1998) S7-21.
[60] F. Marco, F. Milena, G. Gianluca, O. Vittoria, Peri-implant osteogenesis in health and osteoporosis, Micron 36(7-8) (2005) 630-44.
[61] C. Colnot, D.M. Romero, S. Huang, J. Rahman, J.A. Currey, A. Nanci, J.B. Brunski, J.A. Helms, Molecular analysis of healing at a bone-implant interface, J Dent Res 86(9) (2007) 862-7.
[62] N.H. Hart, R.U. Newton, J. Tan, T. Rantalainen, P. Chivers, A. Siafarikas, S. Nimphius, Biological basis of bone strength: anatomy, physiology and measurement, J Musculoskelet Neuronal Interact 20(3) (2020) 347-371.
[63] T.A. Franz-Odendaal, B.K. Hall, P.E. Witten, Buried alive: how osteoblasts become osteocytes, Dev Dyn 235(1) (2006) 176-90.
[64] L.F. Bonewald, The amazing osteocyte, J Bone Miner Res 26(2) (2011) 229-38.
[65] F.A. Shah, X. Wang, P. Thomsen, K. Grandfield, A. Palmquist, High-Resolution Visualization of the Osteocyte Lacuno-Canalicular Network

Juxtaposed to the Surface of Nanotextured Titanium Implants in Human, ACS Biomater Sci Eng 1(5) (2015) 305-313.
[66] X. Fu, B. Han, S. Cai, Y. Lei, T. Sun, Z. Sheng, Migration of bone marrow-derived mesenchymal stem cells induced by tumor necrosis factor-alpha and its possible role in wound healing, Wound Repair Regen 17(2) (2009) 185-91.
[67] A.L. Ponte, E. Marais, N. Gallay, A. Langonne, B. Delorme, O. Herault, P. Charbord, J. Domenech, The in vitro migration capacity of human bone marrow mesenchymal stem cells: comparison of chemokine and growth factor chemotactic activities, Stem Cells 25(7) (2007) 1737-45.
[68] I. Von Luttichau, M. Notohamiprodjo, A. Wechselberger, C. Peters, A. Henger, C. Seliger, R. Djafarzadeh, R. Huss, P.J. Nelson, Human adult CD34-progenitor cells functionally express the chemokine receptors CCR1, CCR4, CCR7, CXCR5, and CCR10 but not CXCR4, Stem Cells Dev 14(3) (2005) 329-36.
[69] L.K. Bi, N. Zhou, C. Liu, F.D. Lu, T.X. Lin, X.J. Xuan, C. Jiang, J.L. Han, H. Huang, C.X. Zhang, W. Dong, H. Liu, J. Huang, K.W. Xu, Kidney cancer cells secrete IL-8 to activate Akt and promote migration of mesenchymal stem cells, Urol Oncol 32(5) (2014) 607-12.
[70] Y. Hou, C.H. Ryu, J.A. Jun, S.M. Kim, C.H. Jeong, S.S. Jeun, IL-8 enhances the angiogenic potential of human bone marrow mesenchymal stem cells by increasing vascular endothelial growth factor, Cell Biol Int 38(9) (2014) 1050-9.
[71] C.M. Champagne, J. Takebe, S. Offenbacher, L.F. Cooper, Macrophage cell lines produce osteoinductive signals that include bone morphogenetic protein-2, Bone 30(1) (2002) 26-31.
[72] R.P. Pirraco, R.L. Reis, A.P. Marques, Effect of monocytes/macrophages on the early osteogenic differentiation of hBMSCs, J Tissue Eng Regen Med 7(5) (2013) 392-400.
[73] V. Nicolaidou, M.M. Wong, A.N. Redpath, A. Ersek, D.F. Baban, L.M. Williams, A.P. Cope, N.J. Horwood, Monocytes induce STAT3 activation in human mesenchymal stem cells to promote osteoblast formation, PLoS One 7(7) (2012) e39871.
[74] O.M. Omar, C. Graneli, K. Ekstrom, C. Karlsson, A. Johansson, J. Lausmaa, C.L. Wexell, P. Thomsen, The stimulation of an osteogenic response by classical monocyte activation, Biomaterials 32(32) (2011) 8190-204.
[75] P. Guihard, Y. Danger, B. Brounais, E. David, R. Brion, J. Delecrin, C.D. Richards, S. Chevalier, F. Redini, D. Heymann, H. Gascan, F. Blanchard, Induction of osteogenesis in mesenchymal stem cells by activated monocytes/macrophages depends on oncostatin M signaling, Stem Cells 30(4) (2012) 762-72.
[76] T.J. Fernandes, J.M. Hodge, P.P. Singh, D.G. Eeles, F.M. Collier, I. Holten, P.R. Ebeling, G.C. Nicholson, J.M. Quinn, Cord blood-derived

macrophage-lineage cells rapidly stimulate osteoblastic maturation in mesenchymal stem cells in a glycoprotein-130 dependent manner, PLoS One 8(9) (2013) e73266.
[77] Y. Zhang, T. Bose, R.E. Unger, J.A. Jansen, C.J. Kirkpatrick, J. van den Beucken, Macrophage type modulates osteogenic differentiation of adipose tissue MSCs, Cell Tissue Res 369(2) (2017) 273-286.
[78] J. Pajarinen, T. Lin, E. Gibon, Y. Kohno, M. Maruyama, K. Nathan, L. Lu, Z. Yao, S.B. Goodman, Mesenchymal stem cell-macrophage crosstalk and bone healing, Biomaterials 196 (2019) 80-89.
[79] P.J. Murray, T.A. Wynn, Protective and pathogenic functions of macrophage subsets, Nat Rev Immunol 11(11) (2011) 723-37.
[80] M.K. Chang, L.J. Raggatt, K.A. Alexander, J.S. Kuliwaba, N.L. Fazzalari, K. Schroder, E.R. Maylin, V.M. Ripoll, D.A. Hume, A.R. Pettit, Osteal tissue macrophages are intercalated throughout human and mouse bone lining tissues and regulate osteoblast function in vitro and in vivo, J Immunol 181(2) (2008) 1232-44.
[81] L. Vi, G.S. Baht, H. Whetstone, A. Ng, Q. Wei, R. Poon, S. Mylvaganam, M. Grynpas, B.A. Alman, Macrophages promote osteoblastic differentiation in-vivo: implications in fracture repair and bone homeostasis, J Bone Miner Res 30(6) (2015) 1090-102.
[82] K.A. Alexander, M.K. Chang, E.R. Maylin, T. Kohler, R. Muller, A.C. Wu, N. Van Rooijen, M.J. Sweet, D.A. Hume, L.J. Raggatt, A.R. Pettit, Osteal macrophages promote in vivo intramembranous bone healing in a mouse tibial injury model, J Bone Miner Res 26(7) (2011) 1517-32.
[83] L.J. Raggatt, M.E. Wullschleger, K.A. Alexander, A.C. Wu, S.M. Millard, S. Kaur, M.L. Maugham, L.S. Gregory, R. Steck, A.R. Pettit, Fracture healing via periosteal callus formation requires macrophages for both initiation and progression of early endochondral ossification, Am J Pathol 184(12) (2014) 3192-204.
[84] A. Insua, A. Monje, H.L. Wang, R.J. Miron, Basis of bone metabolism around dental implants during osseointegration and peri-implant bone loss, J Biomed Mater Res A 105(7) (2017) 2075-2089.
[85] G.N. Thalji, S. Nares, L.F. Cooper, Early molecular assessment of osseointegration in humans, Clin Oral Implants Res 25(11) (2014) 1273-1285.
[86] T. Berglundh, I. Abrahamsson, N.P. Lang, J. Lindhe, De novo alveolar bone formation adjacent to endosseous implants, Clin Oral Implants Res 14(3) (2003) 251-62.
[87] L.J. Raggatt, N.C. Partridge, Cellular and molecular mechanisms of bone remodeling, J Biol Chem 285(33) (2010) 25103-8.
[88] A. Yamada, M. Takami, T. Kawawa, R. Yasuhara, B. Zhao, A. Mochizuki, Y. Miyamoto, T. Eto, H. Yasuda, Y. Nakamichi, N. Kim, T. Katagiri, T. Suda, R. Kamijo, Interleukin-4 inhibition of osteoclast

differentiation is stronger than that of interleukin-13 and they are equivalent for induction of osteoprotegerin production from osteoblasts, Immunology 120(4) (2007) 573-9.
[89] Y.H. Zhang, A. Heulsmann, M.M. Tondravi, A. Mukherjee, Y. Abu-Amer, Tumor necrosis factor-alpha (TNF) stimulates RANKL-induced osteoclastogenesis via coupling of TNF type 1 receptor and RANK signaling pathways, J Biol Chem 276(1) (2001) 563-8.
[90] S.R. Goldring, Bone and joint destruction in rheumatoid arthritis: what is really happening?, J Rheumatol Suppl 65 (2002) 44-8.
[91] M. Lennerås, A. Palmquist, B. Norlindh, L. Emanuelsson, P. Thomsen, O. Omar, Oxidized Titanium Implants Enhance Osseointegration via Mechanisms Involving RANK/RANKL/OPG Regulation, Clin Implant Dent Relat Res 17 Suppl 2 (2015) e486-500.
[92] D.J. Hadjidakis, Androulakis, II, Bone remodeling, Ann N Y Acad Sci 1092 (2006) 385-96.
[93] A.R. Hayman, Tartrate-resistant acid phosphatase (TRAP) and the osteoclast/immune cell dichotomy, Autoimmunity 41(3) (2008) 218-23.
[94] S.K. Lee, S.R. Goldring, J.A. Lorenzo, Expression of the calcitonin receptor in bone marrow cell cultures and in bone: a specific marker of the differentiated osteoclast that is regulated by calcitonin, Endocrinology 136(10) (1995) 4572-81.
[95] U.H. Lerner, Osteoclast formation and resorption, Matrix Biol 19(2) (2000) 107-20.
[96] G. Thalji, L.F. Cooper, Molecular assessment of osseointegration in vivo: a review of the current literature, Int J Oral Maxillofac Implants 28(6) (2013) e521-34.
[97] G. Thalji, L.F. Cooper, Molecular assessment of osseointegration in vitro: a review of current literature, Int J Oral Maxillofac Implants 29(2) (2014) e171-99.
[98] S. Shanbhag, V. Shanbhag, A. Stavropoulos, Genomic analyses of early peri-implant bone healing in humans: a systematic review, Int J Implant Dent 1(1) (2015) 5.
[99] O. Omar, F. Shah, K. Ruscsák, S. Shariel, A. Palmquist, P. Thomsen, Cellular and molecular reactions to dental implants, in: A.H.J. JA (Ed.), Dental Implants and Bone Grafts, ELSEVIER/ Woodhead Publishing2019, pp. 183-205.
[100] O. Omar, F. Suska, M. Lenneras, N. Zoric, S. Svensson, J. Hall, L. Emanuelsson, U. Nannmark, P. Thomsen, The influence of bone type on the gene expression in normal bone and at the bone-implant interface: experiments in animal model, Clin Implant Dent Relat Res 13(2) (2011) 146-56.
[101] T. Masuda, G.E. Salvi, S. Offenbacher, D.A. Felton, L.F. Cooper, Cell and matrix reactions at titanium implants in surgically prepared rat tibiae, Int J Oral Maxillofac Implants 12(4) (1997) 472-85.

[102] L. Le Guéhennec, A. Soueidan, P. Layrolle, Y. Amouriq, Surface treatments of titanium dental implants for rapid osseointegration, Dent Mater 23(7) (2007) 844-54.
[103] F. Variola, J.B. Brunski, G. Orsini, P. Tambasco de Oliveira, R. Wazen, A. Nanci, Nanoscale surface modifications of medically relevant metals: state-of-the art and perspectives, Nanoscale 3(2) (2011) 335-53.
[104] R.A. Gittens, R. Olivares-Navarrete, Z. Schwartz, B.D. Boyan, Implant osseointegration and the role of microroughness and nanostructures: lessons for spine implants, Acta Biomater 10(8) (2014) 3363-71.
[105] T. Albrektsson, A. Wennerberg, On osseointegration in relation to implant surfaces, Clin Implant Dent Relat Res 21 Suppl 1 (2019) 4-7.
[106] G. Wang, J. Li, K. Lv, W. Zhang, X. Ding, G. Yang, X. Liu, X. Jiang, Surface thermal oxidation on titanium implants to enhance osteogenic activity and in vivo osseointegration, Sci Rep 6 (2016) 31769.
[107] L. Lv, K. Li, Y. Xie, Y. Cao, X. Zheng, Enhanced osteogenic activity of anatase TiO(2) film: Surface hydroxyl groups induce conformational changes in fibronectin, Mater Sci Eng C Mater Biol Appl 78 (2017) 96-104.
[108] S.E. Wheelis, A.G. Montaño-Figueroa, M. Quevedo-Lopez, D.C. Rodrigues, Effects of titanium oxide surface properties on bone-forming and soft tissue-forming cells, Clin Implant Dent Relat Res 20(5) (2018) 838-847.
[109] N. Gui, W. Xu, D.E. Myers, R. Shukla, H.P. Tang, M. Qian, The effect of ordered and partially ordered surface topography on bone cell responses: a review, Biomater Sci 6(2) (2018) 250-264.
[110] N.P. Lang, G.E. Salvi, G. Huynh-Ba, S. Ivanovski, N. Donos, D.D. Bosshardt, Early osseointegration to hydrophilic and hydrophobic implant surfaces in humans, Clin Oral Implants Res 22(4) (2011) 349-56.
[111] A. Wennerberg, S. Galli, T. Albrektsson, Current knowledge about the hydrophilic and nanostructured SLActive surface, Clin Cosmet Investig Dent 3 (2011) 59-67.
[112] T. Albrektsson, Hydroxyapatite-coated implants: a case against their use, J Oral Maxillofac Surg 56(11) (1998) 1312-26.
[113] Y. Zeng, Y. Yang, L. Chen, D. Yin, H. Zhang, Y. Tashiro, S. Inui, T. Kusumoto, H. Nishizaki, T. Sekino, J. Okazaki, S. Komasa, Optimized Surface Characteristics and Enhanced in Vivo Osseointegration of Alkali-Treated Titanium with Nanonetwork Structures, Int J Mol Sci 20(5) (2019).
[114] W.A. Camargo, S. Takemoto, J.W. Hoekstra, S.C.G. Leeuwenburgh, J.A. Jansen, J. van den Beucken, H.S. Alghamdi, Effect of surface alkali-based treatment of titanium implants on ability to promote in vitro mineralization and in vivo bone formation, Acta Biomater 57 (2017) 511-523.
[115] K. Isoshima, T. Ueno, Y. Arai, H. Saito, P. Chen, Y. Tsutsumi, T. Hanawa, N. Wakabayashi, The change of surface charge by lithium ion coating

enhances protein adsorption on titanium, J Mech Behav Biomed Mater 100 (2019) 103393.
[116] A. Kuwabara, N. Hori, T. Sawada, N. Hoshi, A. Watazu, K. Kimoto, Enhanced biological responses of a hydroxyapatite/TiO2 hybrid structure when surface electric charge is controlled using radiofrequency sputtering, Dent Mater J 31(3) (2012) 368-76.
[117] B.R. Chrcanovic, T. Albrektsson, A. Wennerberg, Reasons for failures of oral implants, J Oral Rehabil 41(6) (2014) 443-76.
[118] M.J. Kim, C.W. Kim, Y.J. Lim, S.J. Heo, Microrough titanium surface affects biologic response in MG63 osteoblast-like cells, J Biomed Mater Res A 79(4) (2006) 1023-32.
[119] S.L. Hyzy, R. Olivares-Navarrete, D.L. Hutton, C. Tan, B.D. Boyan, Z. Schwartz, Microstructured titanium regulates interleukin production by osteoblasts, an effect modulated by exogenous BMP-2, Acta Biomater 9(3) (2013) 5821-9.
[120] Z. Schwartz, P. Raz, G. Zhao, Y. Barak, M. Tauber, H. Yao, B.D. Boyan, Effect of micrometer-scale roughness of the surface of Ti6Al4V pedicle screws in vitro and in vivo, J Bone Joint Surg Am 90(11) (2008) 2485-98.
[121] T. Albrektsson, A. Wennerberg, Oral implant surfaces: Part 1--review focusing on topographic and chemical properties of different surfaces and in vivo responses to them, Int J Prosthodont 17(5) (2004) 536-43.
[122] A. Wennerberg, T. Albrektsson, B. Chrcanovic, Long-term clinical outcome of implants with different surface modifications, Eur J Oral Implantol 11 Suppl 1 (2018) S123-s136.
[123] J.L. Ong, D.C.N. Chan, A Review of Hydroxapatite and its use as a Coating in Dental Implants, Crit Rev Biomed Eng 45(1-6) (2017) 411-451.
[124] M.J. Glimcher, The nature of the mineral component of bone and the mechanism of calcification, Instr Course Lect 36 (1987) 49-69.
[125] Z. Chen, A. Bachhuka, F. Wei, X. Wang, G. Liu, K. Vasilev, Y. Xiao, Nanotopography-based strategy for the precise manipulation of osteoimmunomodulation in bone regeneration, Nanoscale 9(46) (2017) 18129-18152.
[126] M.J. Davison, R.J. McMurray, C.A. Smith, M.J. Dalby, R.D. Meek, Nanopit-induced osteoprogenitor cell differentiation: The effect of nanopit depth, J Tissue Eng 7 (2016) 2041731416652778.
[127] M.J. Dalby, N. Gadegaard, M.O. Riehle, C.D. Wilkinson, A.S. Curtis, Investigating filopodia sensing using arrays of defined nano-pits down to 35 nm diameter in size, Int J Biochem Cell Biol 36(10) (2004) 2005-15.
[128] E. Lamers, X.F. Walboomers, M. Domanski, J. te Riet, F.C. van Delft, R. Luttge, L.A. Winnubst, H.J. Gardeniers, J.A. Jansen, The influence of nanoscale grooved substrates on osteoblast behavior and extracellular matrix deposition, Biomaterials 31(12) (2010) 3307-16.

[129] A. Klymov, L. Prodanov, E. Lamers, J.A. Jansen, X.F. Walboomers, Understanding the role of nano-topography on the surface of a bone-implant, Biomater Sci 1(2) (2013) 135-151.
[130] P.T. de Oliveira, A. Nanci, Nanotexturing of titanium-based surfaces upregulates expression of bone sialoprotein and osteopontin by cultured osteogenic cells, Biomaterials 25(3) (2004) 403-13.
[131] P.T. de Oliveira, S.F. Zalzal, M.M. Beloti, A.L. Rosa, A. Nanci, Enhancement of in vitro osteogenesis on titanium by chemically produced nanotopography, J Biomed Mater Res A 80(3) (2007) 554-64.
[132] Q.L. Ma, L. Fang, N. Jiang, L. Zhang, Y. Wang, Y.M. Zhang, L.H. Chen, Bone mesenchymal stem cell secretion of sRANKL/OPG/M-CSF in response to macrophage-mediated inflammatory response influences osteogenesis on nanostructured Ti surfaces, Biomaterials 154 (2018) 234-247.
[133] J. Wang, F. Meng, W. Song, J. Jin, Q. Ma, D. Fei, L. Fang, L. Chen, Q. Wang, Y. Zhang, Nanostructured titanium regulates osseointegration via influencing macrophage polarization in the osteogenic environment, Int J Nanomedicine 13 (2018) 4029-4043.
[134] M. Kulkarni, A. Mazare, E. Gongadze, S. Perutkova, V. Kralj-Iglic, I. Milosev, P. Schmuki, A. Iglic, M. Mozetic, Titanium nanostructures for biomedical applications, Nanotechnology 26(6) (2015) 062002.
[135] D. Karazisis, A.M. Ballo, S. Petronis, H. Agheli, L. Emanuelsson, P. Thomsen, O. Omar, The role of well-defined nanotopography of titanium implants on osseointegration: cellular and molecular events in vivo, Int J Nanomedicine 11 (2016) 1367-82.
[136] D. Karazisis, S. Petronis, H. Agheli, L. Emanuelsson, B. Norlindh, A. Johansson, L. Rasmusson, P. Thomsen, O. Omar, The influence of controlled surface nanotopography on the early biological events of osseointegration, Acta Biomater 53 (2017) 559-571.
[137] A. Ballo, H. Agheli, J. Lausmaa, P. Thomsen, S. Petronis, Nanostructured model implants for in vivo studies: influence of well-defined nanotopography on de novo bone formation on titanium implants, Int J Nanomedicine 6 (2011) 3415-28.
[138] L.M. Svanborg, M. Andersson, A. Wennerberg, Surface characterization of commercial oral implants on the nanometer level, J Biomed Mater Res B Appl Biomater 92(2) (2010) 462-9.
[139] C.A. Siedlecki, R.E. Marchant, Atomic force microscopy for characterization of the biomaterial interface, Biomaterials 19(4-5) (1998) 441-54.
[140] J. Lu, T.J. Webster, Reduced immune cell responses on nano and submicron rough titanium, Acta Biomater 16 (2015) 223-31.

[141] D. Khang, J. Lu, C. Yao, K.M. Haberstroh, T.J. Webster, The role of nanometer and sub-micron surface features on vascular and bone cell adhesion on titanium, Biomaterials 29(8) (2008) 970-83.
[142] K.C. Popat, L. Leoni, C.A. Grimes, T.A. Desai, Influence of engineered titania nanotubular surfaces on bone cells, Biomaterials 28(21) (2007) 3188-97.
[143] C. Yao, E.B. Slamovich, T.J. Webster, Enhanced osteoblast functions on anodized titanium with nanotube-like structures, J Biomed Mater Res A 85(1) (2008) 157-66.
[144] W.L. Lu, N. Wang, P. Gao, C.Y. Li, H.S. Zhao, Z.T. Zhang, Effects of anodic titanium dioxide nanotubes of different diameters on macrophage secretion and expression of cytokines and chemokines, Cell Prolif 48(1) (2015) 95-104.
[145] J. Wang, S. Qian, X. Liu, L. Xu, X. Miao, Z. Xu, L. Cao, H. Wang, X. Jiang, M2 macrophages contribute to osteogenesis and angiogenesis on nanotubular TiO2 surfaces, J Mater Chem B 5(18) (2017) 3364-3376.
[146] T. Sjöström, L.E. McNamara, R.M. Meek, M.J. Dalby, B. Su, 2D and 3D nanopatterning of titanium for enhancing osteoinduction of stem cells at implant surfaces, Adv Healthc Mater 2(9) (2013) 1285-93.
[147] T. Sjöström, L.E. McNamara, L. Yang, M.J. Dalby, B. Su, Novel anodization technique using a block copolymer template for nanopatterning of titanium implant surfaces, ACS Appl Mater Interfaces 4(11) (2012) 6354-61.
[148] R.K. Silverwood, P.G. Fairhurst, T. Sjostrom, F. Welsh, Y. Sun, G. Li, B. Yu, P.S. Young, B. Su, R.M. Meek, M.J. Dalby, P.M. Tsimbouri, Analysis of Osteoclastogenesis/Osteoblastogenesis on Nanotopographical Titania Surfaces, Adv Healthc Mater 5(8) (2016) 947-55.
[149] C. Ning, S. Wang, Y. Zhu, M. Zhong, X. Lin, Y. Zhang, G. Tan, M. Li, Z. Yin, P. Yu, X. Wang, Y. Li, T. He, W. Chen, Y. Wang, C. Mao, Ti nanorod arrays with a medium density significantly promote osteogenesis and osteointegration, Sci Rep 6 (2016) 19047.
[150] T. Sjöström, M.J. Dalby, A. Hart, R. Tare, R.O. Oreffo, B. Su, Fabrication of pillar-like titania nanostructures on titanium and their interactions with human skeletal stem cells, Acta Biomater 5(5) (2009) 1433-41.
[151] L.E. McNamara, T. Sjöström, K.E. Burgess, J.J. Kim, E. Liu, S. Gordonov, P.V. Moghe, R.M. Meek, R.O. Oreffo, B. Su, M.J. Dalby, Skeletal stem cell physiology on functionally distinct titania nanotopographies, Biomaterials 32(30) (2011) 7403-10.
[152] G.M. de Peppo, H. Agheli, C. Karlsson, K. Ekstrom, H. Brisby, M. Lenneras, S. Gustafsson, P. Sjovall, A. Johansson, E. Olsson, J. Lausmaa, P. Thomsen, S. Petronis, Osteogenic response of human mesenchymal stem cells to well-defined nanoscale topography in vitro, Int J Nanomedicine 9 (2014) 2499-515.

[153] P. Roach, D. Eglin, K. Rohde, C.C. Perry, Modern biomaterials: a review - bulk properties and implications of surface modifications, J Mater Sci Mater Med 18(7) (2007) 1263-77.
[154] M. Lord, M. Foss, F. Besenbacher, Influence of nanoscale surface topography on protein adsorption and cellular response, Nano Today 5 (2010) 66-78.
[155] C.J. Wilson, R.E. Clegg, D.I. Leavesley, M.J. Pearcy, Mediation of biomaterial-cell interactions by adsorbed proteins: a review, Tissue Eng 11(1-2) (2005) 1-18.
[156] T.J. Webster, C. Ergun, R.H. Doremus, R.W. Siegel, R. Bizios, Specific proteins mediate enhanced osteoblast adhesion on nanophase ceramics, J Biomed Mater Res 51(3) (2000) 475-83.
[157] S. Di Cio, J.E. Gautrot, Cell sensing of physical properties at the nanoscale: Mechanisms and control of cell adhesion and phenotype, Acta Biomater 30 (2016) 26-48.
[158] L.M. Bjursten, L. Rasmusson, S. Oh, G.C. Smith, K.S. Brammer, S. Jin, Titanium dioxide nanotubes enhance bone bonding in vivo, J Biomed Mater Res A 92(3) (2010) 1218-24.
[159] G. Giavaresi, M. Tschon, J.H. Daly, J.J. Liggat, D.S. Sutherland, H. Agheli, M. Fini, P. Torricelli, R. Giardino, In vitro and in vivo response to nanotopographically-modified surfaces of poly(3-hydroxybutyrate-co-3-hydroxyvalerate) and polycaprolactone, J Biomater Sci Polym Ed 17(12) (2006) 1405-23.
[160] X. Wu, X. Liu, J. Wei, J. Ma, F. Deng, S. Wei, Nano-TiO2/PEEK bioactive composite as a bone substitute material: in vitro and in vivo studies, Int J Nanomedicine 7 (2012) 1215-25.
[161] L. Meirelles, L. Melin, T. Peltola, P. Kjellin, I. Kangasniemi, F. Currie, M. Andersson, T. Albrektsson, A. Wennerberg, Effect of hydroxyapatite and titania nanostructures on early in vivo bone response, Clin Implant Dent Relat Res 10(4) (2008) 245-54.
[162] V.C. Mendes, R. Moineddin, J.E. Davies, Discrete calcium phosphate nanocrystalline deposition enhances osteoconduction on titanium-based implant surfaces, J Biomed Mater Res A 90(2) (2009) 577-85.
[163] Q.L. Ma, L.Z. Zhao, R.R. Liu, B.Q. Jin, W. Song, Y. Wang, Y.S. Zhang, L.H. Chen, Y.M. Zhang, Improved implant osseointegration of a nanostructured titanium surface via mediation of macrophage polarization, Biomaterials 35(37) (2014) 9853-9867.
[164] Y. Dang, L. Zhang, W. Song, B. Chang, T. Han, Y. Zhang, L. Zhao, In vivo osseointegration of Ti implants with a strontium-containing nanotubular coating, Int J Nanomedicine 11 (2016) 1003-11.

[165] A. Bandyopadhyay, A. Shivaram, I. Mitra, S. Bose, Electrically polarized TiO2 nanotubes on Ti implants to enhance early-stage osseointegration, Acta Biomater 96 (2019) 686-693.
[166] A. Palmquist, F. Lindberg, L. Emanuelsson, R. Branemark, H. Engqvist, P. Thomsen, Biomechanical, histological, and ultrastructural analyses of laser micro- and nano-structured titanium alloy implants: a study in rabbit, J Biomed Mater Res A 92(4) (2010) 1476-86.
[167] A. Palmquist, L. Emanuelsson, R. Branemark, P. Thomsen, Biomechanical, histological and ultrastructural analyses of laser micro- and nano-structured titanium implant after 6 months in rabbit, J Biomed Mater Res B Appl Biomater 97(2) (2011) 289-98.
[168] N. Wang, H. Li, W. Lu, J. Li, J. Wang, Z. Zhang, Y. Liu, Effects of TiO2 nanotubes with different diameters on gene expression and osseointegration of implants in minipigs, Biomaterials 32(29) (2011) 6900-11.
[169] A.S.H. Buddy D. Ratner, Frederic J. Schoen, Jack E. Lemons, Biomaterials Science, Academic Press.2004.
[170] G. Adams, A beginner's guide to RT-PCR, qPCR and RT-qPCR, The Biochemist 42 (2020).
[171] T. Nolan, R.E. Hands, S.A. Bustin, Quantification of mRNA using real-time RT-PCR, Nat Protoc 1(3) (2006) 1559-82.
[172] J. Vandesompele, K. De Preter, F. Pattyn, B. Poppe, N. Van Roy, A. De Paepe, F. Speleman, Accurate normalization of real-time quantitative RT-PCR data by geometric averaging of multiple internal control genes, Genome biology 3(7) (2002) RESEARCH0034.
[173] C.L. Andersen, J.L. Jensen, T.F. Orntoft, Normalization of real-time quantitative reverse transcription-PCR data: a model-based variance estimation approach to identify genes suited for normalization, applied to bladder and colon cancer data sets, Cancer research 64(15) (2004) 5245-50.
[174] M.W. Pfaffl, A new mathematical model for relative quantification in real-time RT-PCR, Nucleic Acids Res 29(9) (2001) e45.
[175] K. Donath, G. Breuner, A method for the study of undecalcified bones and teeth with attached soft tissues. The Sage-Schliff (sawing and grinding) technique, J Oral Pathol 11(4) (1982) 318-26.
[176] R. Branemark, L.O. Ohrnell, P. Nilsson, P. Thomsen, Biomechanical characterization of osseointegration during healing: an experimental in vivo study in the rat, Biomaterials 18(14) (1997) 969-78.
[177] R. Branemark, R. Skalak, An in-vivo method for biomechanical characterization of bone-anchored implants, Med Eng Phys 20(3) (1998) 216-9.
[178] F. Faul, E. Erdfelder, A.G. Lang, A. Buchner, G*Power 3: a flexible statistical power analysis program for the social, behavioral, and biomedical sciences, Behav Res Methods 39(2) (2007) 175-91.

[179] M. Bryington, G. Mendonca, S. Nares, L.F. Cooper, Osteoblastic and cytokine gene expression of implant-adherent cells in humans, Clin Oral Implants Res 25(1) (2014) 52-8.
[180] K.M. Ainslie, S.L. Tao, K.C. Popat, H. Daniels, V. Hardev, C.A. Grimes, T.A. Desai, In vitro inflammatory response of nanostructured titania, silicon oxide, and polycaprolactone, J Biomed Mater Res A 91(3) (2009) 647-55.
[181] T. Schmitz, M. Jannasch, T. Weigel, C. Moseke, U. Gbureck, J. Groll, H. Walles, J. Hansmann, Nanotopographical Coatings Induce an Early Phenotype-Specific Response of Primary Material-Resident M1 and M2 Macrophages, Materials (Basel) 13(5) (2020).
[182] R. Sridharan, A.R. Cameron, D.J. Kelly, C.J. Kearney, F.J. O'Brien, Biomaterial based modulation of macrophage polarization: a review and suggested design principles, Materials Today 18(6) (2015) 313-325.
[183] J.K. Chan, G.E. Glass, A. Ersek, A. Freidin, G.A. Williams, K. Gowers, A.I. Espirito Santo, R. Jeffery, W.R. Otto, R. Poulsom, M. Feldmann, S.M. Rankin, N.J. Horwood, J. Nanchahal, Low-dose TNF augments fracture healing in normal and osteoporotic bone by up-regulating the innate immune response, EMBO Mol Med 7(5) (2015) 547-61.
[184] J. Hashimoto, H. Yoshikawa, K. Takaoka, N. Shimizu, K. Masuhara, T. Tsuda, S. Miyamoto, K. Ono, Inhibitory effects of tumor necrosis factor alpha on fracture healing in rats, Bone 10(6) (1989) 453-7.
[185] A.L. Ponte, E. Marais, N. Gallay, A. Langonné, B. Delorme, O. Hérault, P. Charbord, J. Domenech, The in vitro migration capacity of human bone marrow mesenchymal stem cells: comparison of chemokine and growth factor chemotactic activities, Stem Cells 25(7) (2007) 1737-45.
[186] A. D'Andrea, X. Ma, M. Aste-Amezaga, C. Paganin, G. Trinchieri, Stimulatory and inhibitory effects of interleukin (IL)-4 and IL-13 on the production of cytokines by human peripheral blood mononuclear cells: priming for IL-12 and tumor necrosis factor alpha production, J Exp Med 181(2) (1995) 537-46.
[187] I.M. Rea, D.S. Gibson, V. McGilligan, S.E. McNerlan, H.D. Alexander, O.A. Ross, Age and Age-Related Diseases: Role of Inflammation Triggers and Cytokines, Front Immunol 9 (2018) 586.
[188] J. Liang, S. Xu, M. Shen, B. Cheng, Y. Li, X. Liu, D. Qin, A. Bellare, L. Kong, Osteogenic activity of titanium surfaces with hierarchical micro-/nano-structures obtained by hydrofluoric acid treatment, Int J Nanomedicine 12 (2017) 1317-1328.
[189] R.A. Gittens, R. Olivares-Navarrete, S.L. Hyzy, K.H. Sandhage, Z. Schwartz, B.D. Boyan, Superposition of nanostructures on microrough titanium-aluminum-vanadium alloy surfaces results in an altered integrin expression profile in osteoblasts, Connect Tissue Res 55 Suppl 1 (2014) 164-8.

[190] R.A. Gittens, R. Olivares-Navarrete, T. McLachlan, Y. Cai, S.L. Hyzy, J.M. Schneider, Z. Schwartz, K.H. Sandhage, B.D. Boyan, Differential responses of osteoblast lineage cells to nanotopographically-modified, microroughened titanium-aluminum-vanadium alloy surfaces, Biomaterials 33(35) (2012) 8986-94.
[191] P. Zhou, F. Mao, F. He, Y. Han, H. Li, J. Chen, S. Wei, Screening the optimal hierarchical micro/nano pattern design for the neck and body surface of titanium implants, Colloids Surf B Biointerfaces 178 (2019) 515-524.
[192] K. Gulati, H.J. Moon, T. Li, P.T. Sudheesh Kumar, S. Ivanovski, Titania nanopores with dual micro-/nano-topography for selective cellular bioactivity, Mater Sci Eng C Mater Biol Appl 91 (2018) 624-630.
[193] X. Ding, L. Zhou, J. Wang, Q. Zhao, X. Lin, Y. Gao, S. Li, J. Wu, M. Rong, Z. Guo, C. Lai, H. Lu, F. Jia, The effects of hierarchical micro/nanosurfaces decorated with TiO2 nanotubes on the bioactivity of titanium implants in vitro and in vivo, Int J Nanomedicine 10 (2015) 6955-73.
[194] S. Nesbitt, A. Nesbit, M. Helfrich, M. Horton, Biochemical characterization of human osteoclast integrins. Osteoclasts express alpha v beta 3, alpha 2 beta 1, and alpha v beta 1 integrins, J Biol Chem 268(22) (1993) 16737-45.
[195] A.M. Moursi, R.K. Globus, C.H. Damsky, Interactions between integrin receptors and fibronectin are required for calvarial osteoblast differentiation in vitro, J Cell Sci 110 (Pt 18) (1997) 2187-96.
[196] M. Mizuno, R. Fujisawa, Y. Kuboki, Type I collagen-induced osteoblastic differentiation of bone-marrow cells mediated by collagen-alpha2beta1 integrin interaction, J Cell Physiol 184(2) (2000) 207-13.
[197] D.E. Hughes, D.M. Salter, S. Dedhar, R. Simpson, Integrin expression in human bone, J Bone Miner Res 8(5) (1993) 527-33.
[198] D. Khang, J. Choi, Y.M. Im, Y.J. Kim, J.H. Jang, S.S. Kang, T.H. Nam, J. Song, J.W. Park, Role of subnano-, nano- and submicron-surface features on osteoblast differentiation of bone marrow mesenchymal stem cells, Biomaterials 33(26) (2012) 5997-6007.
[199] T.G. Kashima, T. Nishiyama, K. Shimazu, M. Shimazaki, I. Kii, A.E. Grigoriadis, M. Fukayama, A. Kudo, Periostin, a novel marker of intramembranous ossification, is expressed in fibrous dysplasia and in c-Fos-overexpressing bone lesions, Hum Pathol 40(2) (2009) 226-37.
[200] S. Wei, H. Kitaura, P. Zhou, F.P. Ross, S.L. Teitelbaum, IL-1 mediates TNF-induced osteoclastogenesis, J Clin Invest 115(2) (2005) 282-90.
[201] F.A. Shah, M.L. Johansson, O. Omar, H. Simonsson, A. Palmquist, P. Thomsen, Laser-Modified Surface Enhances Osseointegration and Biomechanical Anchorage of Commercially Pure Titanium Implants for Bone-Anchored Hearing Systems, PLoS One 11(6) (2016) e0157504.
[202] A. Azeem, A. English, P. Kumar, A. Satyam, M. Biggs, E. Jones, B. Tripathi, N. Basu, J. Henkel, C. Vaquette, N. Rooney, G. Riley, A. O'Riordan,

G. Cross, S. Ivanovski, D. Hutmacher, A. Pandit, D. Zeugolis, The influence of anisotropic nano- to micro-topography on in vitro and in vivo osteogenesis, Nanomedicine (Lond) 10(5) (2015) 693-711.
[203] E. Lamers, X.F. Walboomers, M. Domanski, L. Prodanov, J. Melis, R. Luttge, L. Winnubst, J.M. Anderson, H.J. Gardeniers, J.A. Jansen, In vitro and in vivo evaluation of the inflammatory response to nanoscale grooved substrates, Nanomedicine 8(3) (2012) 308-17.
[204] A. Wilkinson, R.N. Hewitt, L.E. McNamara, D. McCloy, R.M. Dominic Meek, M.J. Dalby, Biomimetic microtopography to enhance osteogenesis in vitro, Acta Biomater 7(7) (2011) 2919-25.
[205] M.J. Biggs, R.G. Richards, N. Gadegaard, C.D. Wilkinson, M.J. Dalby, The effects of nanoscale pits on primary human osteoblast adhesion formation and cellular spreading, J Mater Sci Mater Med 18(2) (2007) 399-404.
[206] M.J. Dalby, N. Gadegaard, R. Tare, A. Andar, M.O. Riehle, P. Herzyk, C.D. Wilkinson, R.O. Oreffo, The control of human mesenchymal cell differentiation using nanoscale symmetry and disorder, Nat Mater 6(12) (2007) 997-1003.
[207] J. Fiedler, B. Ozdemir, J. Bartholomä, A. Plettl, R.E. Brenner, P. Ziemann, The effect of substrate surface nanotopography on the behavior of multipotnent mesenchymal stromal cells and osteoblasts, Biomaterials 34(35) (2013) 8851-9.
[208] M. Mohiuddin, H.A. Pan, Y.C. Hung, G.S. Huang, Control of growth and inflammatory response of macrophages and foam cells with nanotopography, Nanoscale Res Lett 7(1) (2012) 394.
[209] J. Park, S. Bauer, K.A. Schlegel, F.W. Neukam, K. von der Mark, P. Schmuki, TiO2 nanotube surfaces: 15 nm--an optimal length scale of surface topography for cell adhesion and differentiation, Small 5(6) (2009) 666-71.
[210] J. Park, S. Bauer, K. von der Mark, P. Schmuki, Nanosize and vitality: TiO2 nanotube diameter directs cell fate, Nano Lett 7(6) (2007) 1686-91.
[211] K.S. Brammer, S. Oh, C.J. Cobb, L.M. Bjursten, H. van der Heyde, S. Jin, Improved bone-forming functionality on diameter-controlled TiO(2) nanotube surface, Acta Biomater 5(8) (2009) 3215-23.
[212] C. von Wilmowsky, S. Bauer, S. Roedl, F.W. Neukam, P. Schmuki, K.A. Schlegel, The diameter of anodic TiO2 nanotubes affects bone formation and correlates with the bone morphogenetic protein-2 expression in vivo, Clin Oral Implants Res 23(3) (2012) 359-66.
[213] J.C.M. Souza, M.B. Sordi, M. Kanazawa, S. Ravindran, B. Henriques, F.S. Silva, C. Aparicio, L.F. Cooper, Nano-scale modification of titanium implant surfaces to enhance osseointegration, Acta Biomater 94 (2019) 112-131.